Title	がん光温熱治療のための多機能ソフトナノ材料の開発
Author(s)	戚, 耘
Citation	
Issue Date	2025-03
Type	Thesis or Dissertation
Text version	ETD
URL	http://hdl.handle.net/10119/19935
Rights	
Description	Supervisor: 都 英次郎, 先端科学技術研究科, 博士

Doctoral Dissertation

Development of Multifunctional Soft Nanomaterials for Photothermal Cancer Therapy

Yun QI

Supervisor: Eijiro MIYAKO

Graduate School of Advanced Science and Technology
Japan Advanced Institute of Science and Technology
(Materials Science)
March　2025

Abstract

Cancer is one of the leading causes of death worldwide. According to the World Health Organization (WHO), approximately 10 million deaths were attributed to cancer in 2020. With an aging population and lifestyle factors, the number of cases is expected to continue rising. Despite significant advancements in science, technology, and societal development, cancer remains a significant global health challenge due to the limitations of conventional therapies, such as poor specificity, severe side effects, and limited efficacy against metastatic disease.

This study focuses on developing novel multifunctional nanoconjugates using liquid metal (LM) and ionic liquid (IL) as soft materials for advanced cancer theranostics. The research emphasizes photothermal therapy (PTT), immunotherapy, and bioimaging, by using the impressive photothermal conversion of LM- and carbon nanohorns (CNHs)-based nanoconjugates. The nanoparticles were chemically functionalized with biomolecules and fluorescent dyes to improve stability, dispersibility, and biocompatibility. These nanoparticles exhibited exceptional photothermal conversion efficiency and selective tumor ablation under near-infrared (NIR) laser irradiation, with less side effects. Additionally, surface modification with immunostimulants enabled synergistic integration of PTT and immunotherapy, enhancing therapeutic efficacy. Building on this, we also introduced smart magnetically driven nanoconjugates by loading magnetic IL. These nanoconjugates demonstrated precise magnetic responsiveness, providing a solution to the low targeting of the enhanced permeability and retention (EPR) effect and enabling controlled drug delivery and localized photothermal effects. This innovative approach expanded the versatility of soft materials in cancer treatment. *In vivo* mice tumor model confirmed the therapeutic potential of LM and CNHs-based nanoconjugates, achieving significant tumor regression, enhanced bioimaging, and excellent biological safety. This work advances the field of cancer nanomedicine, providing a multifunctional platform for nanotheranostics and targeted therapies.

Keywords: cancer, nanoparticles, soft material, near infrared laser, photothermal therapy, immunotherapy, chemical functionalization

Referee-in-chief:

Prof. Dr. Eijiro MIYAKO

Japan Advanced Institute of Science and Technology (JAIST)

Referees:

Prof. Dr. Kazuaki MATSUMURA

Japan Advanced Institute of Science and Technology (JAIST)

Prof. Dr. Motoichi KURISAWA

Japan Advanced Institute of Science and Technology (JAIST)

Prof. Dr. Shun NISHIMURA

Japan Advanced Institute of Science and Technology (JAIST)

Dr. Mitsumasa TAGUCHI

National Institutes for Quantum Science and Technology (QST)

Contents

List of Tables and Figures

biologically independent tests), ***, $p < 0.001$ vs control w/o nanoparticles (Student's *t-test*).

Figure 2.13 Cell viability after the treatment of 5 min NIR laser irradiation of laser-induced gelatin-LM nanoparticles at various concentrations. Data presented as means ± SEM ($n = 4$;biologically independent tests), **, $p < 0.01$.

Figure 2.14 Optical micrographs of Colon26 cells after 6 h incubation with and without 0.1 mg ml^{-1} gelatin-LM at 37 °C in 5% CO_2.

Figure 2.15 Optical micrographs of Colon26 cells after 6 h incubation with and without 0.1 mg ml^{-1} gelatin-LM at 4 °C in 5% CO_2. Black arrows show gelatin-LMs.

Figure 2.16 Cancer cell destruction by laser-induced gelatin-LM before and after laser irradiation. The red circle shows laser irradiation position and area.

Figure 2.17 Direct observation of laser-induced cancer cell behavior without gelatin-LM before and after laser irradiation. The red circle shows laser irradiation position and area.

Figure 2.18 Schematic illustration of DyLight800-gelatin-LM.

Figure 2.19 UV−Vis−NIR optical absorption spectrum of gelatin-LM, DyLight800, and DyLight800-gelatin-LM

Figure 2.20 A) The fluorescence spectrum of DyLight800-gelatin-LM at various excitation wavelengths. **B)** Two-vial images represent DyLight800-gelatin-LM (left) and gelatin-LM (right) FL properties under NIR-exposed bioimaging.

Figure 2.21 The fluorescence spectrums of gelatin-LM, DyLight800, and DyLight800-gelatin-LM at various excitation wavelengths.

Figure 2.22 A) FL imaging of Colon26 tumor-bearing mice after an intravenous injection of DyLight800-gelatin-LM. Blue dashed circle denotes solid tumor location. **B)** FL imaging of tumor and major organs after 24 h injection.

Figure 2.23 Experimental design of photothermal therapy using gelatin-LM in syngeneic tumor models.

Figure 2.24 A) Infrared thermal images of whole-mouse bodies with and without laser irradiation. **B)** Solid tumor surface temperature of Colon26-bearing mice under 808 nm laser irradiation. Data represented as means ± SEM; $n = 5$ independent experiments. ns, not significant; **, $p < 0.01$, and ***, $p < 0.001$.

Figure 2.25 Mouse images after 0 and 10 d intravenous PBS injection and gelatin-LM with and without tumor laser irradiation.

Figure 2.26 Gelatin-LM injected mouse image at d-26.

Figure 2.27 A) Average solid tumor size changes under the *in vivo* anticancer effect of NIR laser-induced LM nanoparticles. **B)** Average body weight of mice after treatment. Data presented as means ± SEM ($n = 5$ biologically independent tests). ns, not significant; **, $p < 0.01$.

Figure 2.28 Mouse treatment-group hematoxylin and eosin- and TUNEL-stained tumor tissue on d-2.

Figure 3.1 Synthesis scheme of the preparation of PEG–IMIQ–LM nanoconjugates.

Figure 3.2 Image of the prepared PEG–IMIQ–LM and IMIQ–LM aqueous suspension.

Figure 3.3 The DLS result of PEG–IMIQ–LM in 1, 3, and 10 days.

calculated in comparison with the NS group. **, $p < 0.01$, and ***, $p < 0.001$, by Student's *t-test*.

Figure 3 24 *In vivo* anticancer effect of various samples with and without laser irradiation. Irradiation time = 5 min every day (total six times irradiation). Data are expressed as means ± standard error of the mean (SEM) (n = 5 biologically independent tests). *, $p < 0.05$, and ***, $p < 0.001$, by Student's *t-test*. The black arrows display the time point of sample administration.

Figure 3.25 Images of mice after each treatment.

Figure 3.26 Kaplan–Meier survival curves of Colon26-tumor-bearing mice (n = 5 biologically independent mice) after tumor implantation for 30 days. Statistical significance was calculated in comparison with the NS group. ***, $p < 0.001$ by Log-rank (Mantel–Cox) test.

Figure 3.27 Average mouse body weight after treatments during the treatment period. The black arrow displays the time point of the sample administration.

Figure 3.28 Mechanism of tumor suppression by laser-driven Anti-PD-L1–PEG–IMIQ–LM. **A)** H&E, TUNEL, and IHC stained tumor tissues collected from different groups of mice at day 1 after their respective treatments. **B)** Statistical analyses of IHC and TUNEL-positive stained tumor tissues in Figure 3.28A. Data are represented as mean ± standard error of the mean (SEM); n = 10 independent areas (region of interest) in each tumor tissue collected from the groups of mice on day 1 after treatments. Statistical significance was calculated in comparison with the NS group. *, $p < 0.05$, **, $p < 0.01$, and ***, $p < 0.001$ by Student's *t-test*.

Figure 3.29 **A)**TNF-α and IL-6-stained tumor tissues were collected from different groups of mice on day 1 after the respective treatments. **B)** Statistical analyses of TNF-α and IL-6-positive stained tumor tissues in Figure 3.29A. Data are represented as mean ± standard error of the mean (SEM); n = 10 independent areas (region of interest) in each tumor tissue collected from the groups of mice on day 1 after treatments. Statistical significance was calculated in comparison with the NS group. ***, $p < 0.001$ by Student's *t-test*.

Figure 3.30 Flow cytometry analyses of expression of CD3, CD8a, CD11b, and CD80 in spleens after i.v. injection of each sample for 3 h. **A)** Representative gating strategy for flow cytometry experiments assessing T cell (CD3 and CD8a) and DC (CD11b and CD80) populations after treatment with Anti-PD-L1–PEG–IMIQ–LM. The lymphocytes or the population of monocytes and granulocytes was gated by SSC-H vs. FSC-H, and then plotted in a new graph to calculate the percentages of the CD3, CD8a, CD11b, and CD80 positive cells in the selected total cells. Dead cells were excluded by selecting all live cells from the plots with PI staining. **B)** Statistical analyses of immunological biomarkers relevant to T cell and DC activations. Data are represented as mean ± SEM; n = 3 independent spleen tissues. Statistical significance was calculated in comparison with the NS group.*, $p < 0.05$, **, $p < 0.01$, and ***, $p < 0.001$, by one-side Student's *t-test*.

Figure 3.31 The scheme of the proposed mechanism.

Figure 4.1 Synthesis scheme of the preparation of $[Bmim][FeCl_4]$–PEG–CNH

significance was calculated in comparison with the NS group. ***, $p < 0.001$ by Log-rank (Mantel–Cox) test.

Figure 4.30 A) H&E, TUNEL, and Cleaved Caspase3 stained tumor tissues collected from different groups of mice at day 1 after their respective treatments. **B)** Statistical analyses of IHC and TUNEL-positive stained tumor tissues in Figure 4.26A. Data are represented as mean ± standard error of the mean (SEM); $n = 7$ independent areas (region of interest) in each tumor tissue collected from the groups of mice on day 1 after treatments. Statistical significance was calculated in comparison with the PBS group. *, $p < 0.05$, and ***, $p < 0.001$ by Student's *t-test*.

Chapter 1

General Introduction

1.1 Research background

Cancer is a highly invasive and metastatic disease caused by uncontrolled abnormal cell growth. It is one of the leading causes of death worldwide. According to the World Health Organization (WHO), approximately 10 million deaths were attributed to cancer in 2020. The most common types globally are breast, lung, colorectal, prostate, and stomach cancers. With an aging population and lifestyle factors, the number of cases is expected to continue rising. Despite significant advancements in science, technology, and societal development, cancer remains one of the most serious threats to human life.[1] The primary treatment modalities for cancer include surgery, radiotherapy, and chemotherapy. The choice of treatment depends on the location, malignancy, and progression of the tumor as well as the patient's physical condition. Unfortunately, these conventional treatments are gradually losing their luster as they face numerous drawbacks that hinder their widespread use. In theory, cancer can be cured if the tumor cells are completely removed surgically. But it is not always that simple, since some tumors grow fast and have no obvious boundaries with the surrounding normal tissues, a certain range of normal tissues around it must be removed during the surgery. In addition, for radiotherapy, and chemotherapy, because of its lack of specificity, it may harm healthy tissues as a side effect, causing more pain to patients.[2, 3] Meanwhile, whether surgery, radiotherapy, or chemotherapy, is extremely burdensome to the body, and after malignant metastasis occurs, it is difficult to completely cure it no matter which method is used. Therefore, cancer treatment is still a great challenge facing mankind. In the recent years, photothermal therapy (PTT) has been shown to have tremendous potential in treating cancer due to its unique benefits of high specificity and minimal invasiveness.[4] In PTT, a photosensitizer is excited by light of a specific wavelength, usually near-infrared (NIR). This activation places the sensitizer in an excited state, which then releases energy (heat), thereby leading to thermal ablation of cancer cells. In contrast to traditional treatments, PTT provides distinct benefits such as lower toxicity, enhanced specificity, and reduced invasiveness.[5, 6] These attributes position PTT as a highly effective alternative for cancer treatment.

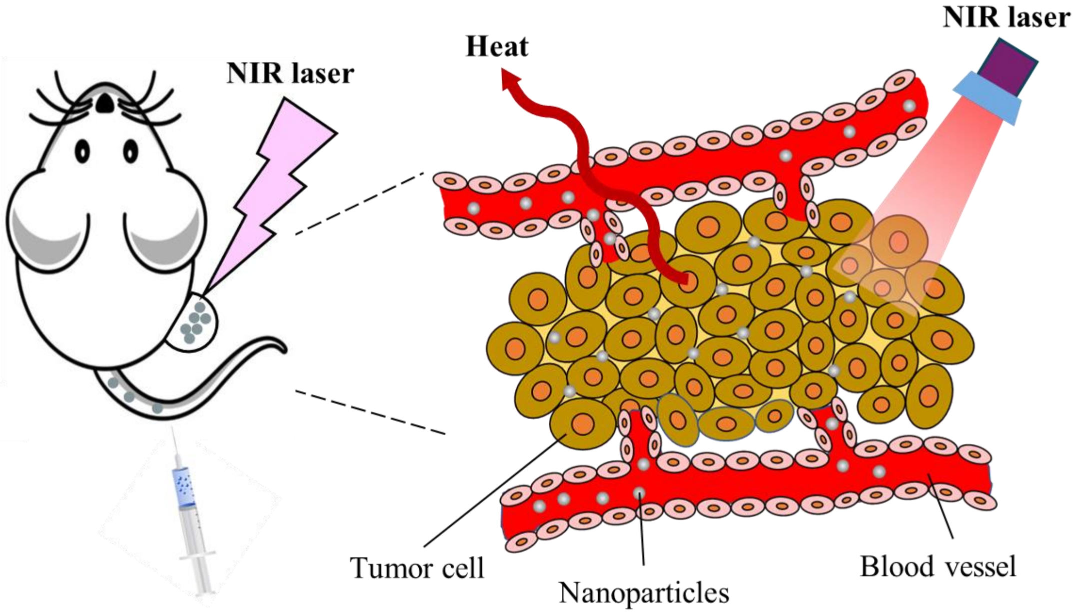

Figure 1.1 Schematic illustration of nanoparticles-based tumor specific photothermal therapy.

Many types of nanoparticles have been investigated as photosensitizers for PTT

(**Figure 1.1**). This is because particles within a certain size range (usually 20-300 nm) have an enhanced permeability and retention effect (EPR effect).[7, 8] Due to the EPR effect, the concentration of nanoparticles in tumor tissue is significantly higher than in other parts of the body, and can accumulate for a longer time. In previous studies, several materials, such as gold, gallium, copper, semiconducting polymers, and carbon, exhibit strong photothermal conversion capabilities in the NIR region, making them suitable photosensitizers for use in PTT to effectively eliminate tumors.[9-13] However, efficiently delivering nanoparticles in substantial quantities to tumors presents a significant challenge. This is because almost all nanoparticles do not have high dispersibility and stability in aqueous solutions, resulting in the inability of the photosensitizer to reach tumor tissue through blood vessels. The surface modification design of nanoparticles is crucial to improve the original properties and physical and chemical multifunctionality.

1.2 Objective of this study

The primary objective of this study is to develop novel multifunctional soft materials for photothermal cancer therapy that can effectively elicit tumor regression while minimizing or eliminating any undesirable side effects. This study presents the development of a series of functional nanoconjugates as photosensitizers for cancer photothermal therapy. These nanoconjugates are based on the utilization of soft materials such as liquid metal (LM) and ionic liquid (IL). This research incorporates three distinct formulations, each corresponding to a unique type of photothermal nanoconjugates. We used different formulations, from simply using biomolecules to improve the dispersibility and stability of nanoparticles, to linking antibodies on the surface of nanoparticles and encapsulating anticancer drugs inside to improve targeting and immune synergy, and finally developed a smart light-, and magnetic field-controllable nanoconjugates that is providing a solution to the low targeting of the EPR effect as a highly efficient photosensitizer for photothermal therapy. All these nanoconjugates in this study can be synthesized simply and efficiently, can maintain high dispersibility and stability for a long time, and can be used for intravenous injection. In addition, they have shown exciting results in further *in vitro* and *in vivo* studies in mice. Therefore, we firmly believe that these nanoconjugates have great potential as effective tools for cancer treatment and provide new solutions.

1.3 Outline of this dissertation

In **Chapter 1**, the general introduction of this dissertation summarizes the background of cancer photothermal therapy and the objective of this study.

In **Chapter 2**, a novel functional liquid metal nanoconjugate was synthesized as an innovative photosensitizer for cancer photothermal therapy. Using a biocompatible gallium-indium eutectic alloy (EGaIn) as the core and various biomolecules as the shell, these nanoconjugates achieved photothermal elimination of tumor tissues under NIR laser irradiation.

In **Chapter 3**, an innovative light-activated immunostimulant based on EGaIn nanoparticles was investigated. It can be used for targeted therapy and diagnosis via intravenous injection. By surface modification of nanoparticles with antibodies and loading of anticancer drugs, it aims to achieve effective synergistic treatment of multiple pathways.

In **Chapter 4**, a novel magnetically driven functional nanoconjugate based on IL and carbon nanohorns (CNHs) is proposed. We conjugate IL with CNHs as a potential optically and magnetically responsive drug delivery system. It is expected to provide a solution to the low targeting of the EPR effect, achieve more precise photothermal therapy.

In **Chapter 5**, the general conclusion of this dissertation, the overall finding of this study was presented, and the future prospects of this study were discussed.

1.4 Reference

1. Ali, I.; Hozaifa, M.; Ali, S.; Malik, A.; Locatelli, M., Advances in ionic liquids as future anti-cancer drugs. *Journal of Molecular Liquids* **2023,** *388.*
2. Mohan, G.; T P, A. H.; A J, J.; K M, S. D.; Narayanasamy, A.; Vellingiri, B., Recent advances in radiotherapy and its associated side effects in cancer—a review. *The Journal of Basic and Applied Zoology* **2019,** *80* (1).
3. Oun, R.; Moussa, Y. E.; Wheate, N. J., The side effects of platinum-based chemotherapy drugs: a review for chemists. *Dalton Trans* **2018,** *47* (19), 6645-6653.
4. Zou, L.; Wang, H.; He, B.; Zeng, L.; Tan, T.; Cao, H.; He, X.; Zhang, Z.; Guo, S.; Li, Y., Current Approaches of Photothermal Therapy in Treating Cancer Metastasis with Nanotherapeutics. *Theranostics* **2016,** *6* (6), 762-72.
5. Shanmugam, V.; Selvakumar, S.; Yeh, C.-S., Near-infrared light-responsive nanomaterials in cancer therapeutics. *Chemical Society Reviews* **2014,** *43* (17), 6254-6287.
6. Ma, Y.; Liang, X.; Tong, S.; Bao, G.; Ren, Q.; Dai, Z., Gold Nanoshell Nanomicelles for Potential Magnetic Resonance Imaging, Light‐Triggered Drug Release, and Photothermal Therapy. *Advanced Functional Materials* **2012,** *23* (7), 815-822.
7. Maeda, H.; Wu, J.; Sawa, T.; Matsumura, Y.; Hori, K., Tumor vascular permeability and the EPR effect in macromolecular therapeutics: a review. *Journal of Controlled Release* **2000,** *65* (1), 271-284.
8. Matsumura, Y.; Maeda, H. J. C. r., A new concept for macromolecular therapeutics in cancer chemotherapy: mechanism of tumoritropic accumulation of proteins and the antitumor agent smancs. **1986,** *46* (12_Part_1), 6387-6392.
9. Ajima, K.; Yudasaka, M.; Murakami, T.; Maigné, A.; Shiba, K.; Iijima, S. J. M. p., Carbon nanohorns as anticancer drug carriers. **2005,** *2* (6), 475-480.
10. Alkilany, A. M.; Thompson, L. B.; Boulos, S. P.; Sisco, P. N.; Murphy, C. J., Gold nanorods: Their potential for photothermal therapeutics and drug delivery, tempered by the complexity of their biological interactions. *Advanced Drug Delivery Reviews* **2012,** *64* (2), 190-199.
11. Hessel, C. M.; Pattani, V. P.; Rasch, M.; Panthani, M. G.; Koo, B.; Tunnell, J. W.; Korgel, B. A., Copper selenide nanocrystals for photothermal therapy. *Nano Lett* **2011,** *11* (6), 2560-6.
12. Li, J.; Pu, K., Semiconducting Polymer Nanomaterials as Near-Infrared Photoactivatable Protherapeutics for Cancer. *Acc Chem Res* **2020,** *53* (4), 752-762.
13. Qi, Y.; Miyahara, M.; Iwata, S.; Miyako, E., Light‐Activatable Liquid Metal Immunostimulants for Cancer Nanotheranostics. *Advanced Functional Materials* **2023,** *34* (31).

Chapter 2

Functional biomolecule-liquid metal nanoconjugates for cancer optotheranostics

2.1 Inrtoduction

2.1.1 Introduction of liquid metals

Room temperature liquid metals (LMs) represent a class of emerging multifunctional materials with attractive novel properties, such as high conductivity and favorable flexibility, those can be applied in various fields.[1, 2] Mercury is a kind of well-known liquid metal for us. Unfortunately, toxicity is the biggest disadvantage of mercury so that it is the major impediment to widespread its application. Gallium-based liquid metals (LM), particularly eutectic gallium-indium (EGaIn) and gallium-indiumtin (Galinstan), have shown broad development prospects in a variety of applications, ranging from composites and stretchable electronics to drug delivery systems, due to their low toxicity, fluidity, thermal and electrical conductivity, and optical properties.[3, 4] The research on the applications of liquid metal in the recent years are more and more worthy of attention.[5]

LM is particularly active in healthcare equipment and pharmaceuticals in biomedical applications, and they provide significant contributions to the overall biotechnology area.[6-8] Recently, many studies have reported the latest developments in the design and application of therapeutics based on LM, like drug delivery[9, 10], photothermal therapy[11, 12], magnetocaloric therapy[13] and so on. Although application of LM has obtained evident results and successes thus far, numerous problems in producing functional nanoscale LM dispersions remain to be solved. For their usage in actual medical applications, quality control of LM nanoparticle shape, size, and state of aggregation is critical.

2.1.2 Modification of liquid metal nanoparticles

Surface modification of LM nanoparticles can significantly improve their original physical and chemical properties.[5, 14] Although, many research groups have worked to improve the synthesis and chemical functionalization of LM by using a variety of approaches, stabilizing and functionalizing LM nanoparticles in aqueous solution for a variety of applications using simple and true nanoparticulation remains a challenge.

Among these methods, we use the combination of physical methods and chemical modifications as an excellent candidate for adjusting the properties of LM, especially for rapid and large-scale production. For physical methods, sonication is always used to downsize and nano particularization of LM. Sonication can stabilize LM nanoparticles and reduce their size. At the same time, graft molecules such as surfactants and polymers are added to the LM suspension during the sonication process to achieve the purpose of inhibiting surface oxidation, enhancing biocompatibility, and providing binding sites for functional molecules.[15] However, many grafting molecules are easily detached from their surface due to the low dispersibility of LM. As they interact with LM via weak van der Waals forces, ionic interactions, or both, after the washing process, owing to removement of excess grafting molecules, they form to incompetent LM aggregations.[10] Therefore, choosing a suitable dispersion stabilizer or enhancing the binding of grafting molecules to LM is required.

Biocompatible or biodegradable polymers, such as polyethylene glycol and polyvinyl alcohol, are often used for modification of nanoparticles for medicinal applications because of their low toxicity. However, synthetic polymers might cause unexpected side effects including harsh anaphylactic shock by accelerated blood clearance phenomenon.[16, 17] In addition, these polymers basically require thiolate as a functional group to conjugate with LM surface via covalent metal-thiolate bonding. The synthesis of biocompatible and biodegradable polymer-based thiolates needs complicated multistep using expensive materials. Moreover, thiol compounds are easily oxidized and inactivate metalloenzymes in biological body, resulting in side effects and toxicity.[18] As a result, developing a new molecular design and method for LM bio-nanotechnology that uses highly biocompatible natural materials is critical.

High energy can be used to initiate free radical-based reactions in solids, liquids, or gases, especially gamma (γ)-rays from ^{60}Co sources. Through cross-linking reactions, aqueous treated with γ-rays is commonly used to stabilize nanoparticles made from natural or manufactured polymers and proteins. The γ-ray radiation cross-linking process is frequently utilized in the pharmaceutical industry to synthesize polymer hydrogels.[19, 20] The advantage of γ-ray radiation is that it will not dramatically alter the chemical structure of the base molecules, allowing the original properties of the materials to be preserved, such as biocompatibility and mechanical stability. In addition, For the LM nanoparticles we developed, the experimental stage contains many cell experiments and biological experiments. During the crosslinking under the γ -ray radiation, it can sterilize the media of reaction at the same time. Furthermore, since most of the chemical cross-linking agents are harmful, one more advantage is this method does not require any cross-linking agent to complete the cross-linking reaction. These features are of great significance to our development of LM nanoparticles, especially for biomedical applications.

Since LM nanoparticles have strong photothermal conversion capabilities in the near-infrared (NIR) region, they can be used as photosensitizer in the photothermal therapy (PTT) to achieve the application of eliminating tumors. LM nanoparticles have been used in PTT to achieve tumor treatment, affording better NIR photothermal efficacy.[5, 9, 15] In addition, owing to the enhanced permeation and retention (EPR) effect, nanoparticles with 20−400 nm diameters can accumulate in tumor tissues for a long time[21], which provides the possibility for LM nanoparticles modified by bioimaging contrast agent to achieve clear fluorescent tumor visualization.

2.1.3 Objective of this study

In this study, we intend to produce a new type of functional liquid metal nanoconjugates as an innovative therapeutic material to treat cancer. To this end, we decide to use highly biocompatible gallium-indium eutectic alloys (EGaIn) and various biomolecules such as gelatin, deoxyribonucleic acid, lecithin, and bovine serum albumin for preparation unique core-shell nanostructures by utilizing γ-ray exposure. In particular, further modified with DyLight^{TM} 800 NHS ester on the surface of gelatin-EGaIn, these nanoconjugates can have property of bioimaging. In addition, synthesized nanoconjugates absorb biological penetrable NIR light to generate thermal energy thanks to the photothermal property of EGaIn. We thus apply these multifunction of nanoconjugates for cancer treatment.

2.2 Materials and Methods

2.2.1 Nanoparticle synthesis

Gelatin (Wako Pure Chemical, Osaka, Japan) (10 mg) was dissolved in MillQ water (Direct-Q UV3, Merck, Darmstadt, Germany) (10 ml) at 60 °C by heater (EYELA RCH-20L, Tokyo, Japan), then mixed with LM (Ga:In = 75.5:24.5 wt%; Alfa Aesar, Ward Hill, MA, USA) (10 mg) by pulse-type sonication (VCX-600; Sonics, Danbury, CT, USA) for 10 min. The mixture was then irradiated with γ-rays from ^{60} Co γ-ray sources at 25°C in the dose range of 5 kGy (Gy = J/kg) at the dose rate ranging between 5 kGy h^{-1} at the Takasaki Advanced Radiation Research Institute, National Institutes for Quantum and Radiological Science and Technology (QST), Gunma, Japan. Meanwhile, a concentrated solution of γ-ray-radiated gelatin-LM nanoparticles was synthesized with centrifugation and was then used for *in vivo* experiment.

γ-ray-radiated biomolecule-LM nanoparticles (BSA-LM, lecithin-LM, and DNA-LM, respectively) were synthesized as follows: Albumin (BSA) (from bovine serum, Wako Pure Chemical, Osaka, Japan) (10 mg), Lecithin (from soybean, Nacalai Tesque, Kyoto, Japan) (10 mg), or deoxyribonucleic acid (DNA) sodium salt (from salmon milt, Tokyo Chemical Industry, Tokyo, Japan) (10 mg) was dissolved in MillQ water (10 ml) to make solution. Then mixed with LM (10 mg) by pulse-type sonication for 10 min. And irradiated with γ-rays in a similar manner to the γ-ray-radiated gelatin-LM nanoparticles.

Gelatin-LM nanoparticles containing DyLight^{TM} 800 NHS easter (DyLight800-gelatin-LM) were prepared as follows. Briefly, 10 ml γ-ray-radiated gelatin-LM solution (LM concentration = 10 mg ml^{-1}) was centrifuged and resuspended in 1 ml PBS buffer (Wako Pure Chemical, Osaka, Japan), then mixed with 4 ml of PBS buffer containing 50 μg of DyLight^{TM} 800 NHS easter (Thermo Fisher Scientific, Waltham, MA, USA), reacted with the sample at 4 °C overnight. The quantity of modified DyLight^{TM} 800 NHS ester on gelatin-LM was calculated using an ultraviolet-visible near-infrared (UV−vis−NIR) spectrophotometer (V-730 BIO; Jasco, Tokyo, Japan).

2.2.2 Characterization of LM nanoparticles

The structure and morphology of the prepared γ-ray-radiated gelatin-LM nanoparticles were observed using high-resolution transmission electron microscope (TEM) (JEM-2010; JEOL, Tokyo, Japan) at an accelerating voltage of 200 kV. Energy-dispersive X-ray spectrometric (EDS) mapping was performed using TEM (JEM-2100Plus; JEOL). The hydrodynamic diameter of γ-ray-radiated gelatin-LM nanoparticles was examined by DLS (Zetasizer; Sysmex Corporation, Hyogo, Japan). DLS diagram of γ-ray-radiated gelatin-LM nanoparticles were also measured. The optical absorbance and fluorescence (FL) of the biomolecule-LM nanoparticles and DyLight800-gelatin-LM nanoparticles were determined using UV-vis-NIR (FP-8500) and FL spectrometers (Jasco), respectively.

2.2.3 Photothermal conversion tests

γ-ray-radiated gelatin-LM nanoparticles solution (100 μl) or PBS buffer (100 μl) were irradiated with an 808 nm NIR laser (Civil Laser, Hangzhou, Zhejiang, China) at 1.2 W (~61.1 mW mm^{-2}; spot diameter, about 5 mm), 0.6 W (~30.6 mW mm^{-2}), or 0.3 W (~15.3 mW mm^{-2}) under the indicated conditions. Temperatures of solutions were measured in real-time using a temperature sensor (AD-5601A; A&D, Tokyo, Japan). Thermographic images were recorded using infrared thermography (i7; FLIR, Nashua, NH, USA).

The photothermal stability of gelatin-LM nanoparticles was determined as follows. In a vial, a 100 μl nanoparticle suspension was irradiated with an 808 nm NIR laser for 5 min at 1.2 W (~61.1 mW mm^{-2}, spot ammeter, about 5 mm). Then, diluted with Milli-Q water and measured the optical absorbance spectra by using a UV-vis-NIR spectrophotometer. Compared with the spectra of gelatin-LM nanoparticles of the same concentration before irradiation.

2.2.4 Cell culture and viability test

Human normal diploid fibroblast (MRC5) and murine colon carcinoma (Colon 26) were obtained from the Japanese Collection of Research Bioresources Cell Bank (Tokyo, Japan). The MRC5 cell lines was cultured in Dulbecco's Modified Eagle's Medium (DMEM, Gibco, Grand Island, NY, USA) containing 10% FBS, 2 mM L-glutamine, 1 mM sodium pyruvate, gentamycin, penicillin-streptomycin (100 IU/ml), and Hank's balanced salt solution (Life Technologies, Carlsbad, CA, USA). The Colon26 cell line was cultured in Roswell Park Memorial Institute (RPMI) 1640 Medium (Gibco, Grand Island, NY, USA) containing 10% fetal bovine serum (FBS), 2 mM L-glutamine, 1 mM sodium pyruvate, gentamycin, and penicillin-streptomycin (100 IU ml^{-1}). Cells were maintained at 37 °C in a humidified chamber containing 5% CO_2 and were cryopreserved in multiple vials in liquid nitrogen. Cell stocks were regularly revived to avoid the genetic instabilities associated with high passage numbers.

To assess *in vitro* cytotoxicity of γ-ray-radiated gelatin-LM nanoparticles, normal human cells (MRC5) and cancer cells (Colon26) were pre-seeded overnight in 96-well plates at a density of 5×10^3 cells/well. 100 μl of cell culture medium containing different concentrations (62.5, 125, 250, 500, and 1000 μg ml^{-1}) of γ-ray-radiated gelatin-LM nanoparticles were cocultured with these adhered cells for 24 h. Thereafter, cells were washed with fresh medium and the viability was measured using a Cell Counting Kit (CCK-8) (Dojindo Laboratories, Kumamoto, Japan) according to the manufacturer's instructions. Briefly, cells (5×10^3 cells/well) were seeded in 96-well plates and were allowed to adhere overnight. After washing with fresh medium, cells were incubated with the CCK-8 solution for 2 h at 37 ºC. Absorbance at 450/690 nm was then determined using a microplate reader (Infinite 200 PRO M Plex; Tecan, Männedorf, Switzerland).

RIPA lysis buffer (Wako Pure Chemical, Osaka, Japan) was used as a positive control without further dilution for the cellular viability assay.

2.2.5 Laser-induced cell viability test

MRC5, and Colon26 cells were seeded in 96-well plates at a density of 5 × 10^3 cells/well. After adhering overnight, the cells were administered 100 μl of cell culture medium containing different concentrations (100, 500, and 1000 μg ml^{-1}) of γ-ray-radiated gelatin-LM nanoparticles with 808 nm laser irradiation at a power of 1.2 W (~61.1 mW mm^{-2}) for 5 min. The control was conducted without γ-ray-radiated gelatin-LM nanoparticles. After laser irradiation, the γ-ray-radiated gelatin-LM nanoparticles were washed away, and then the cells were sub-cultured with fresh medium for another 24 h. Further, the cell viability was assayed using the CCK-8 kit according to the indicated protocol.

2.2.6 Direct observation of laser-driven cancer cell destruction

Colon26 cells (2.5 × 10^5 cells/ml) were seeded in bioimaging dishes and cultured overnight. A PBS suspension of gelatin-LM nanoparticles (LM concentration: 100 μg ml^{-1}) was prepared, or PBS was added to the cells for 2 h in a 5% CO_2 incubator at 37 °C. After washing three times with PBS, the cells were maintained in RPMI media. The destruction of cancer cells triggered by laser induced nanomedicine using the laser irradiation setup was performed as follows. An 808 nm, 254 mW (~129 mW mm^{-2}) NIR laser beam from a continuous-wave diode laser (Sigma Koki, Tokyo, Japan) was incorporated into a microscopy system (IX73; Olympus, Tokyo, Japan). The laser beam (laser spot diameter 50 mm) was focused on the target position (× 40 magnification; aperture 0.95; UPLSAPO40X, Olympus) at room temperature for 5 s. The images were recorded using an electron-multiplying, charge-coupled device camera system (DP80, Olympus) before and during irradiation.

2.2.7 Fluorescent bio-imaging

The animal experiments were conducted in accordance with the protocols approved by the Institutional Animal Care and Use Committee of JAIST (No. 01-002). In order to monitor the chronological changes of FL intensity caused by the tumor targeting effect of γ-ray-radiated gelatin-LM nanoparticles in mice, Colon26 tumor-bearing mice (female; 6 weeks; n = 4; average weight = 18 g; average tumor size = 100 mm^3; BALB/cCrSIc; Japan SLC) were injected intravenously with PBS or PBS containing DyLight800-gelatin-LM nanoparticles (200 μl, 100 mg ml^{-1}). The mice were euthanized and the major organs, including heart, liver, spleen, kidney, and tumor, were imaged using an *in vivo* FL imaging system (VISQUE™ InVivo Smart- LF, Vieworks, Anyang, Republic of Korea) with a 3 s exposure time and indocyanine green (ICG) filter (Ex, 740-790 nm; Em, 810-860 nm) at 4, 24, and 48 h after injection. The FL images were acquired and analyzed using CleVue™ software. PBS buffer (200 μl) was also injected and used as a negative control.

2.2.8 *In vivo* viability test

Female BALB/cCrSlc mice (n = 12; 4 weeks old; average weight = 15 g) were obtained from Japan SLC (Hamamatsu, Japan). Mice bearing the Colon26 cell derived tumors were generated by injecting 100 μl of the culture medium/Matrigel (Dow Corning, Corning, NY, USA) mixture (v/v = 1:1) containing 1×10^6 cells into the right side of backs of the mice. After approximately 1 week, when the tumor volumes reached ~100 mm^3, the mice were intravenously injected with 200 μl PBS or 200 μl PBS containing γ-ray-radiated gelatin-LM nanoparticles (100 $mg\ ml^{-1}$), respectively. The tumors on the right side of the backs were irradiated for 5 min every other day (total 6 times laser irradiation) using the 808 nm laser (0.6 W, ~29.7 $mW\ mm^{-2}$) after sample injection. The irradiation location of a laser beam was fixed on the center of a solid tumor by a clamp. The thermographic measurements were conducted during irradiation using IR thermography (i7; FLIR, Nashua, NH, USA). The tumor formation and overall health (viability and body weight) were monitored every other day. Further, the tumor volume was calculated using $V = L \times W^2/2$, where L and W denote the length and width of the tumor, respectively. The survival ratio of Colon26 tumor-bearing mice was also measured during treatments for 30 days. When the tumor volumes reached more than 2000 mm^3, the mice were euthanized as the endpoint according to the guidelines of Institutional Animal Care and Use Committee of JAIST.

2.2.9 Tumor tissues immunohistochemistry staining

The Colon26 tumor-bearing mice (n = 4) were euthanized the next day after administration of PBS/γ-ray-radiated gelatin-LM nanoparticles injection intravenously and laser irradiation. Thereafter, the tumor tissues from the different treatment groups were harvested for immunohistochemistry (IHC) staining. IHC analysis was performed by Biopathology Institute Co., Ltd. (Oita, Japan) with standard protocols. Briefly, primary tumors were surgically removed, fixed in 10% formalin, processed for paraffin embedding, and then cut into 3-4 μm- thick sections. After incubation with the primary antibody (**Table 2-1**), the sections were stained with hematoxylin and examined using light microscopy (IX73).

Table 2-1. Antibody used in IHC staining.

Antibody	Type	Source	Catalog No.	Application
Anti-digoxigenin-peroxidase	Sheep Polyclonal	Merck Millipore	S7100	Tunel

2.2.10 Blood tests

Complete blood counts (CBCs) and blood biochemical parameters were determined by Clea-Japan (Tokyo, Japan) and Oriental Yeast Co. (Tokyo, Japan). BALB/cCrSlc mice (female, 10 weeks; n = 5; average weight = 21 g; Clea-Japan) were injected with PBS containing gelatin−LM nanoparticles (200 μl, 100 mg ml^{-1} LM) or 200 μl PBS in the tail vein. Blood samples were collected from the inferior vena cava of the mice after 7 days.

2.2.11 Statistical analysis

The experiments were performed in triplicate and repeated three or more times. The quantitative values are expressed as the means ± standard error of the mean (SEM) of at least three independent experiments. The statistical differences were identified using Student's two-sided *t-test* or two-way analysis of variance (ANOVA).

2.3 Results and Discussion

2.3.1 Characterization of nanoparticles

We envision using the scheme in **Figure 2.1** to synthesize biomolecule-LM nanoparticles with unique structures. As expected, the water-immiscible LM was transformed into highly water-dispersible nanoparticles through biomolecule modification by simple pulse sonication and γ-ray irradiation process (**Figure 2.2**).

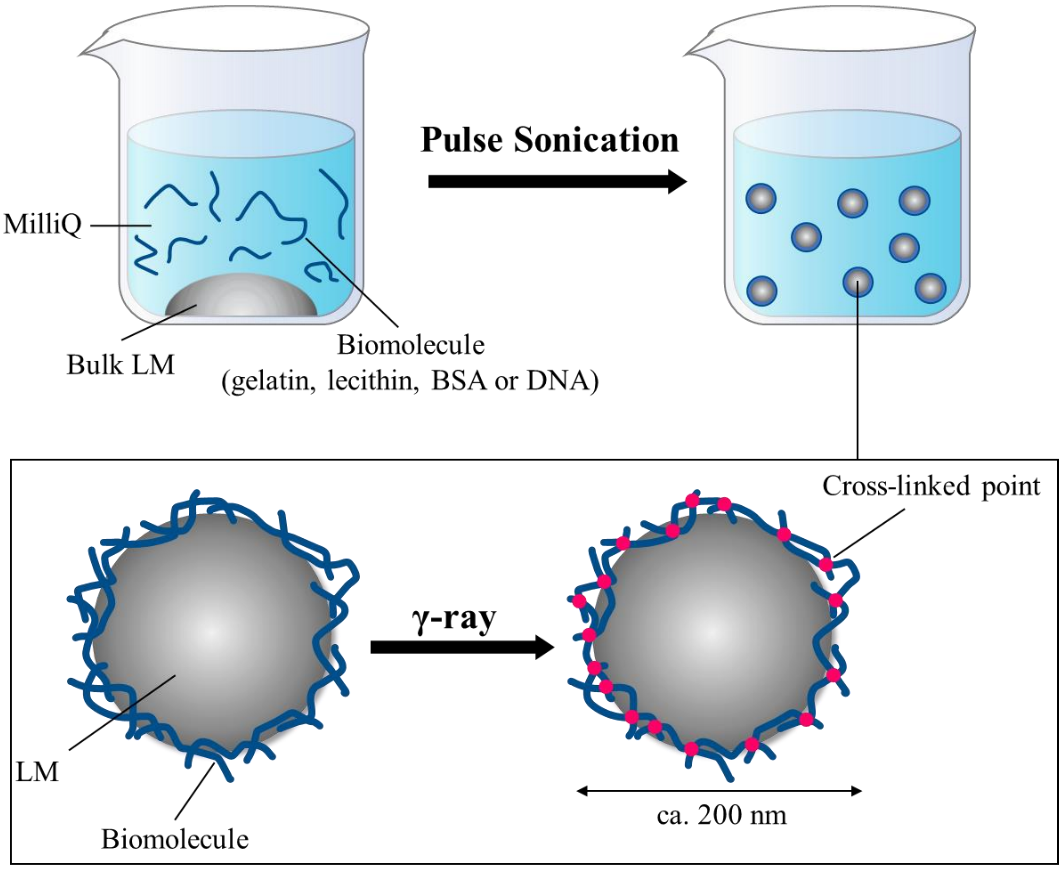

Figure 2.1 Synthesis scheme of biomolecule-LM nanoparticle.

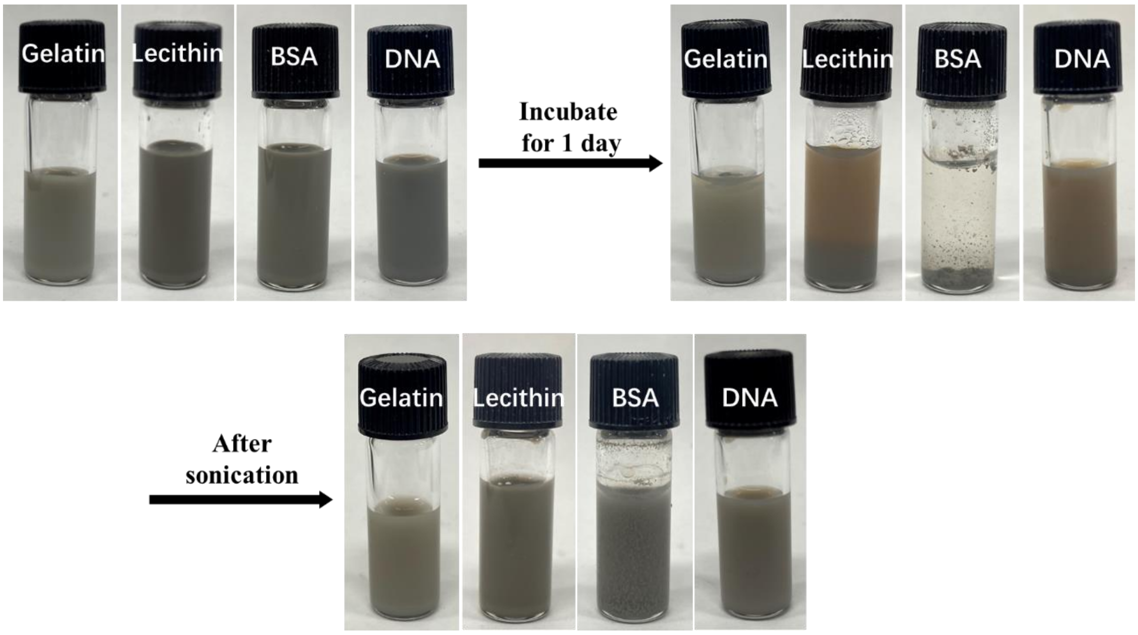

Figure 2.2 Water-dispersion stability of various biomolecule-LM nanoparticles.

As shown in **Figure 2.2**, the prepared aqueous solutions showed a gray color and did not aggregate even after washing 3 times. After incubation for 1 day at room temperature, gelatin-LM remained in a dispersed state with no visible precipitation. Lecithin-LM and DNA-LM showed characteristic gray-brown color with small precipitates after 1 day. The precipitates in the DNA-LM and lecithin-LM suspensions disappeared after sonication. BSA-LM showed many precipitates after 1 day. After sonication, precipitation of BSA-LM was still dispersed in the suspension.

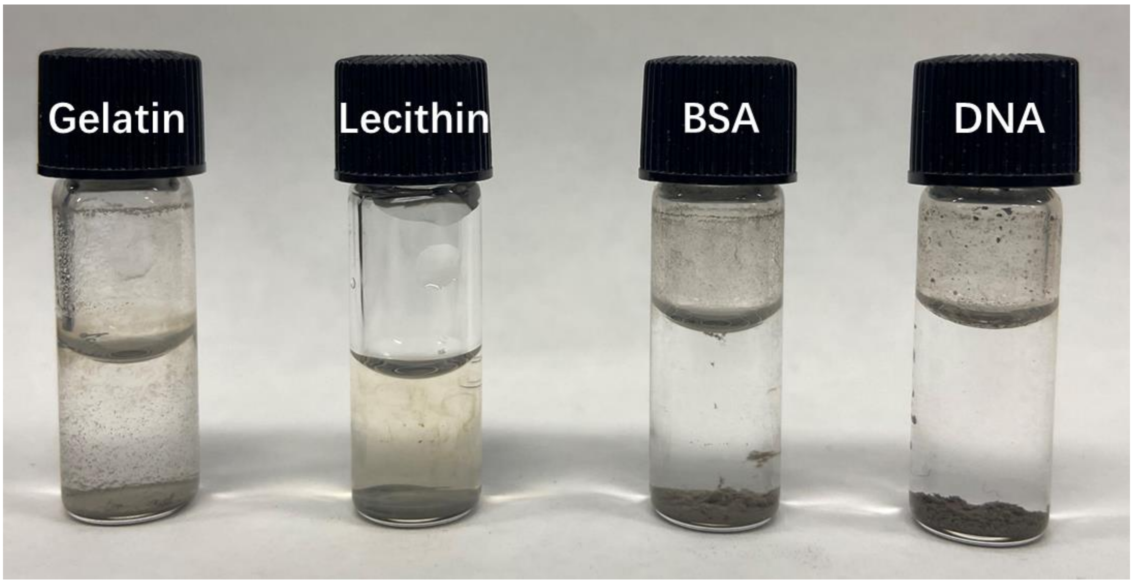

Figure 2.3 Image of biomolecule-LM nanoparticles without γ-ray radiation after washing.

Conversely, **Figure 2.3** is the image of biomolecule-LM nanoparticles without γ-ray radiation process. It shows all kinds of biomolecule-LM nanoparticles formed many precipitates after washing 3 times after incubation for several hours. This is because without γ-ray radiation, biomolecules attach to the LM surface only through weak molecular interactions, which are easily separated by washing.[22] In particular, ionic interactions between biomolecules and the LM surface oxide layer may improve molecular packing and bonding to the oxide layer, although further investigations are needed to elucidate the mechanism of interfacial interactions between oxide layers and biomolecules.

The hydrodynamic diameter of biomolecule-LM nanoparticles after 1 day incubation after sonication was measured by dynamic light scattering (DLS) test. As the results show in **Figure 2.4**, the average hydrodynamic diameter of gelatin-LM, lecithin-LM, BSA-LM, and DNA-LM were 220, 190, 295, and 106 nm, respectively. After 3 days incubation, the average hydrodynamic diameter of gelatin-LM, lecithin-LM, and DNA-LM were 220, 164, and 106 nm, respectively, which means they still maintain good dispersion and stability. In comparison, BSA-LM displays poor dispersibility and stability. The average diameter of BSA-LM increased to 712 nm after 3 days incubation even after sonication, indicating that it is unstable in aqueous solution. It might be because albumin molecules have a poorer water-dispersing stability and a tendency to aggregate.[23, 24]

Moreover, we further measured the DLS size of gelatin-LM after 30 days of incubation. The results are shown in **Figure 2.5**, as we expected, gelatin-LM with the diameter of around 190 nm maintained excellent dispersion and small diameter even after 30 days of incubation.

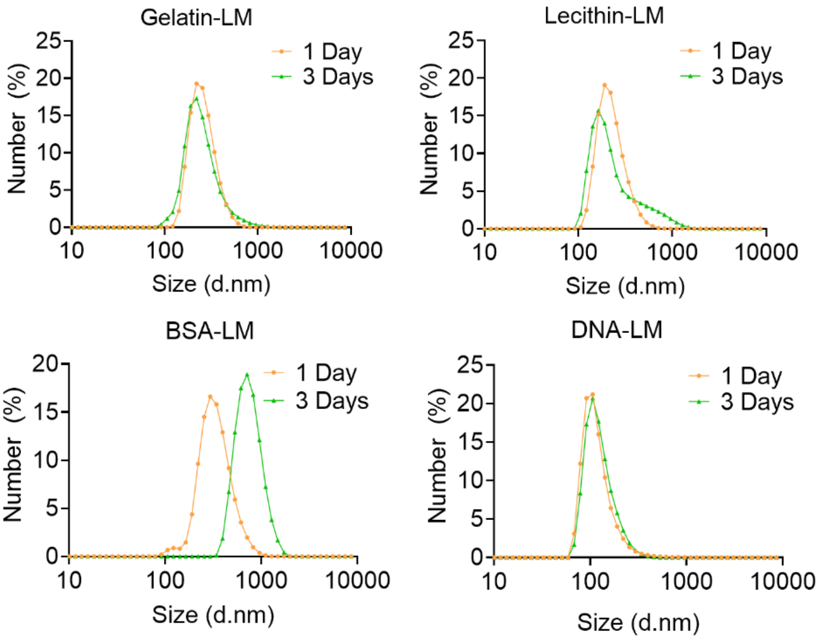

Figure 2.4 DLS size-distribution of various biomolecule-LM nanoparticles at 1 and 3 days.

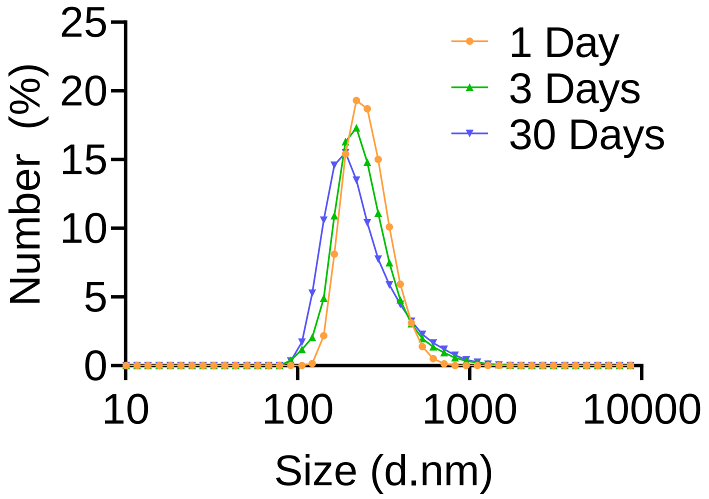

Figure 2.5 DLS size-distribution of gelatin-LM at 1, 3, and 30 days.

The transmission electron microscope (TEM) images corroborate the results of the average hydrodynamic diameter of DLS. Meanwhile, the TEM images were as expected showing the spherical structure of the biomolecule-LM nanoparticles with a unique shell structure in **Figure 2.6A, B**. The lecithin-LM, BSA-LM, and DNA-LM did not show a constant shell thickness, in contrast, the gelatin-LM nanoparticles showed a more uniform shell structure. As shown in **Figure 2.6C**, the shell thickness is around 20 nm. In addition, in the lecithin-LM, BSA-LM, and DNA-LM nanoparticles, many amorphous structural structures were found. Whereas there were a smaller number of amorphous structural structures in the gelatin-LM nanoparticles (**Figure 2.6D**). The values were obtained by measuring at least 200 nanoparticles and amorphous substrates for each sample. As a result, even after a long incubation period, gelatin-LM nanoparticles may not precipitate. Owing to the shape, size, electrical charge, molecular folding, and number of γ-ray-mediated cross-linking biometric points are very complicated. The preparation of particular size or morphology remains a challenge. We believe that nanoparticles with high dispersibility and stability are excellent candidates for biomedical materials. This is one reason why we chose gelatin-LM. Moreover, since gelatin contains a large number of amine groups, it is of great significance for anticancer drugs loading and fluorescent probes modification. Reactive amino acid residues in gelatin molecules, with the exception of phenylalanine, histidine, and tyrosine, are not destroyed by γ-ray radiation.[25] Therefore, we decided to use gelatin-LM nanoparticles for further research.

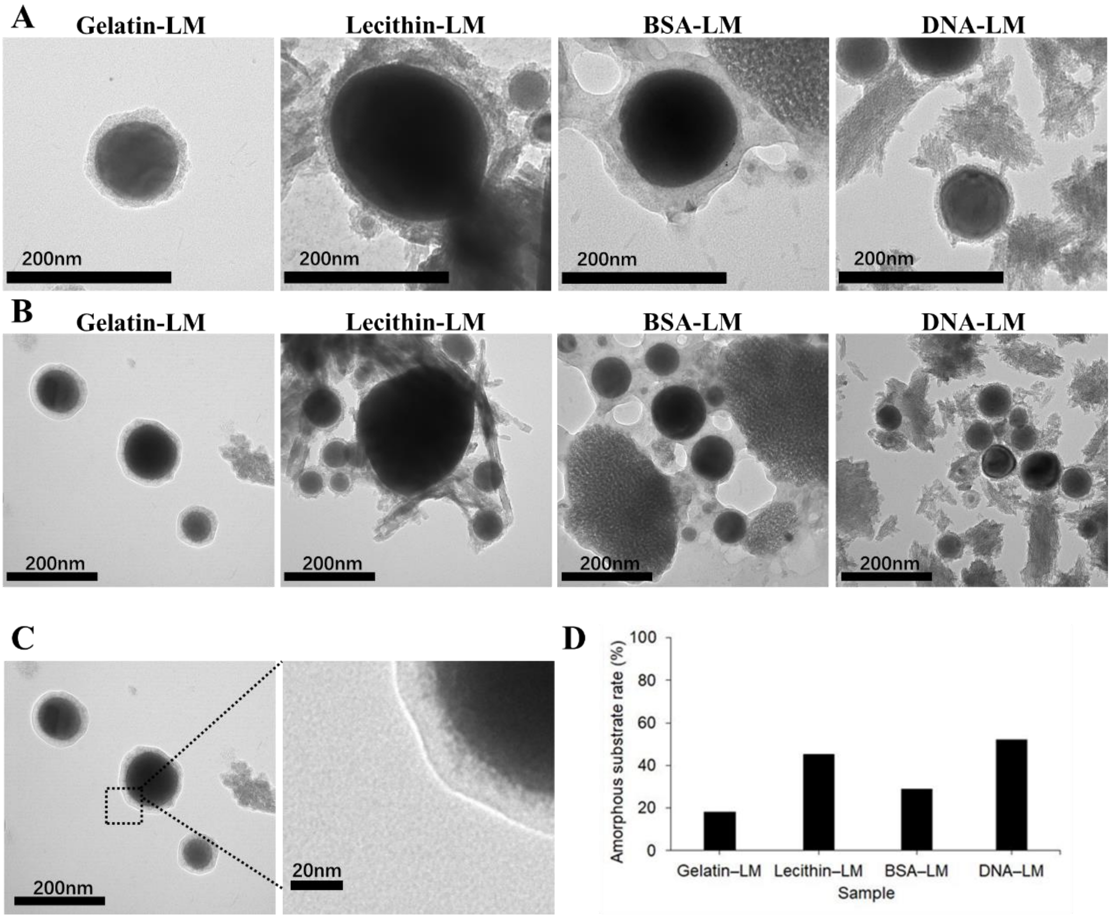

Figure 2.6. TEM image of various biomolecule-LM nanoparticles at **A)** high and **B)** low magnifications. **C)** High-magnification image of gelatin-LM shell structure. **D)** Average amorphous substrate rate in LM nanoparticles under TEM observation.

The results of energy dispersive spectrometer (EDS) mapping are shown in **Figure 2.7A**, gallium (Ga), indium (In) from liquid metal and nitrogen (N) from gelatin all showed on the gelatin-LM nanoparticles, indicating that the preparation of nanoparticles was successful. Also, the ultraviolet-visible near-infrared (UV−vis−NIR) optical absorption spectrum of different concentration (20, 40, 50, 100, and 200 μg ml^{-1}) of biomolecule-LM nanoparticles aqueous solution were measured. **Figure 2.7B** shows the absorbance change with concentration. This indicates that gelatin-LM may be employed as an optically active nanomedicine.

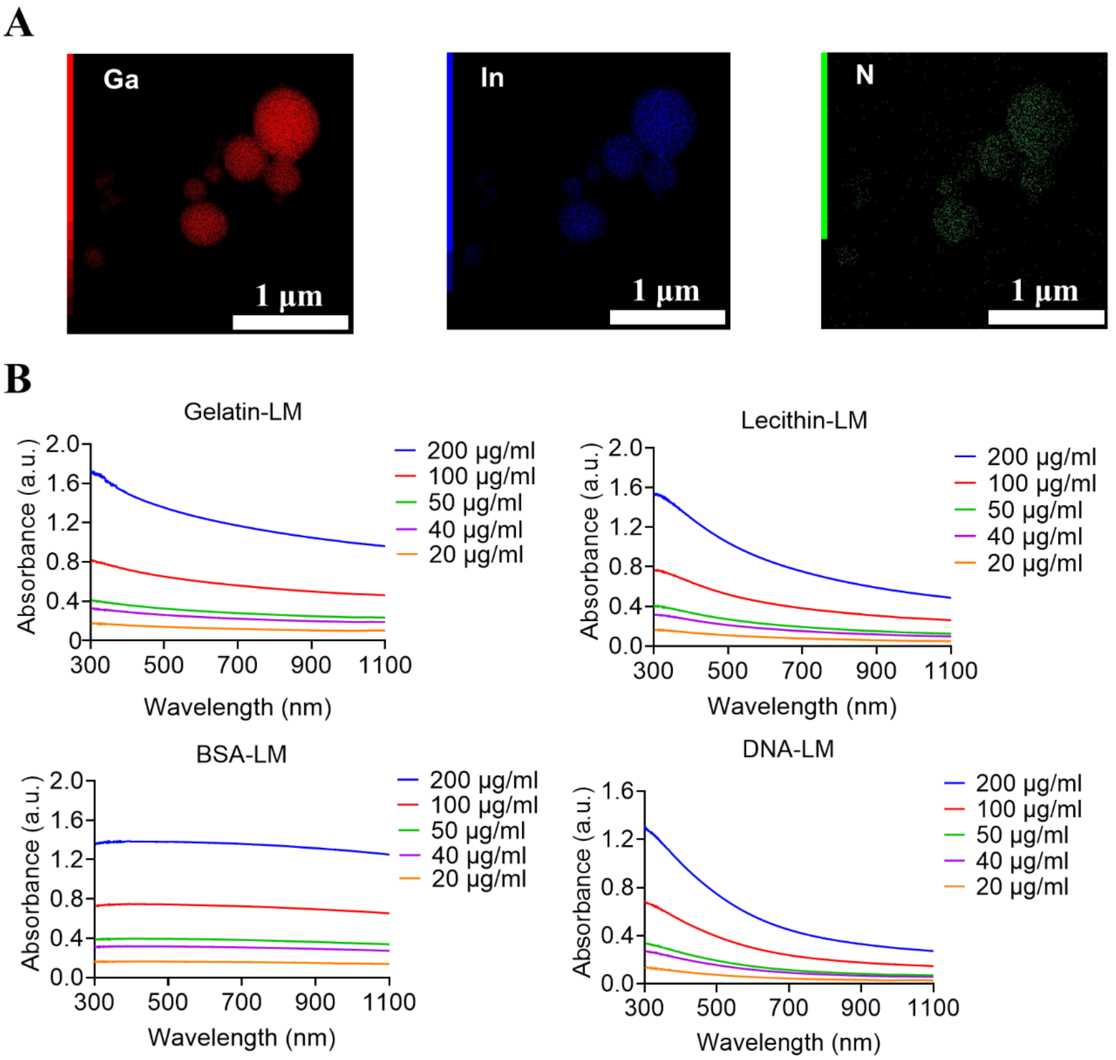

Figure 2.7 A) EDS mapping of gelatin-LM nanoparticles. **B)** UV−vis−NIR absorption spectra of biomolecule-LM nanoparticles at different concentrations.

We further characterized the photothermal conversion and characterization of gelatin-LM nanoparticles. According to the absorbance of gelatin-LM nanoparticles at

NIR wavelength, we measured the laser-induced photothermal conversion by using NIR laser irradiation (808 nm). **Figure 2.8** shows the thermographic image of the temperature change of gelatin-LM particles before and after NIR laser irradiation. Under the laser powers of 1.2 W (~61.1 mW mm^{-2}), the surface temperature of gelatin-LM solution at 1.0 mg ml^{-1} reached to 63 °C after 5 min irradiation. Meanwhile, different concentration of gelatin-LM solution (0.5 and 0.1 mg ml^{-1}) under other laser powers of 0.6 W (~30.6 mW mm^{-2}) and 0.3 W (~15.3 mW mm^{-2}) also showed a different increase in temperature after 5 min irradiation.

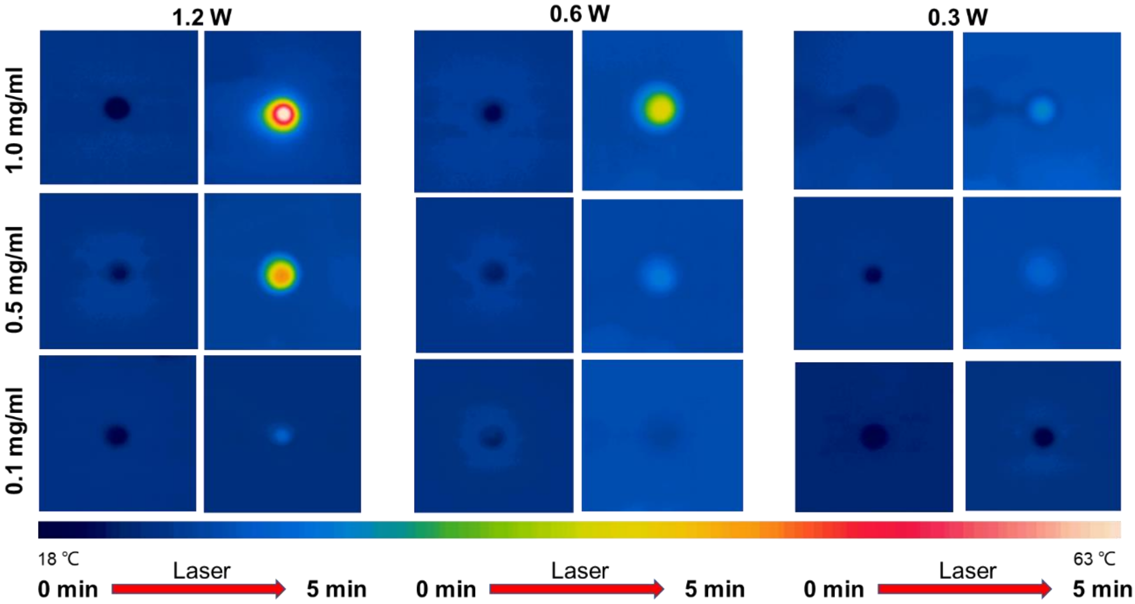

Figure 2.8 Thermographic images of various concentrations of gelatin-LM solution after 5-min laser irradiation at laser powers of 1.2, 0.6, and 0.3 W.

In addition, we measured the temperature difference (ΔT) per minute at various laser powers for various concentrations of gelatin-LM. The results show in the **Figure 2.9**, ΔT of each concentration of gelatin-LM solution increased with laser irradiation time. By adjusting the laser power and irradiation time, it provides us with the possibility to control the temperature and improve the operability of the gelatin-LM nanoparticles.

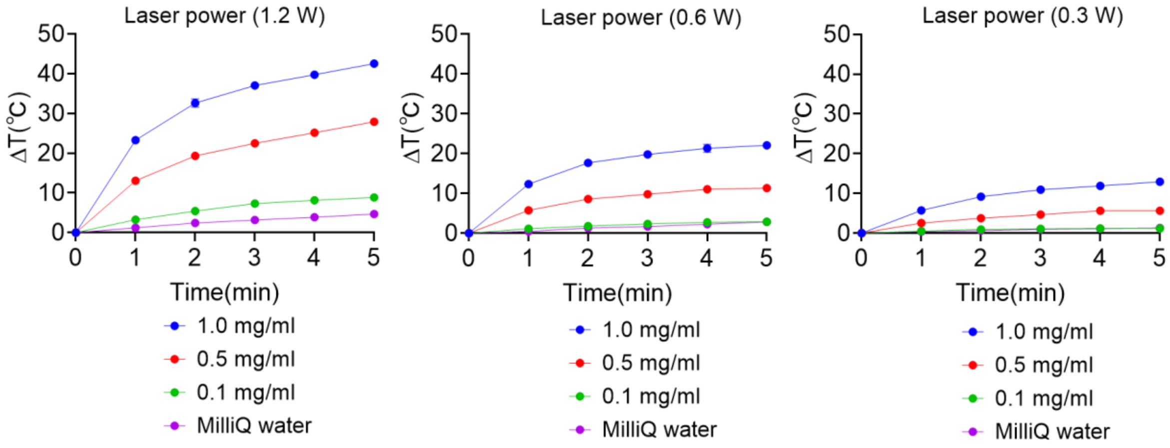

Figure 2.9 Laser-induced temperature increases in MilliQ water (control) and different concentration of gelatin-LM solution at different laser powers.

Here, the photothermal conversion efficiency of the gelatin-LM at 808 nm was 49%. In comparison, as the dates are shown in **Table 2-2**, other photothermal nanomaterials such as metal-based materials, carbon dots, and semiconductor polymer nanoparticles, have lower efficiency than gelatin-LM.[26-28] Especially, compare to other functionalized LM nanoparticles, the efficiency of gelatin-LM also shows higher except for 1,2-distearoyl-sn-glycero-3phosphoethanolamine-N-[amino(polyethylene glycol)2000] (DSPEPEG2000-amine) and 1,2-bis(10,12-tricosadiynoyl)sn-glycero3-phosphocholine (DC(8,9)PC)-functionalized LM nanoparticles (**Table 2-3**). [11, 12, 29, 30]

Table 2-2. The photothermal conversion efficiency of materials in previous reports.

Material	**Photothermal conversion efficiency (%)**	**Reference**
Gelatin–LM	49	This study
Gold nanorods	21	26
Gold nanoshells	13	26
Copper selenide	22	26
Carbon dots	31	27
Semiconducting polymer nanoparticles	37	28

Table 2-3. The photothermal conversion efficiency of LM nanoparticles in previous reports.

Material	**Photothermal conversion efficiency (%)**	**Reference**
DSPE-PEG2000-amine–DC(8,9)PC–LM	52	30
Gelatin–LM	49	This study
Melanin–LM	37	11
SH-PEG-HS–CTAB–LM	33	29
Silica–LM	22	12

The photothermal stability of gelatin-LM was measured under the thermal cycle. Under the 1.2 W (~61.1 mW mm^{-2}) power laser, gelatin-LM was irradiated and naturally cooled by six cycles. The temperature changes are shown in **Figure 2.10**, the maximum temperatures after laser irradiation were fundamentally unchanged. It is worth noting that from the second thermal cycle, the maximum temperatures are a little higher than the first one. This is due to at the end of the natural cooling process of the first cycle (at 600 s), the temperature was not cooled to the initial temperature (at 0 s). This difference disappeared from the second thermal cycle. In addition, the UV−vis−NIR optical absorption spectrum of gelatin-LM nanoparticles aqueous solution before and after laser irradiation were measured. From the spectrum in **Figure 2.11**, it shows no difference in absorbance before and after irradiation, proving that gelatin-LM is not degraded by NIR laser irradiation.

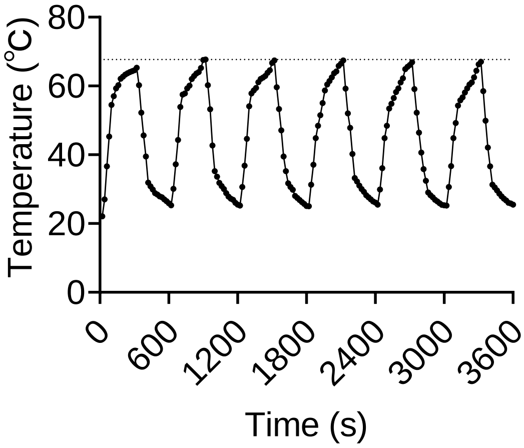

Figure 2.10 Photothermal Stability of gelatin-LM nanoparticles under the thermal cycle.

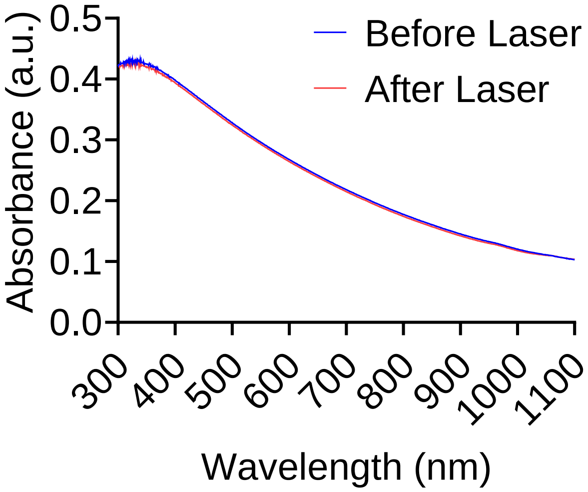

Figure 2.11 UV−vis−NIR absorption spectra of gelatin-LM before and after laser irradiation.

2.3.2 *In vitro* anticancer efficacy of gelatin-LM nanoparticle

To test the cytotoxicity of gelatin-LM nanoparticles, we did the cell viability experiment by using Colon 26 cell and MRC5 cell lines. The cells were incubated with different concentrations of gelatin-LM nanoparticles in 96-well plates for 24 h. CCK-8 was used to measure the cell viability after washing the cells to remove gelatin-LM nanoparticles from the wells. As shown in **Figure 2.12**, the gelatin-LM nanoparticles showed no cytotoxicity of all different concentrations, indicating it can be used for further *in vitro* laser-induced nanoparticle anticancer testing. As a positive control, Radio-immunoprecipitation assay (RIPA) lysis buffer was used, it showed strong cytotoxicity to both cell lines.

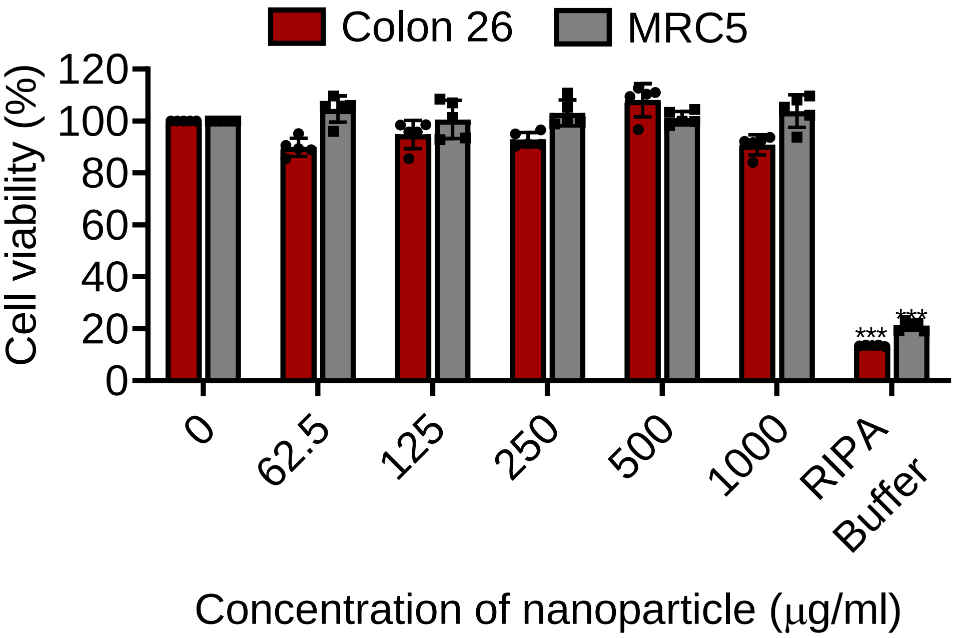

Figure 2.12 Cell viability following treatment with RIPA buffer (control) and gelatin-LM nanoparticles at various concentrations. Data presented as means ± SEM (n = 5; biologically independent tests), ***, $p < 0.001$ vs control w/o nanoparticles (Student's *t-test*).

Subsequently, we did the cancer cell elimination experiment by laser-induced gelatin-LM nanoparticles to confirm they have the ability to photothermal conversion and generate thermal energy. Similarly, Colon 26 cell and MRC5 cell lines were incubated with different concentrations of gelatin-LM nanoparticles in 96-well plates for 24 h, then used the 1.2 W (~61.1 mW mm^{-2}) power NIR laser was to irradiate the wells for 5 min. After the cell viability was measured by CCK-8, the results are shown in **Figure 2.13**. The laser-induced gelatin-LM nanoparticles exhibited a strong photothermal conversion ability, and the cell viability of Colon26 cancer cells was significantly reduced due to the thermal energy they generated. However, the groups without gelatin-LM nanoparticles showed no elimination ability to both cell lines. Notably, the cell viability of normal MRC5 cells shows higher cell viability than Colon26 cancer cells, possibly because cancer cells are usually heat-sensitive.[31] This provides evidence that laser-induced gelatin-LMs display selective anticancer effects.

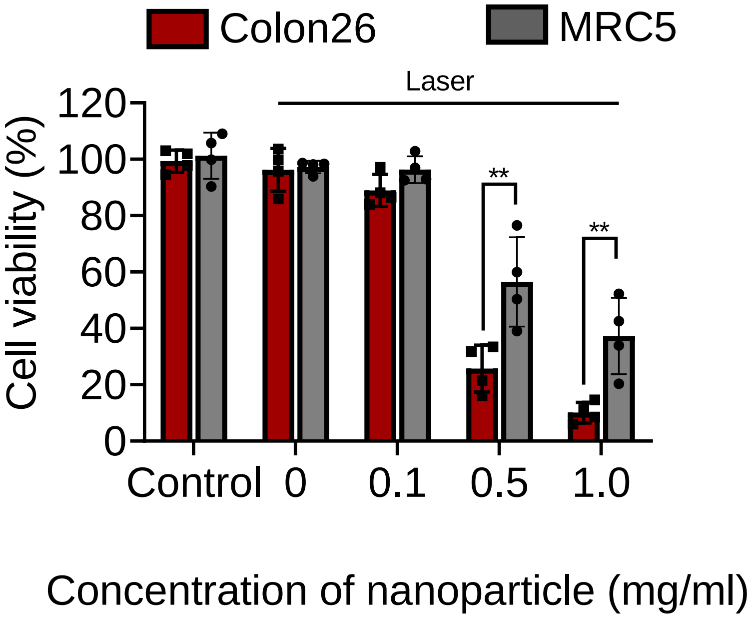

Figure 2.13 Cell viability after the treatment of 5 min NIR laser irradiation of laser-induced gelatin-LM nanoparticles at various concentrations. Data presented as means ± SEM (n = 4; biologically independent tests), **, $p < 0.01$.

Optical microscopy was used to analyze gelatin-LM internalization and distribution in Colon26 cells (**Figure 2.14**), and intracellular gelatin-LM uptake was seen in cells planted in 35 mm glass-bottom dishes and incubated with gelatin-LM for 6 hours. In the cells, black-colored gelatin-LM nanoparticles were found. Furthermore, control Colon26 cells that had not been exposed to gelatin-LM were transparent and unaggregated. Conversely, the optical microscope image demonstrated that gelatin-LM was largely localized around the cell membranes but not inside the cells after incubation of cells with gelatin-LM at 4 °C for 6 hours (**Figure 2.15**), demonstrating that cell internalization was energy dependent.[32] As a result, endocytosis could provide a route for these gelatin-LM nanoparticles to enter the cell.

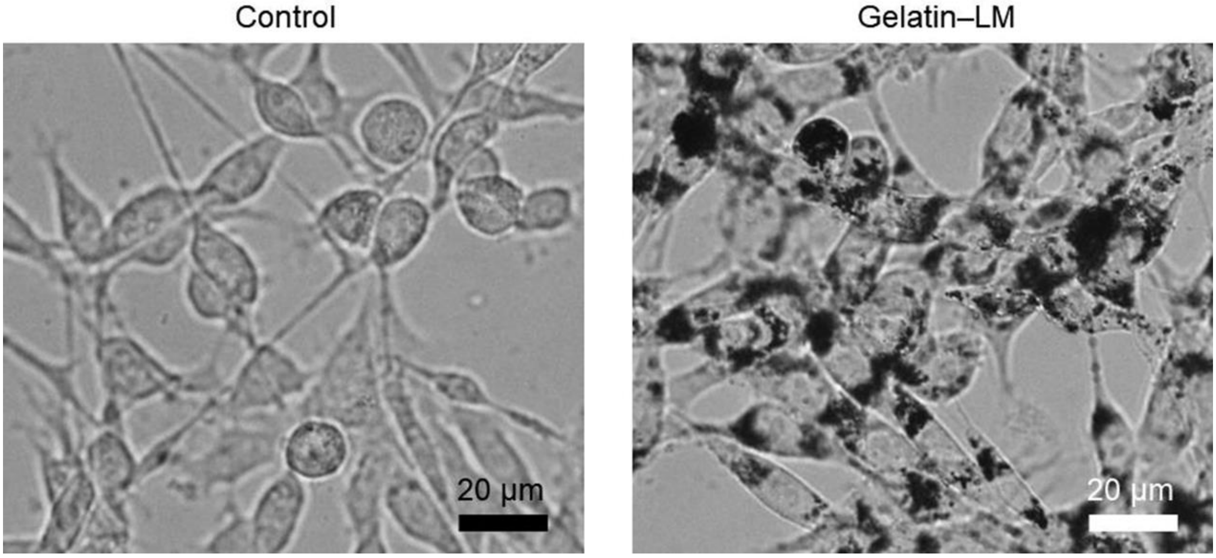

Figure 2.14 Optical micrographs of Colon26 cells after 6 h incubation with and without 0.1 mg ml^{-1} gelatin-LM at 37 °C in 5% CO$_2$.

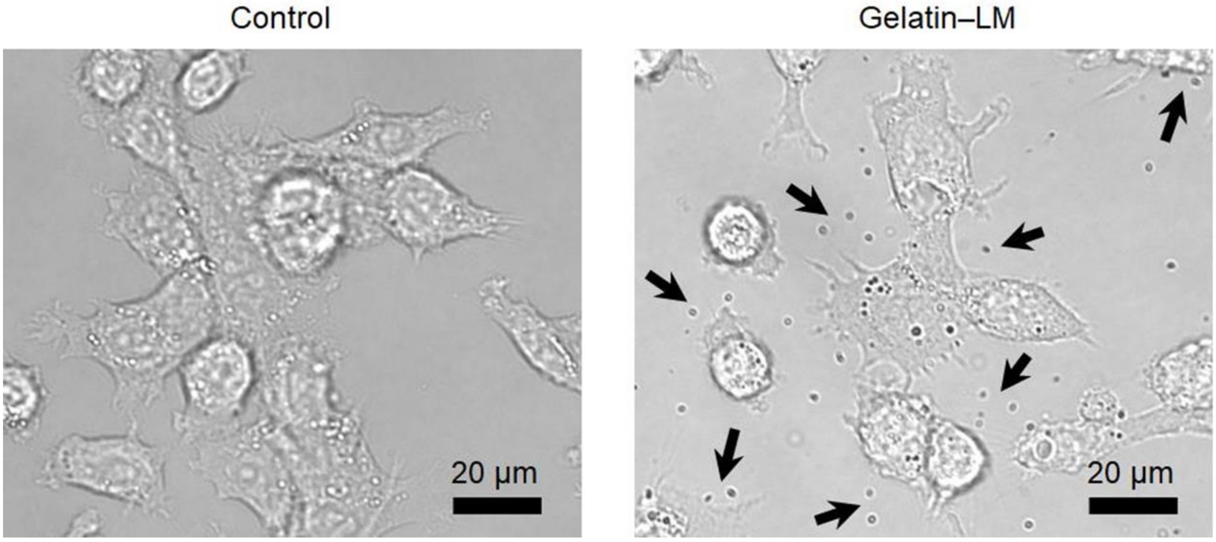

Figure 2.15 Optical micrographs of Colon26 cells after 6 h incubation with and without 0.1 mg ml^{-1} gelatin-LM at 4 °C in 5% CO_2. Black arrows show gelatin-LMs.

In addition, by using optical microscopy, we directly observed the elimination of Colon 26 cancer cells (**Figure 2.16**). When the NIR laser was irradiated (808 nm, 564 mW, ~287 mW mm^{-2}; laser time < 3 s), Colon 26 cancer cells produced bubbles and were instantly eliminated. These bubbles may be formed by the intense photothermal conversion of laser-induced LM nanoparticles through the highly focused laser beam passing through the objective, evaporating the water inside and outside the cells. Due to the boiling point of water, we estimate that the instantaneous temperature can reach above 100°C. In contrast, control cells could not be eliminated by laser irradiation because they did not contain gelatin-LM nanoparticles (**Figure 2.17**). Based on the above experimental results, we believe that the photothermal characteristics of laser-driven gelatin-LM are particularly effective in cancer elimination.

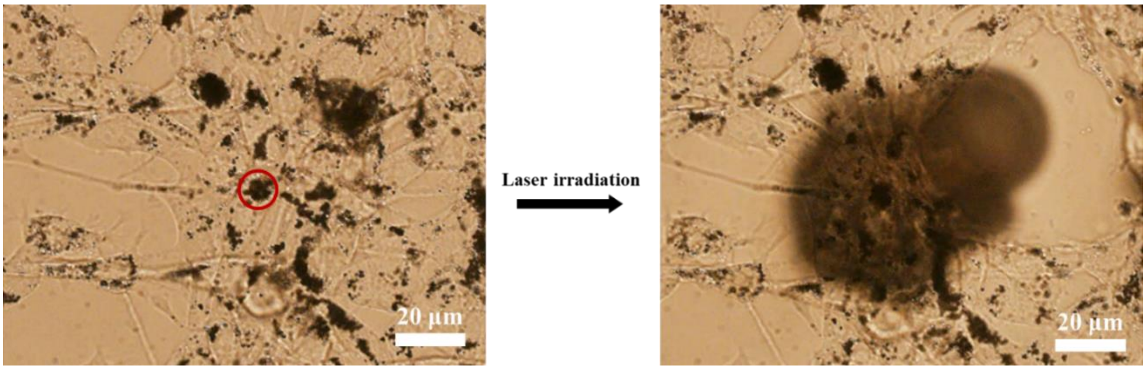

Figure 2.16 Cancer cell destruction by laser-induced gelatin-LM before and after laser irradiation. The red circle shows laser irradiation position and area.

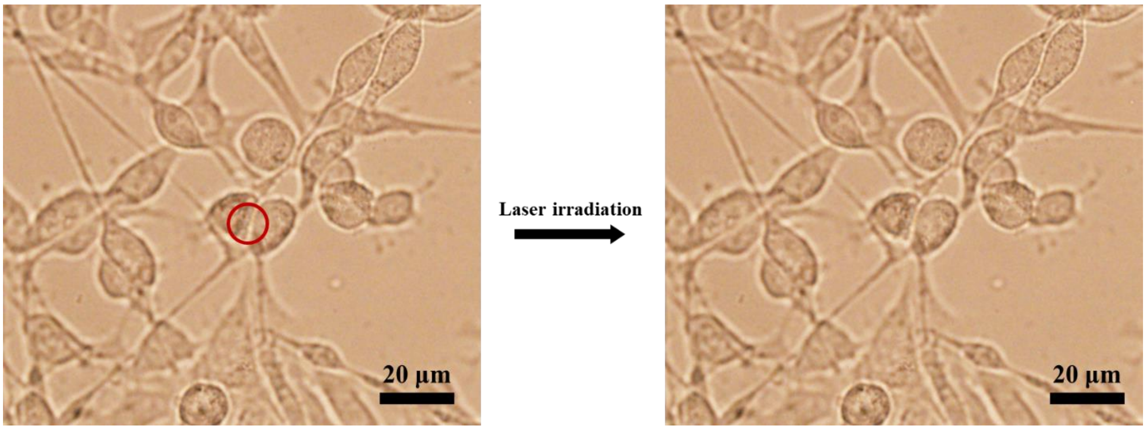

Figure 2.17 Direct observation of laser-induced cancer cell behavior without gelatin-LM before and after laser irradiation. The red circle shows laser irradiation position and area.

2.3.3 *In vivo* tumor elimination by laser-induced gelatin-LM nanoparticles

After verifying the ability of gelatin-LM to eliminate cancer cells by *in vitro* cell experiments, we started *in vivo* animal experiments subsequently. Owing to a large number of functional groups in the gelatin amino acid-residue side chain, it can conjugate with various active molecules. Here, we prepared DyLight800-gelatin-LM by condensation reaction between DyLight^{TM} 800 NHS easter and the amino group of gelatin-LM (**Figure 2.18**). We explored the distribution of gelatin-LM nanoparticles *in vivo* using the fluorescence of DyLight^{TM} 800 NHS easter under NIR wavelength.

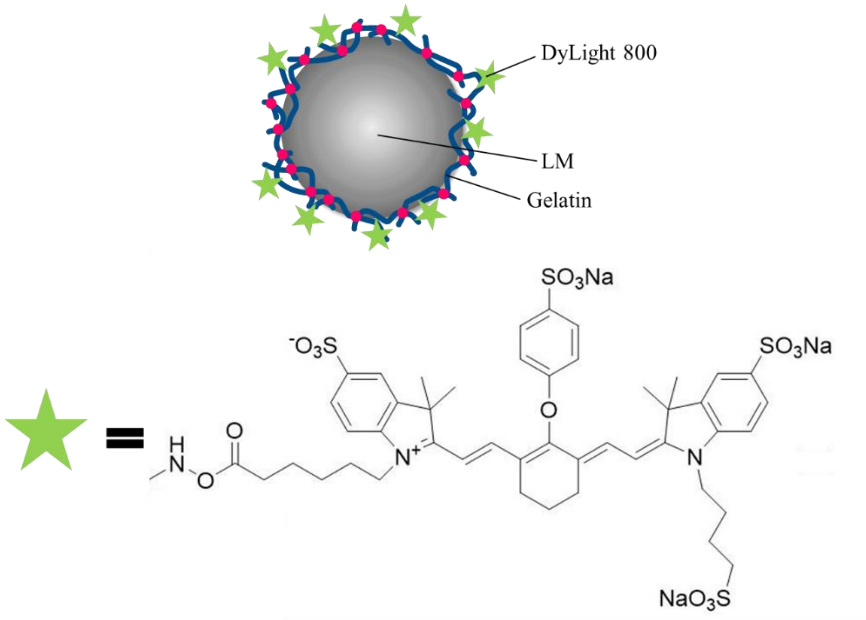

Figure 2.18 Schematic illustration of DyLight800-gelatin-LM.

The UV−vis−NIR optical absorption spectrum of gelatin-LM, DyLight800, and DyLight800-gelatin-LM was measured respectively. Calculated from **Figure 2.19**, the spectrum indicated around 4.8 nmol (~49 μg) DyLight800 reacted with gelatin-LM, which the reaction rate is 98%. Also, **Figure 2.20A** shows the fluorescence spectrum of DyLight800-gelatin-LM at various excitation wavelengths. And the comparison image of FL properties of DyLight800-gelatin-LM and gelatin-LM was taken under the NIR-exposed bioimaging (**Figure 2.20B**). The vial of DyLight800-gelatin-LM (left) showed exhibited FL that gelatin-LM (right) did not have.

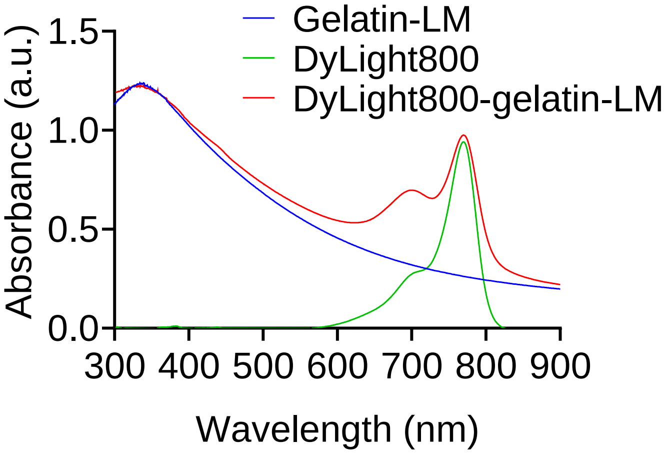

Figure 2.19 UV−vis−NIR absorption spectrum of gelatin-LM, DyLight800, and DyLight800-gelatin-LM

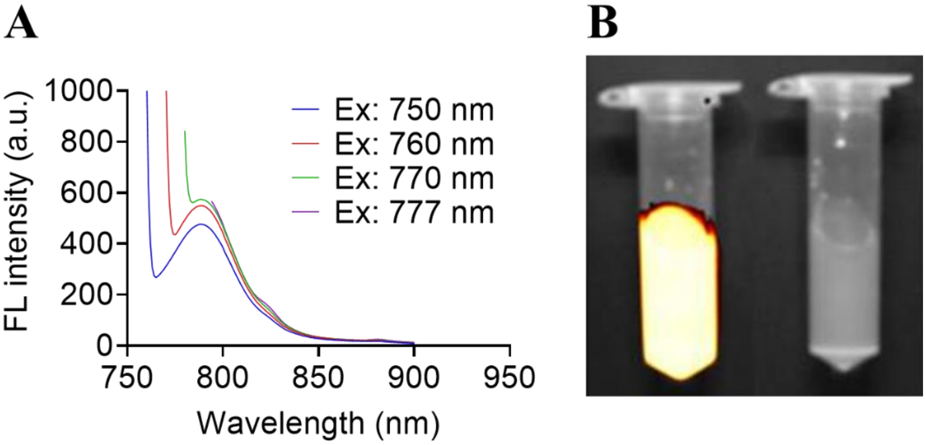

Figure 2.20 **A)** The fluorescence spectrum of DyLight800-gelatin-LM at various excitation wavelengths. **B)** Two-vial images represent DyLight800-gelatin-LM (left) and gelatin-LM (right) FL properties under NIR-exposed bioimaging.

Although the concentration of DyLight800 and LM concentrations were adjusted to the same before measurement, the DyLight800-gelatin-LM still showed a lower FL intensity than the DyLight800 (**Figure 2.21**). We speculate that during the photoinduction process, energy, or electron transfer, or both, may occur between dye molecules and metal surfaces.[33, 34]

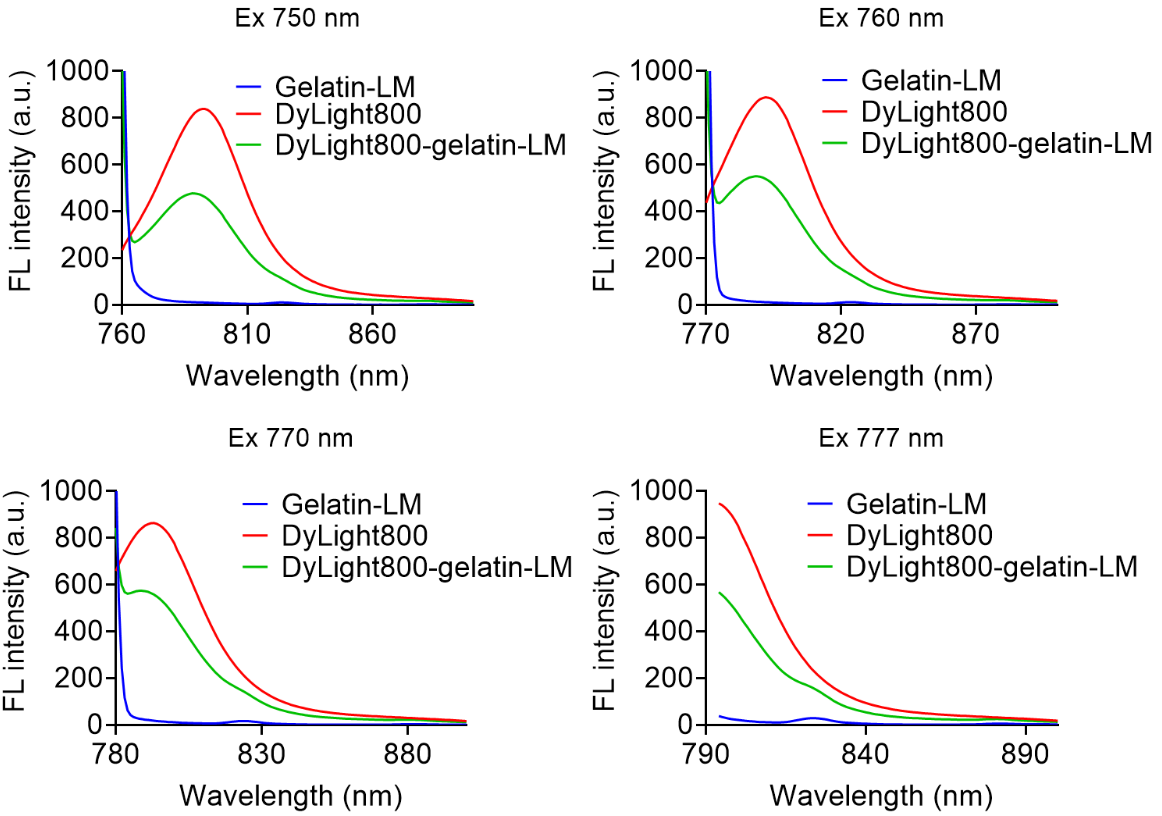

Figure 2.21 The fluorescence spectrums of gelatin-LM, DyLight800, and DyLight800-gelatin-LM at various excitation wavelengths.

As mentioned above, the EPR effect as a promising approach for effective tumor targeting[21], makes the nanoparticles with 20-400 nm diameters can stay in tumor tissues for a long period, which provides the possibility for LM nanoparticles modified by bioimaging contrast agent to achieve clear fluorescent tumor visualization, providing for clear fluorescent tumor visibility by using DyLight800-gelatin-LM nanoparticles as a bioimaging contrast agent. The DyLight800-gelatin-LM solution was intravenously injected into Colon26-bearing mice. Then, investigated the systemic pharmacokinetics of DyLight800-gelatin-LM (~200 nm diameter) using an *in vivo* NIR-bioimaging system (**Figure 2.22**).

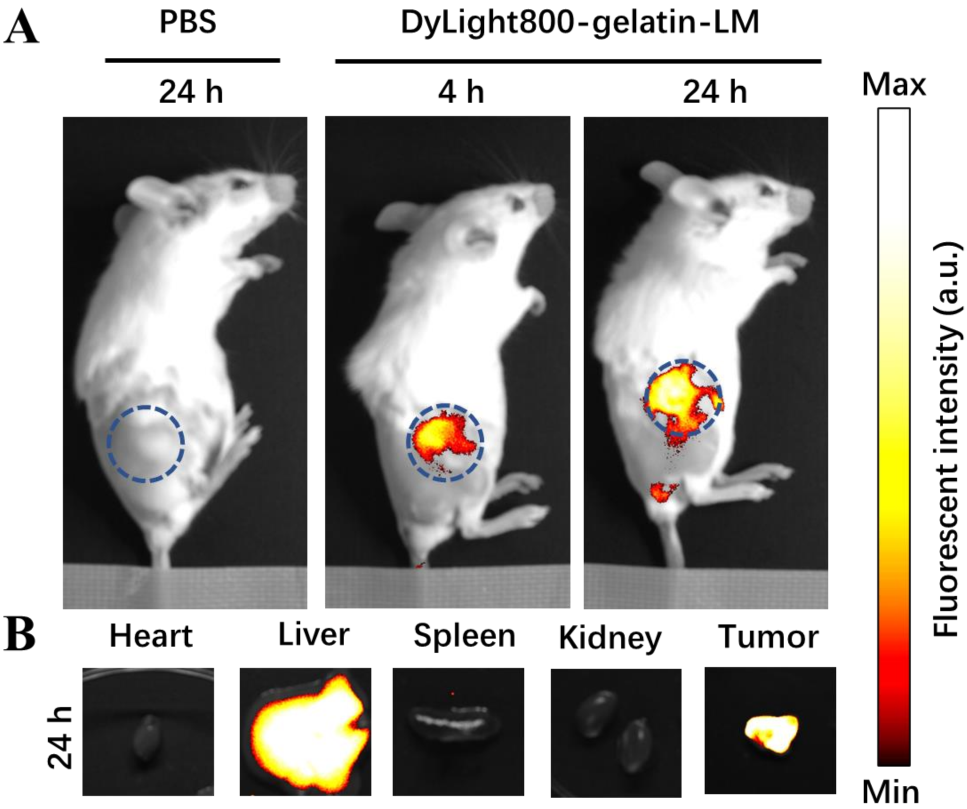

Figure 2.22 A) FL imaging of Colon26 tumor-bearing mice after an intravenous injection of DyLight800-gelatin-LM. Blue dashed circle denotes solid tumor location. **B)** FL imaging of tumor and major organs after 24 h injection.

From FL imaging, the maximum fluorescence intensity was obtained in the tumor after 4 h injection (**Figure 2.22A**), indicating that DyLight800-gelatin-LM accumulated in tumors due to a significant EPR effect. After 24 h injection, beside the solid tumor, the excised vital organs, such as the heart, liver, spleen, and kidneys displayed NIR FL which shows in **Figure 2.22B**. In addition to the tumor, the liver also exhibited relatively bright NIR FL, while other organs showed no FL.

Meanwhile, the absence of *in vivo* toxicity of gelatin-LM was also confirmed, which was further confirmed by blood tests (**Table 2-4**). After 7 days, there was no statistically significant difference in the CBC or biochemical parameters of mice intravenously injected with PBS or gelatin-LM nanoparticle dispersion.

Table 2-4 CBCs and biochemical parameters of the mice injected with PBS or γ-ray-radiated gelatin-LM nanoparticle dispersion after 7 days.

Measured value	Entry	Unit	PBS (n = 5)	Gelatin-LM (n = 5)	P value
CBC	WBC	$\times 10^2$ /μL	58.67 ± 4.16	55.00 ± 1.41	> 0.05
	RBC	$\times 10^4$ /μL	839.60 ± 44.64	857.00 ± 65.19	> 0.05
	HGB	g/dL	12.20 ± 0.77	12.60 ± 0.96	> 0.05
	HCT	%	39.32 ± 2.17	40.18 ± 2.75	> 0.05
	MCV	fL	46.82 ± 0.27	46.90 ± 0.50	> 0.05
	MCH	pg	14.52 ± 0.23	14.70 ± 0.19	> 0.05
	MCHC	g/dL	31.02 ± 0.40	31.36 ± 0.42	> 0.05
	PLT	$\times 10^4$ /μL	68.38 ± 5.95	66.02 ± 9.42	> 0.05
Biochemical parameters	TP	g/dL	3.96 ± 0.13	3.90 ± 0.20	> 0.05
	ALB	g/dL	2.80 ± 0.17	2.72 ± 0.22	> 0.05
	BUN	mg/dL	20.28 ± 0.79	21.75 ± 4.27	> 0.05
	CRE	mg/dL	0.08 ± 0.01	0.10 ± 0.01	> 0.05
	Na	mEq/L	150.80 ± 1.34	151.80 ± 1.30	> 0.05
	K	mEq/L	3.72 ± 0.59	3.28 ± 0.51	> 0.05
	Cl	mEq/L	119.20 ± 1.79	119.20 ± 1.30	> 0.05
	AST	IU/L	54.50 ± 6.36	55.40 ± 9.10	> 0.05
	ALT	IU/L	35.50 ± 3.54	39.40 ± 13.03	> 0.05
	LDH	IU/L	259.33 ± 64.50	231.00 ± 72.76	> 0.05
	AMY	IU/L	1800.40 ± 312.12	1841.00 ± 24.04	> 0.05
	CK	IU/L	175.20 ± 107.48	170.40 ± 115.24	> 0.05

Data are represented as means ± standard errors of the mean (SEM.); n = 5 biologically independent mice. Statistical analyses comprise the Student's two-sided *t test*.

Abbreviations: ALB, albumin; ALT, alanine transaminase; AMY, amylase; AST, aspartate aminotransferase; BUN, blood urea nitrogen; Cl, chlorine; CK, creatine kinase; CRE, creatinine; HCT, hematocrit; HGB, hemoglobin; K, potassium; LDH, lactate dehydrogenase; MCH, mean corpuscular hemoglobin; MCHC, mean corpuscular hemoglobin concentration; MCV, mean corpuscular volume; Na, sodium; PLT, platelet; RBC, red blood cell; TP, total protein; WBC, white blood cell.

These results indicated that strong DyLight800-gelatin-LM NIR FL might be used to visually identify tumor location. The optical phenomena could aid in the development of cancer phototherapy, which uses simultaneous laser irradiation and fluorescence observation to eliminate tumors.

The *in vivo* assessments of the therapeutic efficacy of laser-induced gelatin-LM were further investigated using a syngeneic tumor model. According to **Figure 2.23**, when tumor volumes reached 100 mm^3 after Colon 26 cells transplantation, 200 µl gelatin-LM (100 mg ml^{-1}) or PBS was intravenously injected into Colon26-bearing immunocompetent mice. After 24 h injection, the solid tumors were irradiated using the 808nm NIR laser at 0.6 W (~30.6 mW mm^{-2}) for 5 min. Simultaneously, the surface temperature of solid tumors was monitored by using a thermographic camera during the laser irradiation at 0, 1, 3, and 5 min. As shown in **Figure 2.24**, the surface temperatures of the solid tumors in the mice were approximately 34 °C without laser irradiation. In comparison, due to the EPR effect, gelatin-LM nanoparticles accumulated in the solid tumor and generated heat, the surface temperature of the solid tumors of mice injected gelatin-LM nanoparticles can reach around 53 °C after 5 min 808 nm NIR laser irradiation. Notably, under the NIR laser irradiation, PBS-injected mice also displayed a temperature increase, possibly because skin, blood, and tissue converted light energy to heat. Though, a photosensitizer's dark toxicity is a major issue in laser-based anticancer treatment, particularly photodynamic therapy. As mentioned earlier, the temperature increase caused by the optical properties of gelatin-LM nanoparticles can be completely controlled by the power of the NIR laser and irradiation time, avoiding dark toxicity.[35]

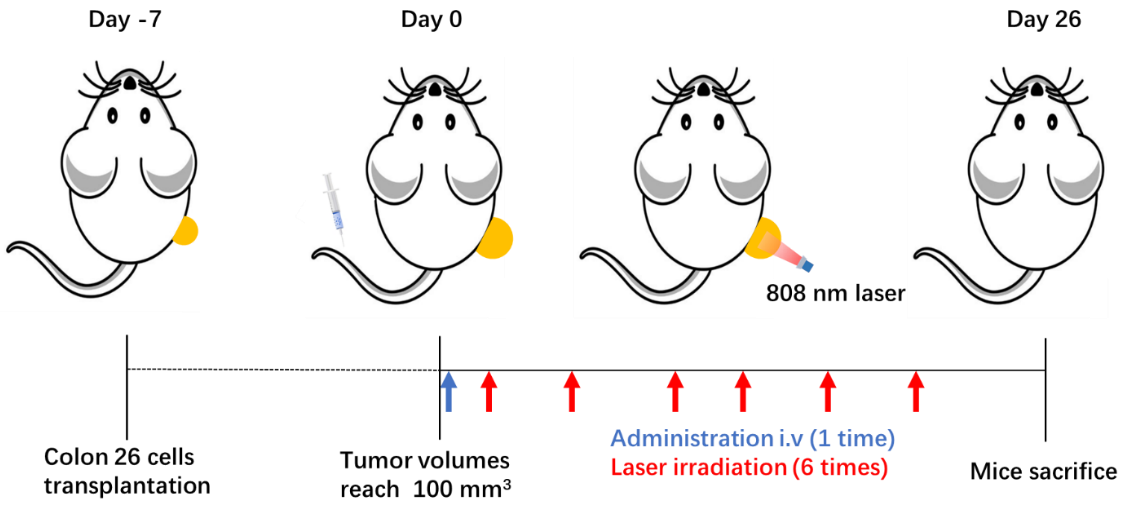

Figure 2.23 Experimental design of photothermal therapy using gelatin-LM in syngeneic tumor models.

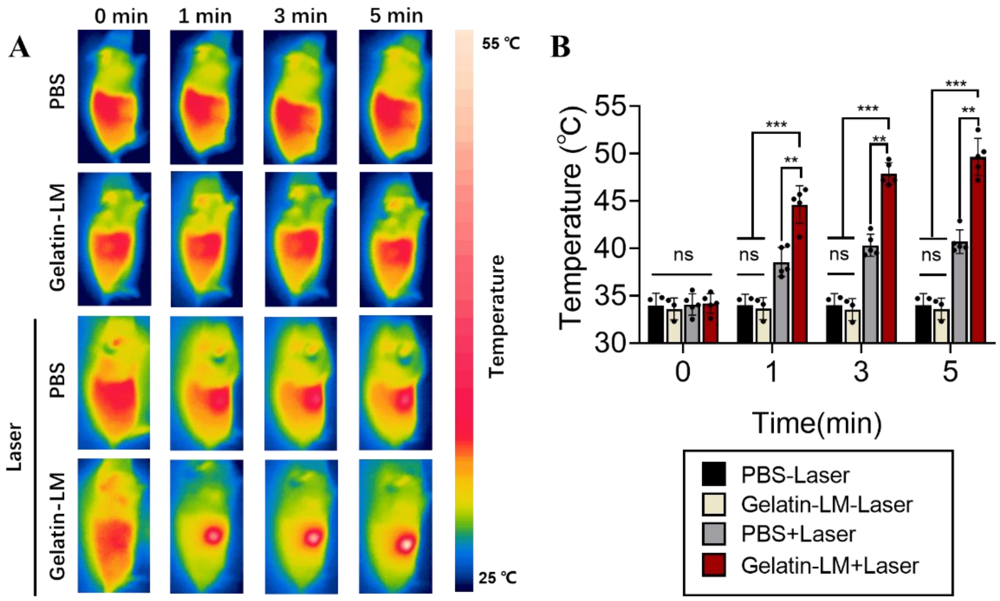

Figure 2.24 A) Infrared thermal images of whole-mouse bodies with and without laser irradiation. **B)** Solid tumor surface temperature of Colon26-bearing mice under 808 nm laser irradiation. Data represented as means ± SEM; n = 5 independent experiments. ns,

not significant; **, $p < 0.01$, and ***, $p < 0.001$.

Furthermore, under regular laser irradiation, due to the excellent photothermal conversion of gelatin-LM nanoparticles, solid tumors were ablated on d-10 (**Figure 2.25**). Although it might have a potential slight burn of the skin on the tumor, on d-26, the scar from the burn had sloughed off (**Figure 2.26**). Importantly, it indicates the laser-induced gelatin-LM nanoparticles are effective for photothermal therapy of cancer.

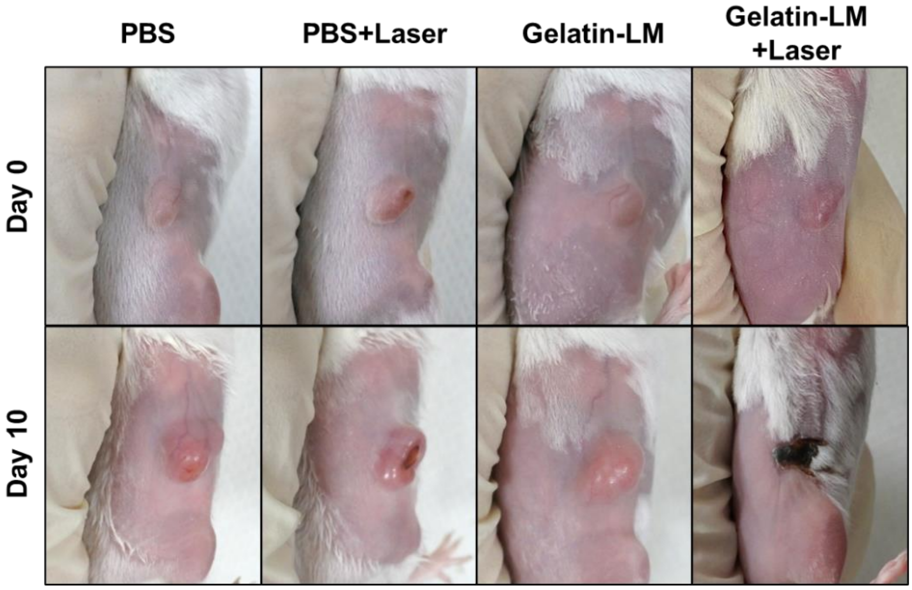

Figure 2.25 Mouse images after 0 and 10 d intravenous PBS injection and gelatin-LM with and without tumor laser irradiation.

Figure 2.26 Gelatin-LM injected mouse image at d-26.

In addition, the body weight and tumor volume of the mice of PBS ± Laser and gelatin-LM ± Laser group were measured every other day respectively (**Figure 2.27**). As shown in **Figure 2.27A**, tumor volume of PBS ± Laser and LM – Laser group continued to increase with days, whereas LM + Laser group showed a decreased tumor volume under NIR laser treatment. The mice body weight of all groups increased steadily over time during the experiment, demonstrating no side effects (**Figure 2.27B**).

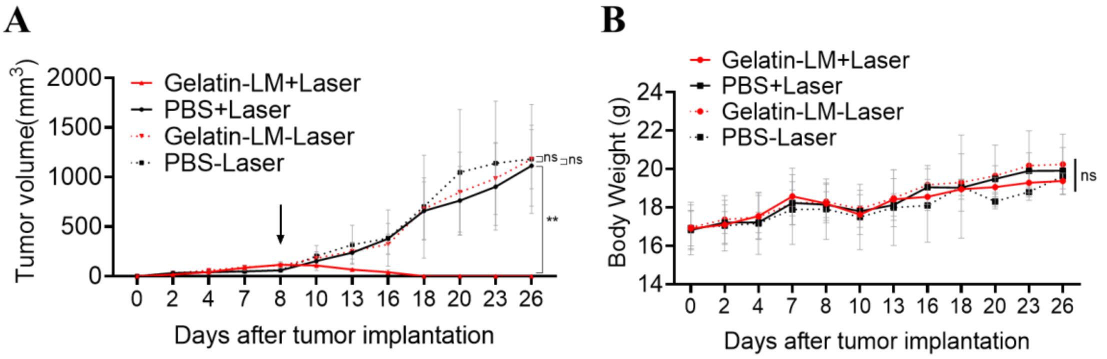

Figure 2.27 A) Average solid tumor size changes under the *in vivo* anticancer effect of NIR laser-induced LM nanoparticles. **B)** Average body weight of mice after treatment. Data presented as means ± SEM (n = 5 biologically independent tests). ns, not significant; **, $p < 0.01$.

The solid tumor suppression behavior of NIR laser-induced gelatin-LM was further investigated using hematoxylin and eosin (H&E) staining and terminal deoxynucleotidyl transferase (TdT)mediated 2′-deoxyuridine, 5′-triphosphate (dUTP) nick end labeling (TUNEL) analysis (**Figure 2.28**). Only in laser-induced gelatin-LM did H&E staining demonstrate tumor destruction with intercellular fragmentation. In the control groups (PBS, PBS + Laser, and LM – Laser), representative logical traits such as tight arrangement and nuclear atypia were detected. Furthermore, cancer cell death was improved by NIR laser-induced gelatin-LM treatment, as evidenced by an increase in TUNEL-positive cells. PBS, PBS + laser, and LM control groups, on the other hand, did not show apoptotic TUNEL color development within the tumor mass. These results indicated that the strong photothermal conversion of gelatin-LM was photothermal conversion activity was a key role in antitumor effectiveness *in vivo*.

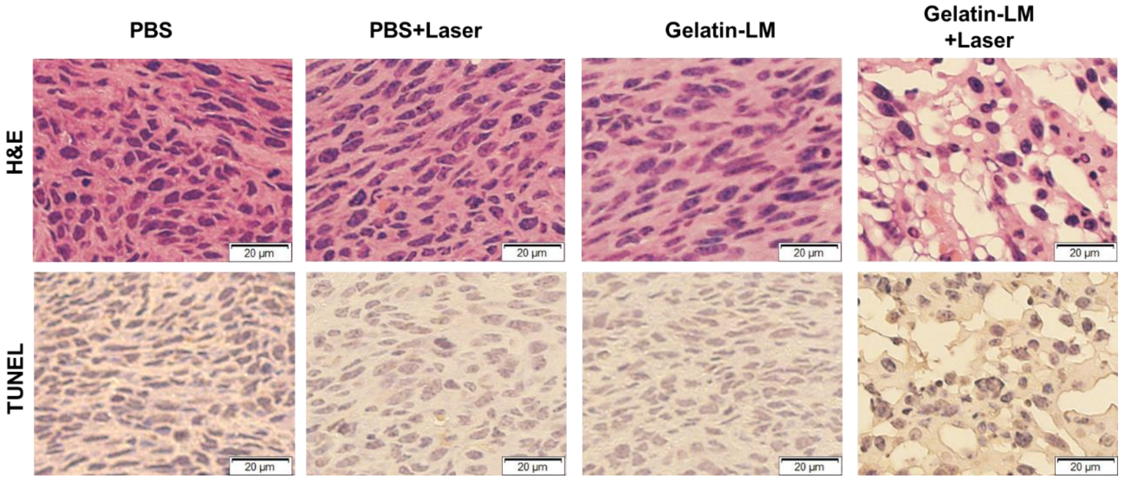

Figure 2.28 Mouse treatment-group hematoxylin and eosin- and TUNEL-stained tumor tissue on d-2.

2.4 Conclusion

In this study, we developed a series of novel functional LM nanoparticles as innovative therapeutic materials for the treatment of cancer. The unique core-shell nanostructures were prepared by γ-ray irradiation, and the characterization of LM nanoparticles modified with different biomolecules was studied for the first time. The modified gelatin-LM nanoparticles can maintain high stability and dispersibility in an aqueous solution for up to 30 days. In particular, the surface of gelatin-LM nanoparticles was further modified with DyLight^{TM} 800 NHS ester, making it useful for near-infrared bioimaging systems to identify tumor sites in mice.

Furthermore, the photothermal conversion efficiency of the gelatin-LM at 808 nm was 49%. In comparison, other photothermal nanomaterials such as metal-based materials, carbon dots, and semiconductor polymer nanoparticles, have lower efficiency than gelatin-LM nanoparticles. Especially, the efficiency of gelatin-LM nanoparticles also shows higher compared to most of other functionalized LM nanoparticles. Therefore, the laser-inducted gelatin-LM nanoparticles are of great significance for photothermal therapy of cancer due to their excellent photothermal conversion ability. During 26 days of photothermal treatment, the mice's tumors completely disappeared.

This study provides a promising strategy for advancing photothermal therapy in cancer treatment. We thus believe that these multifunctions of nanoconjugates would be available for future cancer treatment.

2.5 References

1. Dickey, M. D., Emerging applications of liquid metals featuring surface oxides. *ACS Appl Mater Interfaces* **2014,** *6* (21), 18369-79.
2. Zhang, Q.; Zheng, Y.; Liu, J., Direct writing of electronics based on alloy and metal (DREAM) ink: A newly emerging area and its impact on energy, environment and health sciences. *Frontiers in Energy* **2012,** *6* (4), 311-340.
3. Daeneke, T.; Khoshmanesh, K.; Mahmood, N.; de Castro, I. A.; Esrafilzadeh, D.; Barrow, S. J.; Dickey, M. D.; Kalantar-Zadeh, K., Liquid metals: fundamentals and applications in chemistry. *Chem Soc Rev* **2018,** *47* (11), 4073-4111.
4. Liu, J.; Sheng, L.; He, Z.-Z., *Liquid metal soft machines: principles and applications*. Springer: 2018.
5. Xie, W.; Allioux, F. M.; Ou, J. Z.; Miyako, E.; Tang, S. Y.; Kalantar-Zadeh, K., Gallium-Based Liquid Metal Particles for Therapeutics. *Trends Biotechnol* **2021,** *39* (6), 624-640.
6. Miyako, E., Convergence of Liquid Metal Biotechnologies for Our Health. *Accounts of Materials Research* **2021,** *2* (10), 858-862.
7. Yu, Y.; Miyako, E., Recent Advances in Liquid Metal Manipulation toward Soft Robotics and Biotechnologies. *Chemistry* **2018,** *24* (38), 9456-9462.
8. Yu, Y.; Miyako, E., Alternating-Magnetic-Field-Mediated Wireless Manipulations of a Liquid Metal for Therapeutic Bioengineering. *iScience* **2018,** *3*, 134-148.
9. Lu, Y.; Lin, Y.; Chen, Z.; Hu, Q.; Liu, Y.; Yu, S.; Gao, W.; Dickey, M. D.; Gu, Z., Enhanced Endosomal Escape by Light-Fueled Liquid-Metal Transformer. *Nano Lett* **2017,** *17* (4), 2138-2145.
10. Zhang, J.; Guo, R.; Liu, J., Self-propelled liquid metal motors steered by a magnetic or electrical field for drug delivery. *J Mater Chem B* **2016,** *4* (32), 5349-5357.
11. Yan, J.; Zhang, X.; Liu, Y.; Ye, Y.; Yu, J.; Chen, Q.; Wang, J.; Zhang, Y.; Hu, Q.; Kang, Y.; Yang, M.; Gu, Z., Shape-controlled synthesis of liquid metal nanodroplets for photothermal therapy. *Nano Research* **2019,** *12* (6), 1313-1320.
12. Zhu, P.; Gao, S.; Lin, H.; Lu, X.; Yang, B.; Zhang, L.; Chen, Y.; Shi, J., Inorganic Nanoshell-Stabilized Liquid Metal for Targeted Photonanomedicine in NIR-II Biowindow. *Nano Lett* **2019,** *19* (3), 2128-2137.
13. Yang, N.; Li, W.; Gong, F.; Cheng, L.; Dong, Z.; Bai, S.; Xiao, Z.; Ni, C.; Liu, Z., Injectable Nonmagnetic Liquid Metal for Eddy-Thermal Ablation of Tumors under Alternating Magnetic Field. *Small Methods* **2020,** *4* (9).
14. Bark, H.; Lee, P. S., Surface modification of liquid metal as an effective approach for deformable electronics and energy devices. *Chem Sci* **2021,** *12* (8), 2760-2777.
15. Yamaguchi, A.; Mashima, Y.; Iyoda, T., Reversible Size Control of Liquid-Metal

Nanoparticles under Ultrasonication. *Angew Chem Int Ed Engl* **2015,** *54* (43), 12809-13.

16. Cox, F.; Khalib, K.; Conlon, N., PEG That Reaction: A Case Series of Allergy to Polyethylene Glycol. *J Clin Pharmacol* **2021,** *61* (6), 832-835.
17. Abu Lila, A. S.; Kiwada, H.; Ishida, T., The accelerated blood clearance (ABC) phenomenon: clinical challenge and approaches to manage. *J Control Release* **2013,** *172* (1), 38-47.
18. Day, J. A.; Cohen, S. M., Investigating the selectivity of metalloenzyme inhibitors. *J Med Chem* **2013,** *56* (20), 7997-8007.
19. Flores-Rojas, G. G.; López-Saucedo, F.; Bucio, E., Gamma-irradiation applied in the synthesis of metallic and organic nanoparticles: A short review. *Radiation Physics and Chemistry* **2020,** *169*.
20. Kimura, A.; Jo, J. I.; Yoshida, F.; Hong, Z.; Tabata, Y.; Sumiyoshi, A.; Taguchi, M.; Aoki, I., Ultra-small size gelatin nanogel as a blood brain barrier impermeable contrast agent for magnetic resonance imaging. *Acta Biomater* **2021,** *125*, 290-299.
21. Matsumura, Y.; Maeda, H. J. C. r., A new concept for macromolecular therapeutics in cancer chemotherapy: mechanism of tumoritropic accumulation of proteins and the antitumor agent smancs. **1986,** *46* (12_Part_1), 6387-6392.
22. Lin, Y.; Liu, Y.; Genzer, J.; Dickey, M. D., Shape-transformable liquid metal nanoparticles in aqueous solution. *Chem Sci* **2017,** *8* (5), 3832-3837.
23. Stathopulos, P. B.; Scholz, G. A.; Hwang, Y. M.; Rumfeldt, J. A.; Lepock, J. R.; Meiering, E. M., Sonication of proteins causes formation of aggregates that resemble amyloid. *Protein Sci* **2004,** *13* (11), 3017-27.
24. Holm, N. K.; Jespersen, S. K.; Thomassen, L. V.; Wolff, T. Y.; Sehgal, P.; Thomsen, L. A.; Christiansen, G.; Andersen, C. B.; Knudsen, A. D.; Otzen, D. E., Aggregation and fibrillation of bovine serum albumin. *Biochim Biophys Acta* **2007,** *1774* (9), 1128-38.
25. Kimura, A.; Yoshida, F.; Ueno, M.; Taguchi, M., Application of radiation crosslinking technique to development of gelatin scaffold for tissue engineering. *Radiation Physics and Chemistry* **2021,** *180*.
26. Hessel, C. M.; Pattani, V. P.; Rasch, M.; Panthani, M. G.; Koo, B.; Tunnell, J. W.; Korgel, B. A., Copper selenide nanocrystals for photothermal therapy. *Nano Lett* **2011,** *11* (6), 2560-6.
27. Li, Y.; Bai, G.; Zeng, S.; Hao, J., Theranostic Carbon Dots with Innovative NIR-II Emission for in Vivo Renal-Excreted Optical Imaging and Photothermal Therapy. *ACS Appl Mater Interfaces* **2019,** *11* (5), 4737-4744.
28. Li, J.; Pu, K., Semiconducting Polymer Nanomaterials as Near-Infrared Photoactivatable Protherapeutics for Cancer. *Acc Chem Res* **2020,** *53* (4), 752-762.
29. Sun, X.; Sun, M.; Liu, M.; Yuan, B.; Gao, W.; Rao, W.; Liu, J., Shape tunable gallium nanorods mediated tumor enhanced ablation through near-infrared photothermal therapy. *Nanoscale* **2019,** *11* (6), 2655-2667.

30. Chechetka, S. A.; Yu, Y.; Zhen, X.; Pramanik, M.; Pu, K.; Miyako, E., Light-driven liquid metal nanotransformers for biomedical theranostics. *Nat Commun* **2017,** *8*, 15432.
31. Rossi-Fanelli, A.; Cavaliere, R.; Mondovì, B.; Moricca, G., *Selective heat sensitivity of cancer cells*. Springer Science & Business Media: 2012; Vol. 59.
32. Oh, N.; Park, J. H., Endocytosis and exocytosis of nanoparticles in mammalian cells. *Int J Nanomedicine* **2014,** *9 Suppl 1* (Suppl 1), 51-63.
33. Bhowmick, S.; Saini, S.; Shenoy, V. B.; Bagchi, B., Resonance energy transfer from a fluorescent dye to a metal nanoparticle. *J Chem Phys* **2006,** *125* (18), 181102.
34. Nasri, S.; Bardajee, G. R.; Bayat, M., Synthesis, characterization and energy transfer studies of fluorescent dye-labeled metal-chelating polymers anchoring pendant thiol groups for surface modification of quantum dots and investigation on their application for pH-responsive controlled release of doxorubicin. *Colloids Surf B Biointerfaces* **2018,** *171*, 544-552.
35. Allison, R. R.; Moghissi, K., Photodynamic Therapy (PDT): PDT Mechanisms. *Clin Endosc* **2013,** *46* (1), 24-9.

Chapter 3

Light-activatable liquid metal immunostimulants for cancer nanotheranostics

3.1 Introduction

3.1.1 Brief introduction of liquid metals

As introduced in **Chapter 2**, liquid metals (LMs), including pure gallium, gallium-based, and bismuth-based alloys, as a new class of functional soft materials with unique characteristics of low melting points and metal properties, have aroused increasing attention among multidisciplinary fields ranging from soft robotics, wearable electronics, and injectable materials to healthcare sensor and disease therapeutics thanks to their attractive features.[1-3] In particular, leveraging the combined properties of fluidity and metallic characteristics, LM nanoparticles exhibit high biocompatibility, minimal vapor pressure, and excellent photothermal conversion efficiency, making them promising candidates for a wide range of biomedical and biotechnological applications.[4-6] Among these applications, photothermal therapy using functionalized LM nanoparticles has gained attention as a noninvasive tumor treatment. This approach harnesses the potent photothermal properties of LMs to efficiently convert light into heat energy, enabling the targeted ablation of cancerous tumors upon exposure to an external light source, such as a near-infrared (NIR) laser.[7-13] LM-based photothermal therapy exhibits significant advantages compared with traditional cancer treatment because of its high specificity, repeatable treatment ability, and low adverse side effects.[14-18] Although the conjugation of LM nanoparticles with various biomolecules for cancer phototherapy has been investigated in **Chapter 2**, further complex design and facile multi functionalization of

LM nanoparticles with various bioactive molecules remain challenging.

3.1.2 Immuno-functionalization of LM nanoparticles

Recent successful immuno-functionalization of nanoparticles will enable new generations of immunomodulatory drugs that aim to improve clinical outcomes of nanoparticles in response to refractory cancer.[19-22] Immuno-functionalized nanoparticles boost the immune system's ability to recognize and destroy cancer cells, much like photothermal therapy, and offer the distinct advantage of high targeting precision. Accurate activation, effective infiltration, and integrated orchestration of various immune cells are key issues of immuno-functionalization of nanoparticles for effective immunological stimulations for innovative cancer treatment. Herein, we report a light-activatable immuno-functionalization LM nanoparticles for combining photothermal therapy with immunotherapy. The LM immunostimulants is composed of a eutectic gallium-indium (EGaIn) LM alloy and a biocompatible lipid poly(ethylene glycol) conjugated with potent immunological modulators and a fluorescent reporter molecule via self-assembly approach by simple sonication process and quick chemical reaction. Prepared LM nanoconjugates can effectively stimulate T cells and dendritic cells (DC) owing to its modified immunological modulators to elevate the innate antitumor immunity. Once systemic administration occurs, LM nanoconjugates selectively accumulate at the targeted tumor milieu through enhanced penetration and retention (EPR) effects[23], and remotely release the immunological modulator from LM nanocomplex by

NIR laser irradiation; in addition, strong photothermal conversion property of LM is activated under NIR light to induce a thorough denaturation of aggressive tumor cells. Synergistic effects of photothermal and control drug releasing properties and immunological stimulations can induce the infiltration and activation of cytotoxic T cells and DC in targeted tumors for enhanced cancer immunotherapy. The proposed design and therapeutic strategy of LM nanoconjugates have great potential to evoke antitumor immunity in a controlled manner and regulating the intratumoral and systemic immunological activities.

3.1.3 Objective of this study

In this study, we intended to develop a light-activatable immunostimulant based on EGaIn nanoparticles as an innovative therapeutic material for the treatment of cancer. It could be used for targeted delivery of therapeutics and diagnostics by intravenous injection. However, as investigated in **Chapter 2**, EGaIn LM itself is a water-immiscible material, which makes the handling and processing very problematic for nanomedicine applications. To date, many efforts have been made to prepare water-dispersible EGaIn LMs, and numerous methods for chemical functionalization of EGaIn LMs have already been reported.[24-26] Among them, surfactants are often used for functional surface modifications of EGaIn LMs in addition to certain improvement of water dispersibility of EGaIn LMs.[24] Thus, we propose a facile and effective approach to prepare water-dispersible EGaIn LM nanoparticles by the introduction of immunological modulator imiquimod (IMIQ) just by sonication process using 1,2-distearoyl-sn-glycero-3-phosphoethanolamine-N-[amino(polyethylene glycol)-2000] (DSPE–PEG$_{2000}$–NH$_2$). IMIQ is an imidazoquinoline compound that acts as a potent immunomodulator especially against DC and displays anti-angiogenic, anti-viral, anti-inflammatory, and anti-cancer properties.[27, 28] IMIQ stimulates cytotoxic T cells and exhibits synergistic antitumor activity through multiple immunological pathways. Additionally, the anti-PD-L1 antibodies on the nanoconjugates surface are expected to block the PD-L1 immune checkpoint on tumor cells. We believe that the convergence of immuno-functionalization of nanoparticles and LM technology could provide a promising modality to trigger ideal immune responses for advancing cancer immunotherapy.

3.2 Materials and Methods

3.2.1 Nanoparticle synthesis

The PEG–IMIQ–LM nanoparticles were prepared as fellows. Basically, 10 mg DSPE–PEG$_{2000}$–NH$_2$ (NOF Corporation, Tokyo, Japan), 10 mg IMIQ (Tokyo Chemical Industry, Tokyo, Japan), and 100 mg LM (Ga:In = 75.5:24.5 wt%; Alfa Aesar, Ward Hill, MA, USA) was mixed with 10 ml Milli-Q water (Direct-Q UV3, Merck, Darmstadt, Germany) by pulse-type sonication (VCX-600; Sonics, Danbury, CT, USA) for 10 min in the ice bath. Then, each 1 ml prepared nanoparticles were mixed with 1 mg Anti-PD-L1 antibody (Leinco Technologies, MO, USA) immediately to make Anti-PD-L1–PEG–

IMIQ–LM nanoparticles. The PEG–LM nanoparticles were prepared in a similar way except for adding IMIQ. In addition, highly concentrated PEG–IMIQ–LM or PEG–LM solution was prepared by increasing the amount of LM and PEG in the same ratio.

The Anti-PD-L1–PEG–ICG–IMIQ–LM were prepared as fellows. 1 mg ICG (Tokyo Chemical Industry, Tokyo, Japan) was mixed with 1 ml prepared Anti-PD-L1–PEG–IMIQ–LM solution and stirred up for 1h with dark conditions. The PEG–IMIQ was prepared by mixing 10 mg DSPE–PEG_{2000}–NH_2, 1 mg IMIQ, and 100 µl Cremophor® EL (Nacalai Tesque, Kyoto, Japan) with 900 µl Dulbecco's Phosphate-Buffered Saline (D-PBS) buffer (Nacalai Tesque, Kyoto, Japan) in bath-type sonication (CPX2800H-J; Emerson, Kanagawa, Japan) for 10min.

3.2.2 Nanoparticle structural and optical characterization

The morphology and structure of PEG–IMIQ–LM nanoparticles were observed under a high-resolution transmission electron microscope (TEM) (JEM-2010; JEOL, Tokyo, Japan) at 200 kV acceleration voltage. The TEM observations were performed by the Hanaichi UltraStructure Research Institute Co., Ltd. (Aichi, Japan). The hydrodynamic diameter of the PEG–IMIQ–LM nanoparticle was measured using dynamic light scattering (DLS) (Zetasier Nano ZS; Malvern Panalytical, UK). The optical absorbance and fluorescence (FL) of the PEG–IMIQ–LM and PEG–ICG–IMIQ–LM nanoparticles were determined using UV–vis–NIR (V-730 BIO; Jasco, Tokyo, Japan) and FL spectrometers (FP-8600 NIR Spectrofluorometer; Jasco, Tokyo, Japan), respectively.

3.2.3 Photothermal conversion

PEG–IMIQ–LM nanoparticle dispersions and MilliQ water were irradiated with an 808 nm NIR laser (Civil Laser, Hangzhou, Zhejiang, China) at [1.2 W (~61.1 mW mm^{-2}; spot diameter ~5 mm), 0.6 (~30.6 mW mm^{-2}), and 0.3 W (~15.3 mW mm^{-2})] powers under the indicated conditions. The temperature of the solutions was measured in real-time using a temperature sensor (AD-5601A; A&D, Tokyo, Japan). Thermographic images were recorded using infrared thermography (i7; FLIR, Nashua, NH, USA).

The photothermal stability of PEG–IMIQ–LM nanoparticles was determined as follows. In a vial, a 100 μL nanoparticle suspension was irradiated at 808 nm for 5 min at 1.2 W (~61.1 mW mm^{-2}, spot diameter ~5 mm), and the optical absorbance spectra were analyzed after dilution with MilliQ water using a UV–vis–NIR spectrometer.

3.2.4 Control drug releasing

Control releasing of IMIQ from laser-induced PEG–IMIQ–LM nanoparticle was performed as follows. A 100 μL PEG–IMIQ–LM nanoparticle dispersion (LM concentration = 125 μg ml^{-1}, IMIQ = 12.5 μg ml^{-1}) was irradiated with an 808 nm NIR laser at 1.2 W (~61.1 mW mm^{-2}, spot diameter ~5 mm) power for 5 min. The sumples were centrifuged before and after laser irradiation, and then measured the released IMIQ from laser-induced PEG–IMIQ–LM using a UV–vis–NIR spectrometer.

3.2.5 Cell culture and viability

Murine colon carcinoma (Colon26) and human normal diploid fibroblast (MRC5) cells were obtained from the Japanese Collection of Research Bioresources Cell Bank (Tokyo, Japan). The Colon26 cell line was cultured in Roswell Park Memorial Institute (RPMI) 1640 medium (Gibco, Grand Island, NY, USA) containing 10% fetal bovine serum (FBS), 2 mM L-glutamine, 1 mM sodium pyruvate, gentamycin, and 100 IU ml^{-1} penicillin-streptomycin. The MRC5 cells were cultured in Dulbecco's modified Eagle's medium (Gibco, Grand Island, NY, USA) containing 10% FBS, 2 mM l-glutamine, 1 mM sodium pyruvate, gentamycin, 100 IU/ml penicillin-streptomycin, and Hank's balanced salt solution (Life Technologies, Carlsbad, CA, USA). The cells were maintained at 37 °C in a humidified chamber containing 5% CO_2. They were subsequently cryopreserved in liquid nitrogen in multiple vials. The cell stocks were regularly revived to avoid genetic instability associated with high passage numbers.

Cell viability was assessed using a Cell Counting Kit (CCK)-8 kit (Dojindo Laboratories, Kumamoto, Japan) according to the manufacturer's instructions. Briefly, 5 × 10^3 cells $well^{-1}$ were seeded in 96-well plates, allowed to adhere overnight, then exposed to nanoparticles, and laser-irradiated as indicated. After washing with fresh medium, the cells were incubated with CCK-8 solution for 2 h at 37 °C. The absorbance at 450/690 nm was determined using a microplate reader (Infinite M200 PRO; Tecan, Männedorf, Switzerland).

3.2.6 Intracellular penetration of ICG–IMIQ–LM

Colon-26 cells (2.5×10^5 cells well^{-1}) were seeded in poly-L-lysine coated glass bottom dishes (Matsunami glass, Osaka, Japan) and allowed to adhere overnight. Cells were then exposed to 125 μg ml^{-1} of PEG–ICG–IMIQ–LM (ICG concentration = 12.5 μg ml^{-1}) for 24 h at 37 °C in a fridge or a humidified incubator containing 5% CO_2. After washing thoroughly with fresh PBS solution, Colon-26 cells were observed using a FL microscopy system (IX73) equipped with a mirror unit (IRDYE800-33LP-A-U01; Semrock, Lake Forest, IL, USA) and an objective (×40 magnification, aperture 0.95; UPLSAPO20X, Olympus) at room temperature.

3.2.7 Tumor spheroids

Colon-26 cells (1×10^4 cells well^{-1}) were seeded in a 3D culture spheroid plate (Cell-able® BP-96-R800; Toyo Gosei, Tokyo, Japan) according to the manufacturer's instructions provided with the plate. Cells were cultured for 7 days at 37 °C in a humidified incubator containing 5% CO_2. The medium was replaced every 2 days. Prepared spheroids were then exposed to 125 μg ml^{-1} of PEG–ICG–IMIQ–LM (ICG concentration = 12.5 μg ml^{-1}) for 24 h at 37 °C in a humidified incubator containing 5% CO_2. After washing thoroughly with fresh PBS solution, spheroids were observed using a FL microscopy system (IX73) equipped with a mirror unit (IRDYE800-33LP-A-U01; Semrock) and an objective (×40 magnification, aperture 0.95; UPLSAPO20X, Olympus) at 20 °C.

3.2.8 Direct observation of laser-driven cancer cell and spheroid destruction

Colon26 cells (2.5×10^5 cells ml^{-1}) were seeded in bioimaging dishes and cultured overnight. Meanwhile, Colon26 spheroids were prepared in a similar way to the aforementiond method. A normal saline (NS) suspension of PEG–IMIQ–LM nanoparticles (LM concentration: 500 μg ml^{-1}) was prepared, or NS was added to the cells or spheroids for 2 h in a 5% CO_2 incubator at 37 °C. After washing three times with PBS, the cells or spheroids were maintained in RPMI media. The destruction of cancer cells ans spherods triggered by laser-induced nanomedicine using the laser irradiation setup was performed as follows. An 808 nm, 254 mW (~129 mW mm^{-2}) NIR laser beam from a continuous-wave diode laser (Sigma Koki, Tokyo, Japan) was incorporated into a microscopy system (IX73; Olympus, Tokyo, Japan). The laser beam (laser spot diameter 50 μm) was focused on the target position (× 40 magnification; aperture 0.95; UPLSAPO40X, Olympus) at room temperature for 5 s. The images were recorded using an electron-multiplying, charge-coupled device camera system (DP80, Olympus) before and during irradiation.

3.2.9 *In vivo* fluorescent bio-imaging

The animal experiments were conducted following the protocols approved by the Institutional Animal Care and Use Committee of the Japan Advanced Institute of Science and Technology (JAIST) (No. 04-007). To monitor the chronological changes in FL intensity due to the Anti-PD-L1–PEG–ICG–IMIQ–LM tumor-targeting effect, Colon26 tumor-bearing mice (female; 6 weeks; n = 4; average weight = 18 g; average tumor size = 100 mm^3; BALB/cCrSIc; Japan SLC) were injected intravenously with 200 µl NS or NS containing Anti-PD-L1–PEG–ICG–IMIQ–LM (200 µl, ICG, 11.11 mg kg^{-1}; and LM, 0.56 g kg^{-1}; 200 µl, ICG, 1 mg ml^{-1}; and LM, 100 mg ml^{-1}) The mice were euthanized, and the major organs, including the heart, liver, spleen, and kidneys, in addition to the tumors, were imaged using an *in vivo* FL imaging system (VISQUE™ InVivo Smart-LF, Vieworks, Anyang, Republic of Korea) with a 3-s exposure time and an ICG filter (Ex, 740–790 nm; Em, 810–860 nm) at 4, 8, 12 and 24 h postinjection. The FL images were acquired and analyzed using CleVue™ software.

3.2.10 *In vivo* anticancer therapy

Female BALB/cCrSlc mice (n = 12; 4 weeks old; average weight = 15 g) were obtained from Japan SLC (Hamamatsu, Japan). Colon26 cell-derived mouse tumors were generated by injecting 100 µl Matrigel culture medium (v/v = 1:1; Dow Corning, Corning, NY, USA) containing 1 × 10^6 cells into the dorsal right side of the mice. After approximately 1 week, when the tumor volume reached ∼100 mm^3, the mice were intravenously injected with 200 μl NS, 200 μl NS containing Anti-PD-L1–PEG–ICG–IMIQ–LM (LM concentration = 50 mg ml^{-1}), 200 μl NS containing PEG–LM (LM concentration = 50 mg ml^{-1}), 200 μl NS containing Anti-PD-L1 (concentration = 1 mg ml^{-1}; 10 mg kg^{-1}), or 200 μl D-PBS containing PEG–IMIQ (concentration = 1 mg ml^{-1}). The dorsal right-side tumors were irradiated for 5 min every other day from 24 h after sample injection (total 6 times laser irradiation) using an 808 nm laser (0.6 W, ~30.6 mW mm^{-2}). Thermographic measurements were conducted during irradiation using infrared thermography. Tumor formation and overall health (viability and body weight) were monitored every other day. The tumor volumes were calculated using the formula $V = L \times W^2/2$, where L and W denote the length and width of the tumor, respectively. When the tumor volumes were > 1,500 mm^3, the mice were euthanized according to the JAIST Institutional Animal Care and Use Committee guidelines.

3.2.11 Immunohistochemistry staining of tumor tissues

Colon26 tumor-bearing mice (n = 5) were euthanized on the day after sample intravenous injection and laser irradiation. Subsequently, tumor tissue from the treatment groups was harvested for immunohistochemistry (IHC) staining. IHC analysis was performed by the Biopathology Institute Co., Ltd. (Oita, Japan) with standard protocols. Briefly, primary tumors were surgically removed, fixed in 10% formalin, processed for paraffin embedding, and cut into 3–4-μm sections. After incubation with the primary antibody (**Table 3-1**), the sections were stained with hematoxylin and eosin and examined using light microscopy (IX73). The areas showing positive staining in tumor tissues were analyzed using a light microscopy system (BZ-X800) and hybrid cell count and microcell count software (Keyence).

Table 3-1. Antibodies used in this study.

Antibody	Type	Source	Catalog No.	Application
CD3	Rabbit Monoclonal	Abcam	ab16669	IHC (1:100)
CD8	Rabbit Monoclonal	Cell Signaling Technology	98941	IHC (1:200)
Granzyme B	Rabbit Monoclonal	Cell Signaling Technology	44153	IHC (1:200)
CD11c	Rabbit Polyclonal	Prointech	17342-1-AP	IHC (1:200)
CD80	Rabbit Polyclonal	Bioss	bs-1479R	IHC (1:200)
CD86	Rabbit Monoclonal	Cell Signaling Technology	19589	IHC (1:200)
Cleaved Caspase-3	Rabbit Polyclonal	Cell Signaling Technology	9661S	IHC (1:100)
Anti-digoxigenin-peroxidase	Sheep Polyclonal	Merck Millipore	S7100	Tunel
TNF-α	Rabbit Polyclonal	Abcam	ab6671	IHC (1:100)
IL-6	Goat Polyclonal	R&D Systems	AF-406-NA	IHC (1:100)

3.2.12 Statistical analysis

All experiments were performed in triplicates and repeated three or more times. Quantitative values are expressed as the mean ± standard error of the mean (SEM) of at least three independent experiments. Statistical differences were identified by the Student's *t-test* or Log-rank (Mantel-Cox) test using GraphPad Prism, version 9.4.0 (GraphPad Software, Boston, MA, USA). A P value of less than 0.05 was considered statistically significant.

3.3 Results and Discussion

3.3.1 Characterization of nanoparticles

DSPE–PEG$_{2000}$–NH$_2$ is one of the useful surfactant for biomedical applications because of its high biocompatibility and excellent high versatility for improvement of water-dispersibility of various materials.[29, 30] As described, we intend to synthesize the LM immunological nanostimulators using the scheme in **Figure 3.1**. The modified LM nanoconjugates could conveniently be prepared in one simple step using conventional pulse-type sonication. As expected, the prepared PEG-coated EGaIn LM nanoparticles encapsulating IMIQ (PEG–IMIQ–LM) displayed muddy grey color and high water dispersibility (**Figure 3.2**).

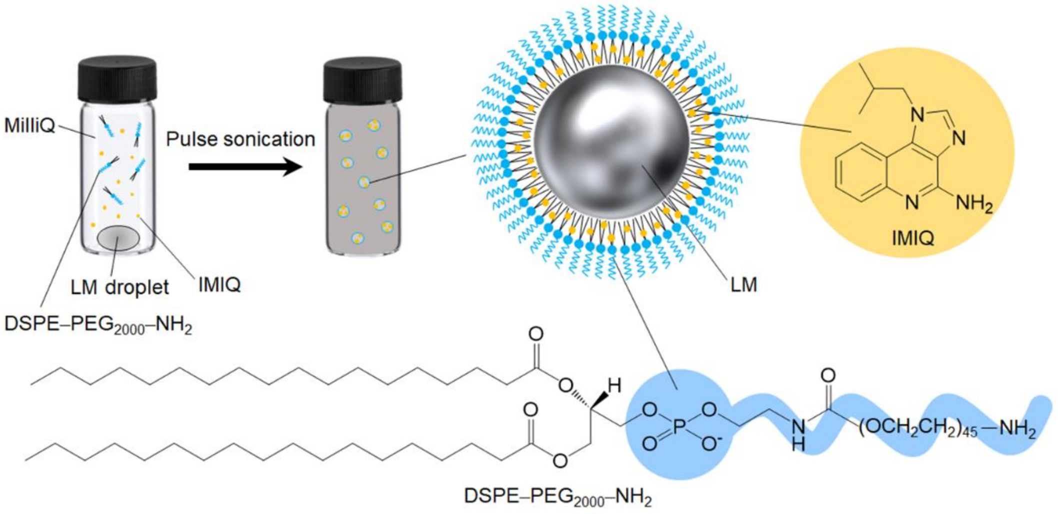

Figure 3.1 Synthesis scheme of the preparation of PEG–IMIQ–LM nanoconjugates.

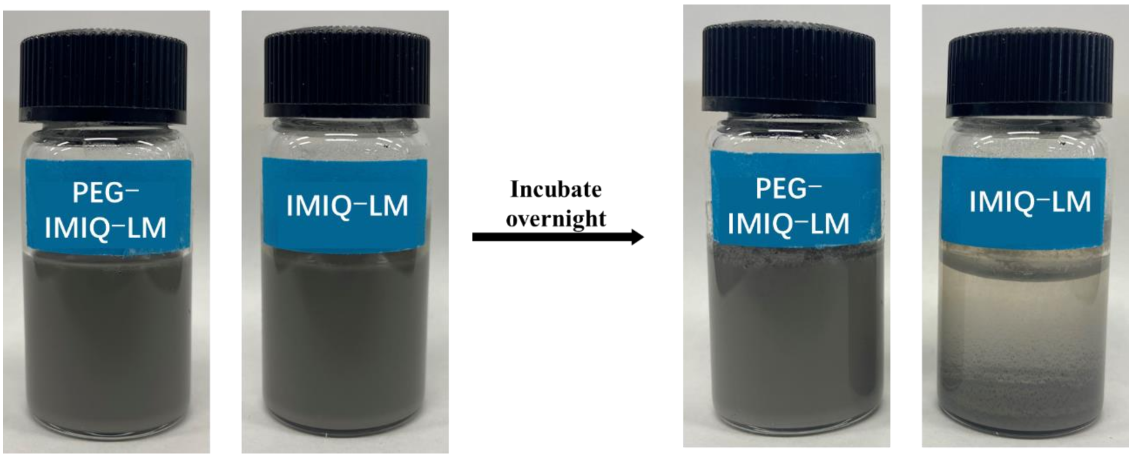

Figure 3.2 Image of the prepared PEG–IMIQ–LM and IMIQ–LM aqueous suspension.

For comparison, IMIQ–LM nanoconjugates without PEG coating were also synthesized using the same method. As shown in **Figure 3.2**, after incubated at room temperature overnight, PEG–IMIQ–LM nanoconjugates still maintained high dispersibility, while IMIQ–LM nanoconjugates lost its dispersibility and precipitated. This indicates that DSPE–PEG_{2000}–NH_2, as a surfactant, contributes greatly to the improvement of the dispersibility and stability of PEG–IMIQ–LM nanoconjugates.

The hydrodynamic diameter of PEG–IMIQ–LM nanoconjugates after 1-, 3-, and 10-day incubation after sonication was measured by dynamic light scattering (DLS) test. As the results show in **Figure 3.3**, the average hydrodynamic diameter of PEG–IMIQ–LM in 1, 3, and 10 days were 122.4, 164.2, and 190.1 nm, respectively. As expected, although the particle size slightly increased after one week of incubation, the good dispersion and nanoscale hydrodynamic diameter were still maintained.

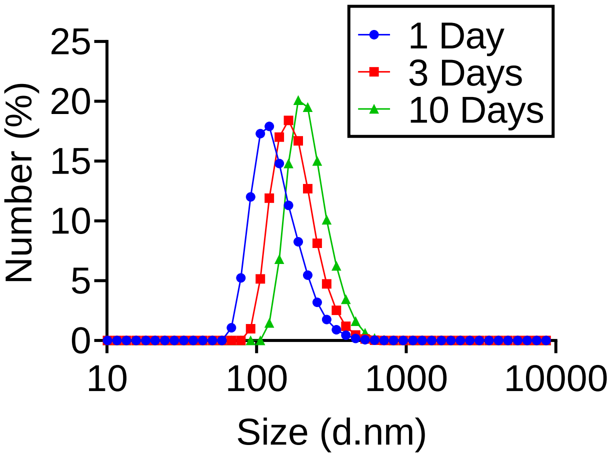

Figure 3.3 The DLS result of PEG–IMIQ–LM in 1, 3, and 10 days.

We further observed the Transmission electron microscopy (TEM) images. TEM said that spherical nanoparticles with diameter of 50~150 nm were individually distributed on a TEM grid (**Figure 3.4**). Single nanolayer (5~10 nm) derived from gallium oxide, DSPE–PEG$_{2000}$–NH$_2$, and IMIQ on LM surface was also observed under high-resolution TEM. This is consistent with the previously measured DLS results, indicating that PEG–IMIQ–LM formed a nanoscale shell structure under the encapsulation of DSPE–PEG$_{2000}$–NH$_2$.

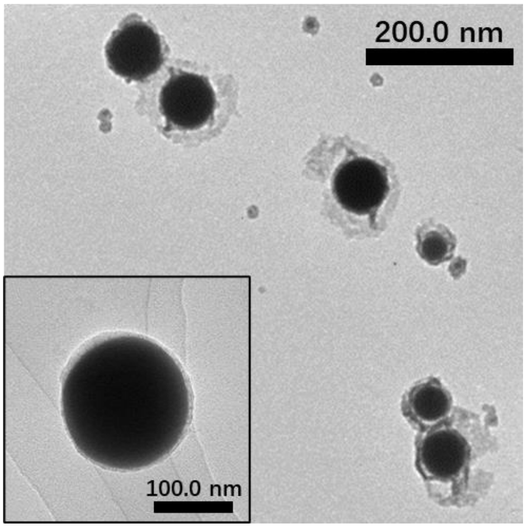

Figure 3.4 TEM images of PEG–IMIQ–LM. High-magnification image on the lower left.

Moreover, the ultraviolet–visible–near-infrared (UV–vis–NIR) optical absorption spectra of PEG–IMIQ–LM nanoparticle in aqueous solution were determined at 31, 63, and 125 μg ml^{-1} LM concentrations (**Figure 3.5**). An appreciable absorbance over the NIR region (700–1000 nm) was certainly observed and a linear increase in NIR optical absorbance at 808 nm with increasing concentration of the LM nanocomplexes in aqueous solution, which provides evidence for further exploring its photothermal conversion in the NIR region. Meanwhile, in the synthesized PEG–IMIQ–LM nanoparticle suspension (LM concentration = 125 μg ml^{-1}), absorption was found around 320 and 340 nm, which was confirmed to be the characteristic peaks of encapsulated IMIQ (**Figure 3.6**). All these data demonstrated that LM nanoparticles could tightly encapsulate IMIQ thanks to excellent dispersing property of DSPE–PEG$_{2000}$–NH$_2$, and they could be used as an optically activating nanomedicine.

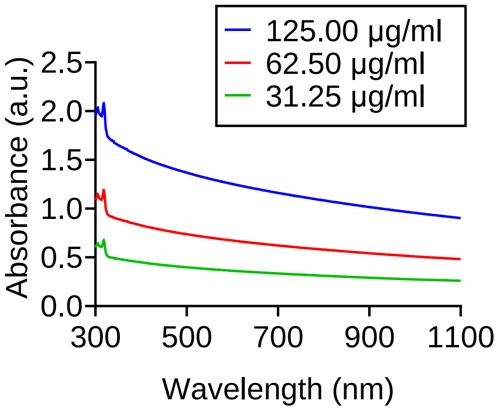

Figure 3.5 UV−vis−NIR absorption spectrum of PEG–IMIQ–LM suspension at different LM concentrations.

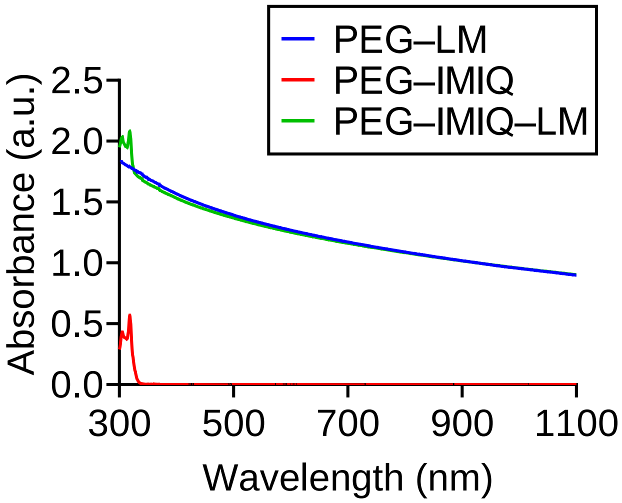

Figure 3.6 UV−vis−NIR absorption spectrum of PEG–LM, PEG–IMIQ, and PEG–IMIQ–LM suspension.

Since PEG–IMIQ–LM nanoparticles have an absorption in the NIR region that increases linearly with LM concentration, we further characterized the thermodynamic properties of PEG–IMIQ–LM nanoparticles. A fiber-coupled 808 nm continuous wave diode laser was used in this study because of high biopermeability, convenient visibility for targeting to objectives, and inexpensive commercial availability. Indeed, aqueous suspensions of the PEG–IMIQ–LM nanoparticle exhibited a significant increase in temperature with increasing LM concentration under NIR-laser irradiation (808 nm) at 1.2 W (~61.1 mW mm^{-2}), whereas control without the PEG–IMIQ–LM nanoparticle displayed a much smaller photothermal conversion effect as a result of absorbance by MilliQ water (**Figure 3.7**). For the 1.0 mg ml^{-1} PEG–IMIQ–LM suspension, the temperature changes (ΔT) reach to 50.3 °C under the 1.2 W laser irradiation for 5 min. In addition, exothermicity of PEG–IMIQ–LM nanoparticle was easily controllable just by changing external laser power. As shown in **Figure 3.7**, when the power of NIR laser decreased to 0.6 W (~30.6 mW mm^{-2}) and 0.3 W (~15.3 mW mm^{-2}), the PEG–IMIQ–LM suspension of the same concentration released less heat (lower ΔT), which reach to 31.9 °C and 15.9 °C, respectively. The above data show that we can control the heat release of LM nanoparticles by adjusting the LM concentration, NIR laser power and irradiation time, thus improving the controllability.

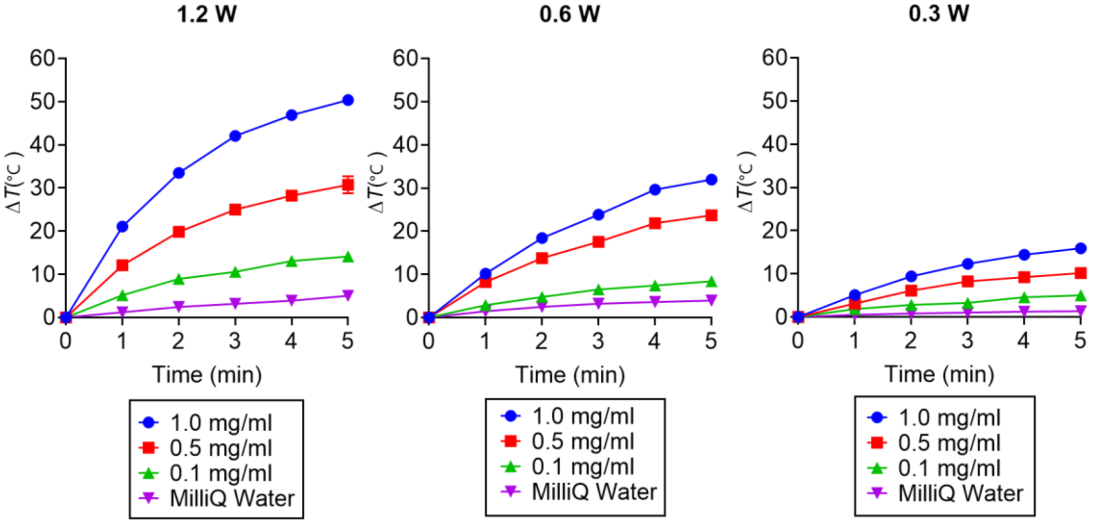

Figure 3.7 Laser-induced temperature increase in MilliQ water (control) and PEG–IMIQ–LM suspension at different concentrations and different powers of NIR laser.

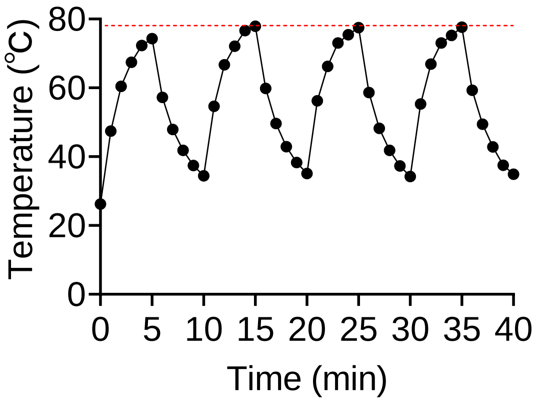

Figure 3.8 Stability testing of the PEG–IMIQ–LM suspension under photothermal heating and natural cooling cycles by 808 nm laser irradiation.

Furthermore, the thermal stability of PEG–IMIQ–LM nanoparticles was investigated. In the laser on/off cycles (four times off and on) at 1.2 W laser power, the temperature changes of PEG–IMIQ–LM nanoparticle suspension showed a negligible fluctuation and an insignificant decline, indicating satisfying photothermal stability of PEG–IMIQ–LM nanoparticle (**Figure 3.8**). In fact, the UV–vis–NIR optical absorption spectra of the PEG–IMIQ–LM nanoparticle was not changed at all except for UV region from 230 to 330 nm because of photo responsive IMIQ releasing before and after laser irradiation for 5 min (**Figure 3.9**). More interestingly, IMIQ molecules can be remotely released from the PEG–IMIQ–LM nanocomplexes by laser irradiation. It was reflected in the increase of absorption in the UV region between 230 to 330 nm after laser irradiation, which is the characteristic region of IMIQ (**Figure 3.10A**). In addition, the releasing of IMIQ was spatiotemporally controllable by laser irradiation time. As shown in **Figure 3.10B**, the release of IMIQ increased with the laser irradiation time, and the maximum release reached 69.16%. We consider that photo-response shape transformation of LMs caused by thermal expansion could contribute on this facilitated drug releasing behaviours.[7, 12]

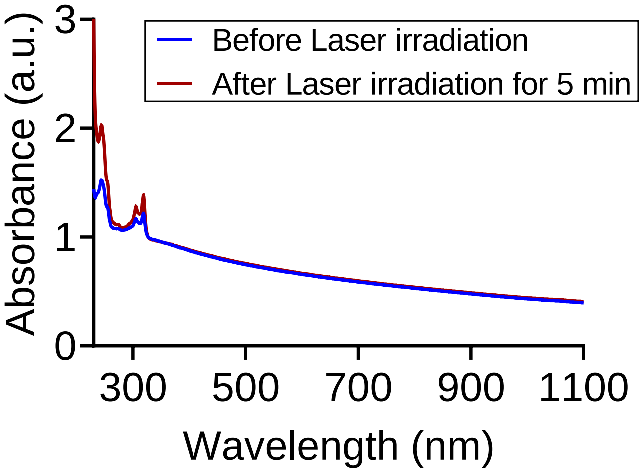

Figure 3.9 UV−vis−NIR absorption spectrum of PEG–IMIQ–LM before and after laser irradiation at 1.2 W power for 5 min.

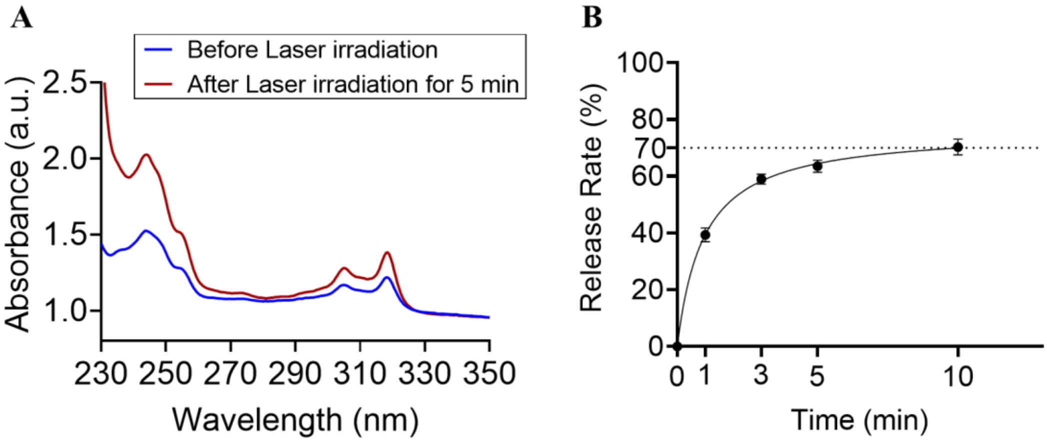

Figure 3.10 Laser-driven control release of IMIQ from the LM nanocomplex. **A)** UV−vis−NIR absorption spectrum (230-350 nm) of PEG–IMIQ–LM before and after laser irradiation at 1.2 W power for 5 min. **B)** Drug release profile from laser-induced PEG–IMIQ–LM.

The photothermal conversion efficiency of the PEG–IMIQ–LM nanoparticle at 808 nm was about 47%. The efficiency of PEG–IMIQ–LM was greater than other light-triggered photo-exothermic nanomaterials such as metal-based materials, carbon dots, and semiconductor polymer nanoparticles (**Tables 3-2 and 3-3**).[7, 10-12, 31-33] These results clearly indicate that the NIR laser-driven PEG–IMIQ–LM nanoparticle act as a powerful and rigid photothermal drug nanocarriers for immunotherapy.

Table 3-2. The photothermal conversion efficiency of materials in previous reports.

Material	Photothermal conversion efficiency (%)	Reference
PEG–IMIQ–LM	47	This study
Gold nanorods	21	31
Gold nanoshells	13	31
Copper selenide	22	31
Carbon dots	31	32
Semiconducting polymer nanoparticles	37	33

Table 3-3. The photothermal conversion efficiency of LM nanoparticles in previous reports.

Material	Photothermal conversion efficiency (%)	Reference
DSPE-PEG2000-amine–DC(8,9)PC–LM	52	7
PEG–IMIQ–LM	47	This study
Melanin–LM	37	12
SH-PEG-HS–CTAB–LM	33	11
Silica–LM	22	10

3.3.2 *In vitro* anticancer efficacy of PEG–IMIQ–LM nanoparticles

Many research groups carefully verify that gallium-based LMs themselves have high biocompatibility.[7-9] To test the cytotoxicity of PEG–IMIQ–LM nanoparticles, we incubated human normal diploid fibroblast (MRC5) and murine colon carcinoma (Colon26) cells with different concentrations of LM nanoparticles for 24 hours. The result was shown in **Figure 3.11**, the synthesized PEG–IMIQ–LM nanoparticle did not also show cytotoxicity at all against MRC5 and Colon26 cells at any concentration. While, radio-immunoprecipitation assay (RIPA) lysis buffer, which was used as a positive control, indicated strong cytotoxicity to both cell lines.

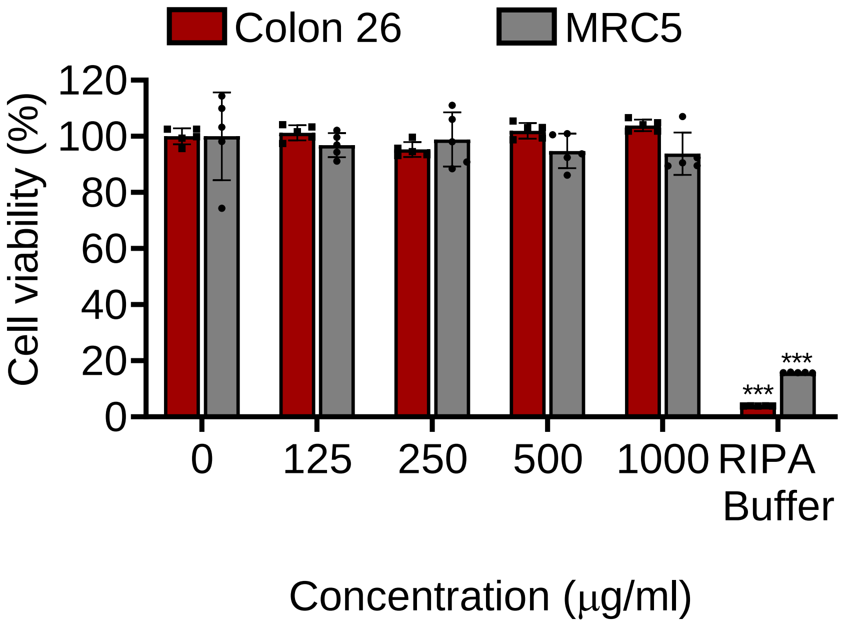

Figure 3.11 Viability of MRC5 and Colon26 cells treated with the RIPA buffer (control) and PEG–IMIQ–LM at various LM concentrations. Data presented as means ± standard error of the mean (SEM) (n = 5; biologically independent tests), ***, $p < 0.001$ versus control without nanoparticles (Student's *t-test*).

More interestingly, Colon26 and MRC5 cells containing PEG–IMIQ–LM were effectively eliminated at 500 or 1000 μg ml^{-1} under an 808 nm NIR laser irradiation at 1.2 W (~61.1 mW/mm^2) thanks to powerful photothermal conversion property of LM. As shown in **Figure 3.12**, high concentrations of PEG–IMIQ–LM have stronger light-induced toxicity, which indicates that the photothermal properties of PEG–IMIQ–LM can still be easily controlled in *in vitro* experiments. At the same time, the laser irradiation group without PEG–IMIQ–LM did not cause toxicity to cells, which showed almost same cell viability with control group, indicating that photothermal therapy using PEG–IMIQ–LM has high precision. Notably, the cytotoxicity of PEG–IMIQ–LM against normal MRC5 cells was less than that against Colon26 cancer cells after laser irradiation because cancer cells are basically heat sensitive because of selective biochemical responses of cancer cells such as heat-shock proteins and unique molecular signalling through heating.[34] In any case, laser-induced PEG–IMIQ–LM indicates selective anticancer efficacy.

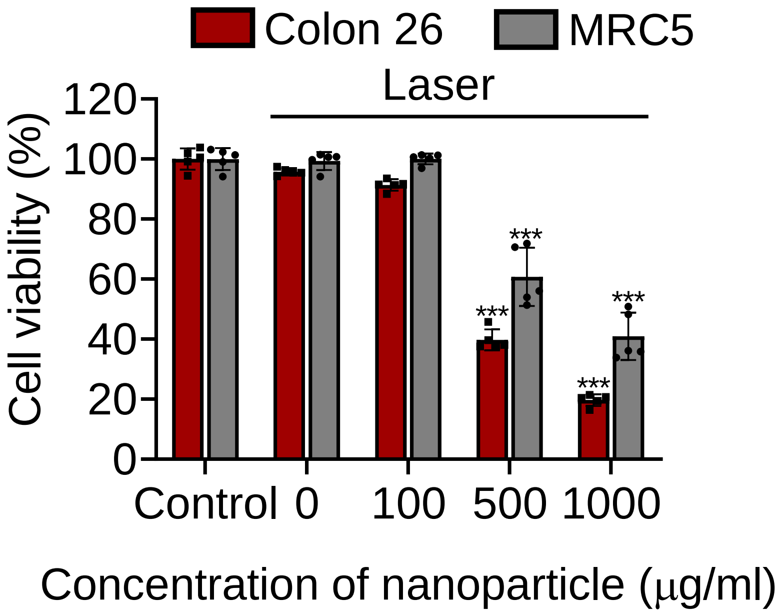

Figure 3.12 Laser-induced PEG–IMIQ–LM cytotoxicity evaluation in MRC5 and Colon26 cells with 5 min laser irradiation at various LM concentrations. Data presented as means ± SEM (n = 5; biologically independent tests), ***, $p < 0.001$, by Student's *t-test*.

Additionally, internalization and distribution of LM nanoparticle in Colon26 cells and spheroids were investigated using fluorescent microscopy. To that end, fluorescent PEG–IMIQ–LM encapsulating indocyanine green (ICG) (PEG–ICG–IMIQ–LM) was prepared using simple sonication process, briefly, 1 mg ICG was mixed with 1 ml prepared PEG–IMIQ–LM solution and stirred up for 1h with dark conditions. (**Figure 3.13**) Hydrophobic ICG molecules can be entrapped with IMIQ in the hydrophobic region formed by long alkyl chains of DSPE–PEG$_{2000}$–NH$_2$ molecules. Fluorescent spectrometer said that the synthesized PEG–ICG–IMIQ–LM (LM concentration = 125 μg ml^{-1}, ICG =

12.5 µg ml^{-1}) had strong NIR fluorescence (FL) emission by various NIR light excitation. (**Figure 3.14**) These excited fluorescent molecules can be observed by fluorescence microscopy to investigate the *in vitro* biological distribution of PEG–ICG–IMIQ–LM.

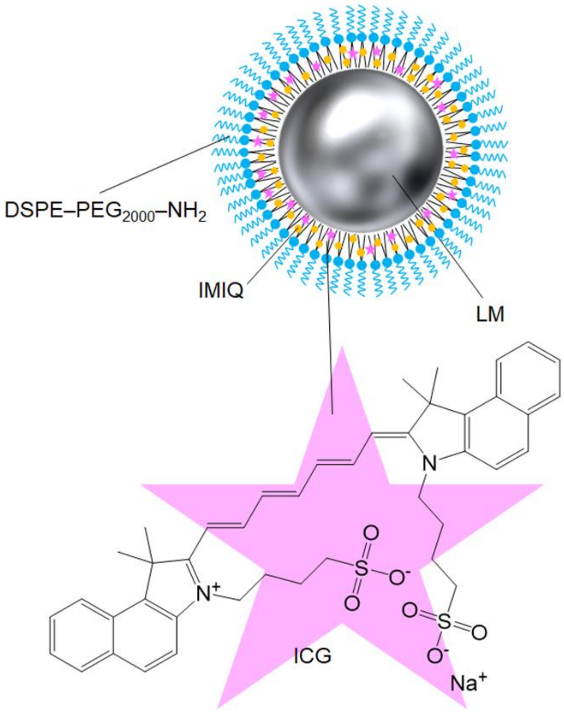

Figure 3 13 Schematic illustration of PEG–ICG–IMIQ–LM nanoparticle.

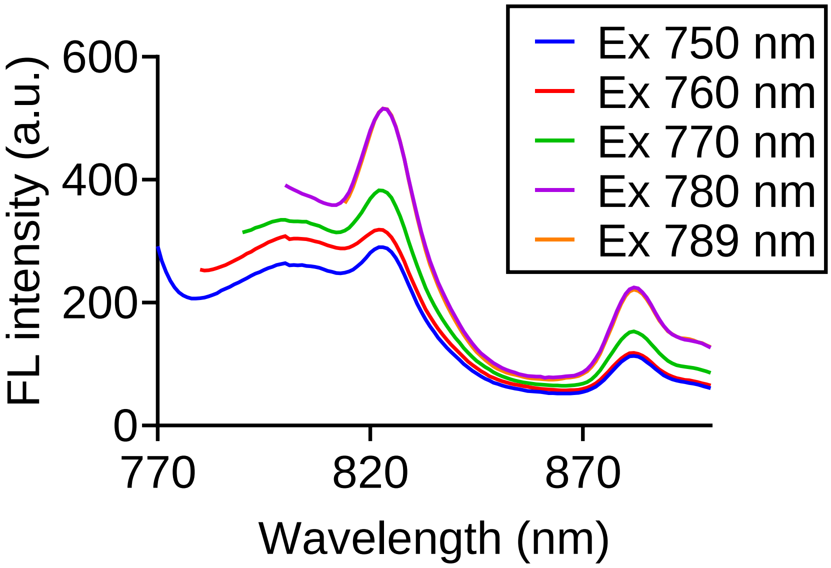

Figure 3.14 FL spectra of PEG–ICG–IMIQ–LM at different excitation wavelength.

The FL microscopy images are shown in **Figure 3.15 and 3.16**, intracellular PEG–ICG–IMIQ–LM uptake (black and/or pink dots) in Colon 26 cells and spheroids model were observed after incubation at 37 °C for 24 h. The black dots are the PEG–ICG–IMIQ–LM nanoconjugates accumulated in cancer cells and spheroids observed under the differential interference contrast (DIC) microscopy, and the pink dots are the released fluorescence signals of nanoconjugates observed by the fluorescence microscopy. This indicates that after cells or spheroids are co-incubated with PEG–ICG–IMIQ–LM, the LM nanoconjugates enter and accumulate inside the cells via endocytosis, providing evidence for further exploration of NIR laser-driven photocytotoxicity. On the other hand, non-treatment cells and spheroids did not show any black or pink dots derived from PEG–ICG–IMIQ–LM nanoconjugates at all.

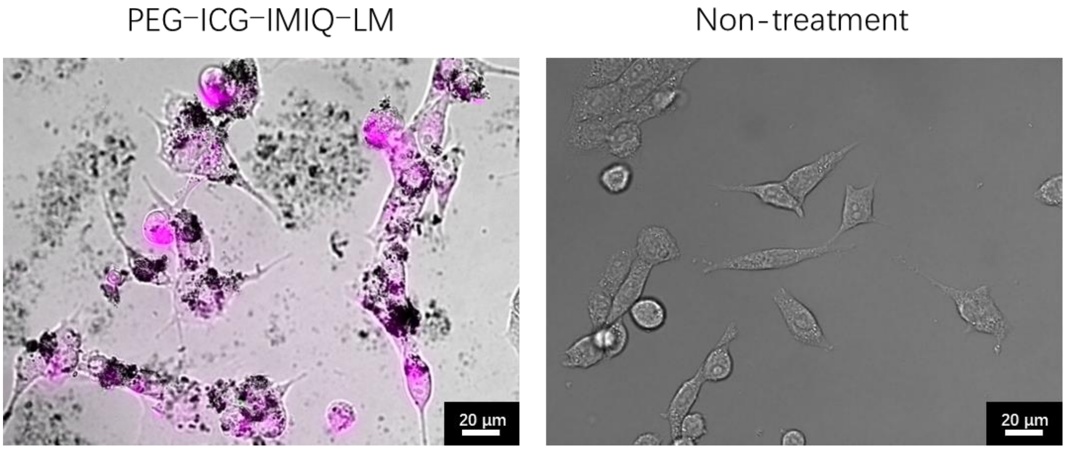

Figure 3.15 *In vitro* biological distribution of PEG–ICG–IMIQ–LM in Colon26 cells (left), and non-treatment as control (right).

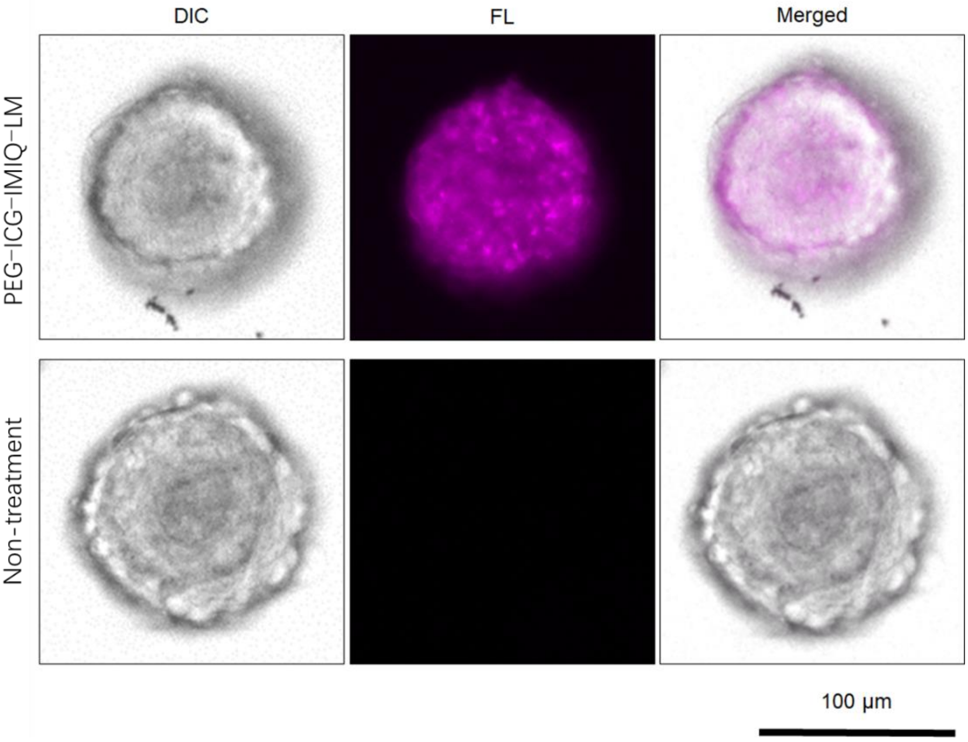

Figure 3.16 *In vitro* fluorescent bioimaging of Colon26 cancer spheroids.

We further investigated the real-time anticancer activity of NIR laser-driven PEG–

IMIQ–LM nanoconjugates by using a beam from a single laser that had been incorporated into the FL microscopy set-up. Surprisingly, the structures of Colon26 cells and spheroids were immediately destructed while forming bubbles presumably after 808nm laser irradiation at 254 mW (~129 mW mm^{-2}) because of water vaporization by strong photo-exothermicity of LM (**Figure 3.17 and 3.18**). In the control experiments performed without the PEG–IMIQ–LM complexes, there were no destruction of cancer cells and spheroids at all. These results clearly indicate that the powerful photothermal conversion of the LM nanoparticles are able to accurately direct the elimination of the targeted cancer cells and spheroids.

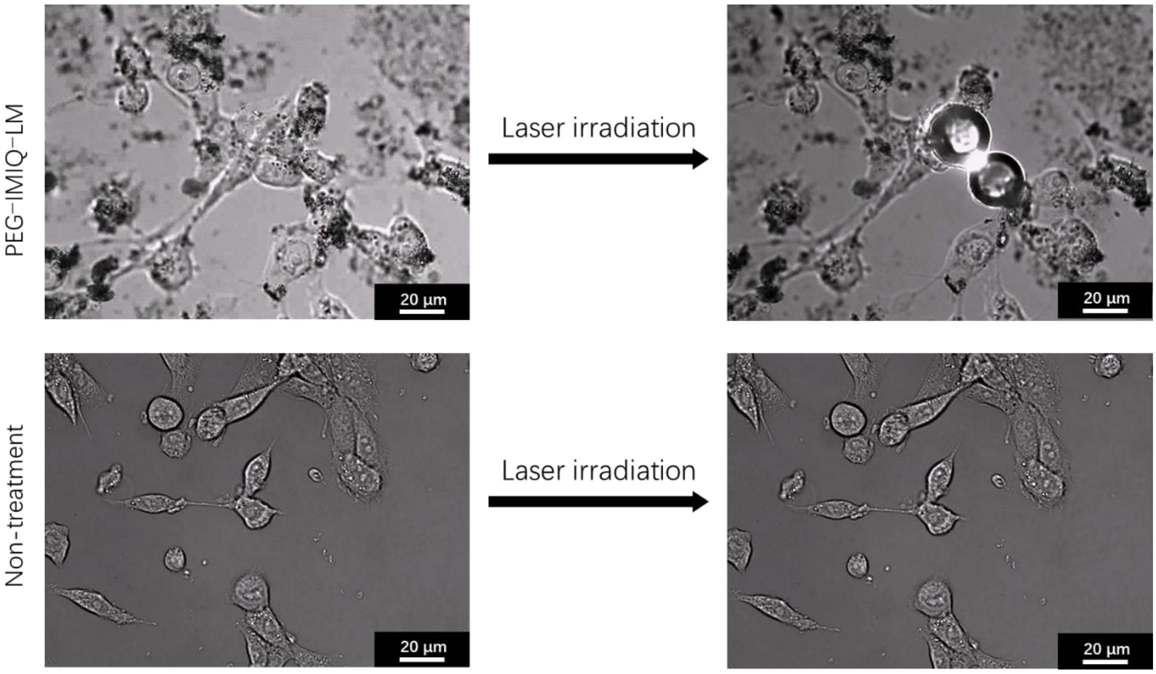

Figure 3.17 Colon26 cells destruction by laser-induced PEG–IMIQ–LM before and after laser irradiation.

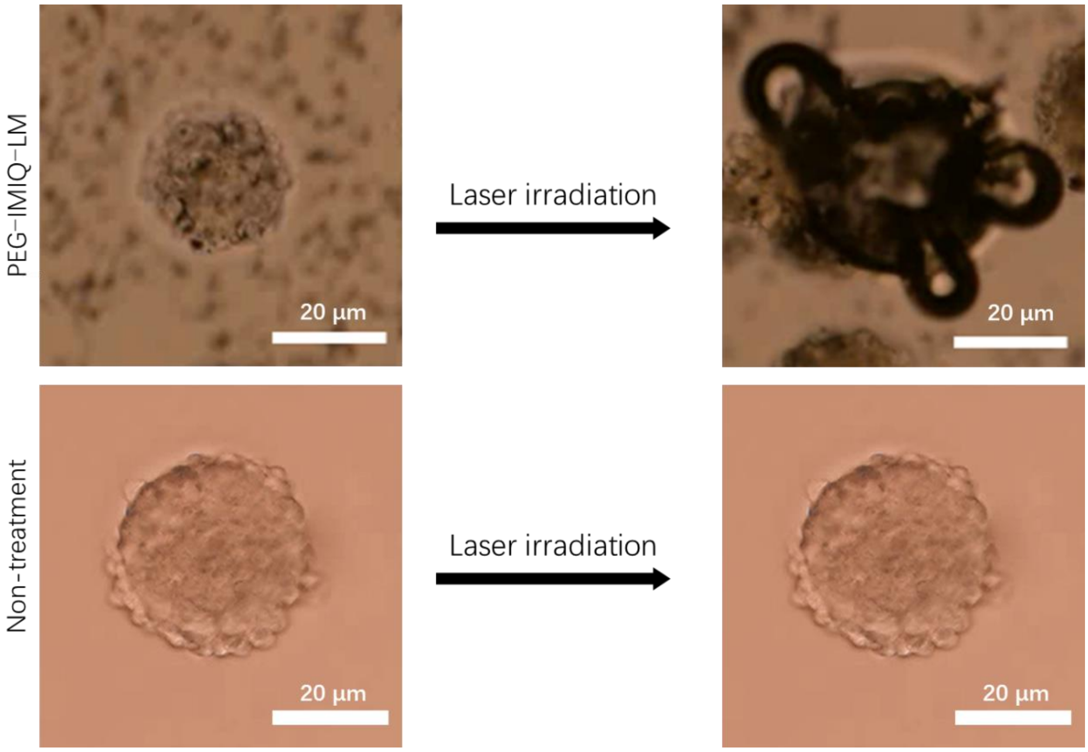

Figure 3.18 Colon26 spheroid destruction by laser-induced PEG–IMIQ–LM before and after laser irradiation.

3.3.3 *In vivo* cancer theranostics

The final goal of the present research is to develop a multifunctional LM immune-nanostimulator for cancer theranostics. To this end, we used the n-hydroxysuccinimide (NHS) group of a commercially-available functional PEG lipid (DSPE–PEG_{2000}–NHS) for the condensation reaction with anti-programmed death ligand-1 antibody (Anti-PD-L1), which is one of the promising immune checkpoint inhibitors (**Figure 3.19**). The binding of PD-L1 to PD-1 inhibits T-cell proliferation and activity, leading to tumor immunosuppression.[35, 36] Thus, Anti-PD-L1 allows blocking of the PD-L1 on cancer cells to evoke anticancer T-cell functions. The Anti-PD-L1 loading concentration was calculated as ~108.5 μg ml^{-1} (reaction yield ~86.8%) to PEG–ICG–IMIQ–LM (LM concertation: 1 mg ml^{-1}) through a bicinchoninic acid assay (BCA assay).

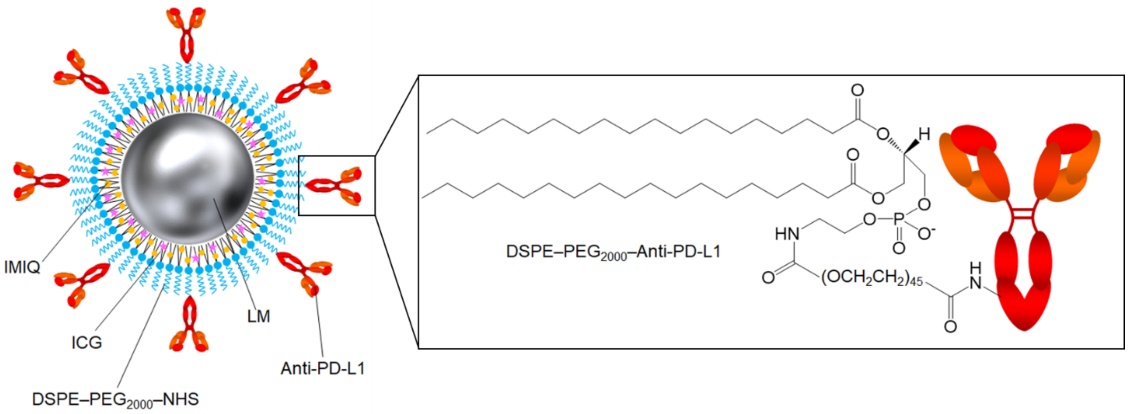

Figure 3.19 Schematic illustration of Anti-PD-L1–PEG–ICG–IMIQ–LM.

Next, the systemic distribution of functional Anti-PD-L1-modified PEG–ICG–IMIQ–LM (Anti-PD-L1–PEG–ICG–IMIQ–LM) nanoparticles was studied to clarify the tumor targeting and anticancer eradication ability of the LM immuno-nanostimulators. As shown in **Figure 3.20**, the prepared Anti-PD-L1–PEG–ICG–IMIQ–LM suspension exhibited sufficient NIR FL by using a bioimager, which PEG–IMIQ–LM showed nothing. The tumor targeting distributions of LM nanoparticles were observed in tumors at 4, 8, 12, and 24 h after intravenous (i.v.) injections of Anti-PD-L1–PEG–ICG–IMIQ–LM through the tail vein of Colon26-bearing mice. As expected, NIR FL was observed in mice after injection of Anti-PD-L1–PEG–ICG–IMIQ–LM and accumulated at the tumor site over time because of the EPR effects (**Figure 3.21A**).[23] The control group which injected NS did not display any FL intensity in the whole body of Colon26-bearing mouse.

In addition, the mice were dissected 24 hours after injection, and the NIR FL intensity of major organs including heart, liver, spleen, lung, kidney and tumor tissues were observed by using a bioimager (**Figure 3.21B**). A minor amount of fluorescence in the kidneys suggests that the major elimination pathway for LM nanocomplexes is renal excretion thanks to the enhanced long-term blood circulation of nanomedicines because of its typical excellent water dispersibility and immune evasion properties by PEGylation.[37, 38] These results definitely indicate that the prepared Anti-PD-L1–PEG–ICG–IMIQ–LM should have high tumor selectivity through a single administration.

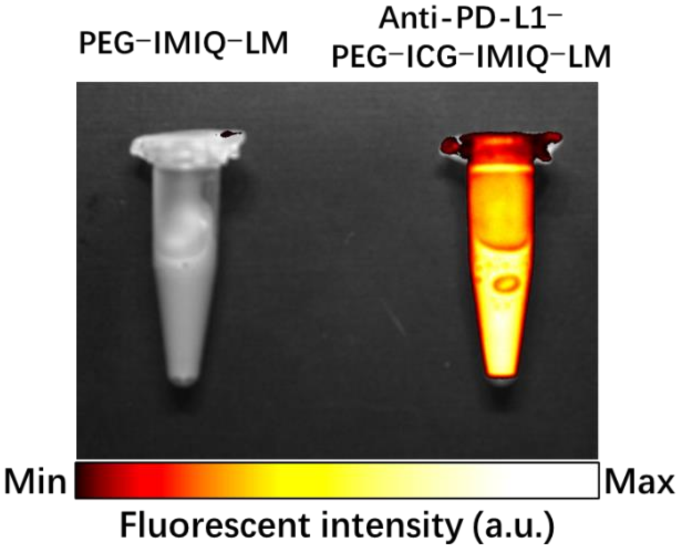

Figure 3.20 FL images of PEG–IMIQ–LM (left) and anti-PD-L1–PEG–ICG–IMIQ–LM (right) suspensions.

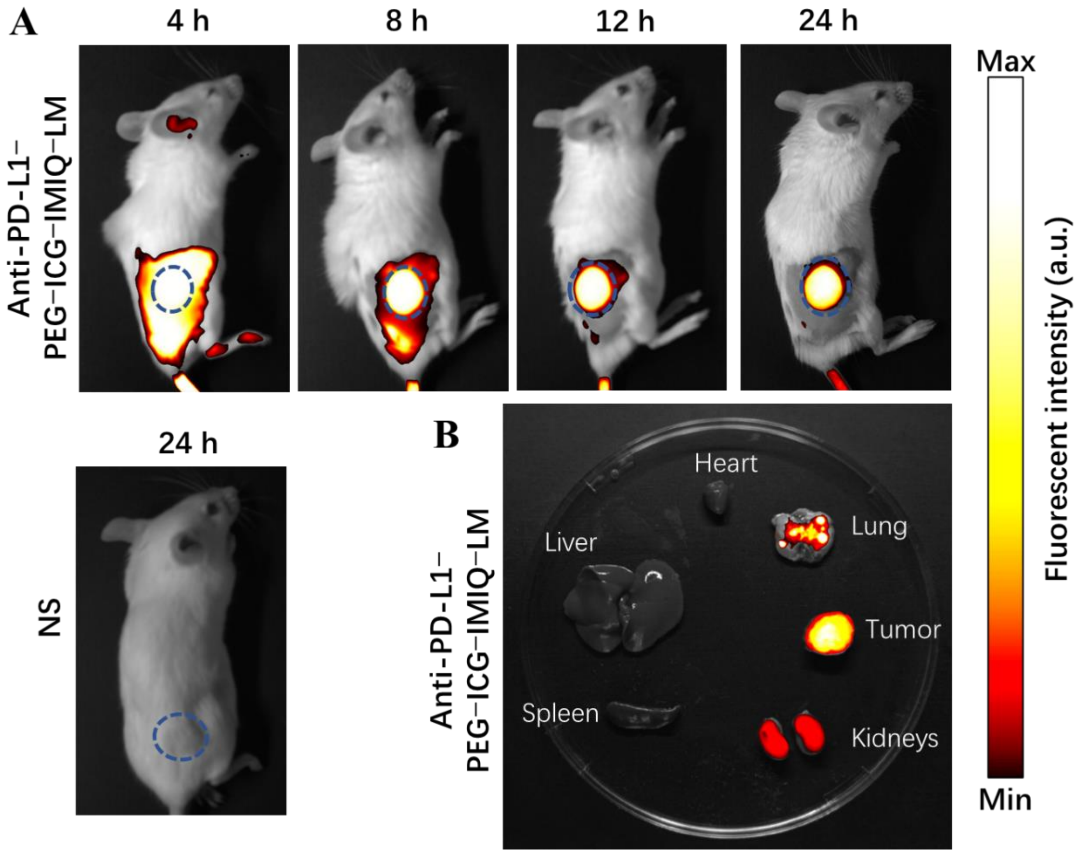

Figure 3.21 FL imaging of **A)** Colon26 tumor-bearing mice and **B)** extracted vital organs and tumor tissue after an i.v. injection. Blue dashed circles denote the solid tumor location.

We then investigated the *in vivo* photothermal conversion capability of Anti-PD-L1–PEG–IMIQ–LM nanoconjugates (and other samples as control) at tumor sites. The targeted Colon26 tumor of a mouse was irradiated using an 808 nm laser at 0.6 W (~30.6 mW mm^{-2}) after 24 h of single i.v. administration of each sample. We then continuously monitored the body surface temperature by using a thermographic camera during irradiation (**Figure 3.22**). Among them, the tumor surface temperatures of mice injected with Anti-PD-L1-functionalized PEG–IMIQ–LM (Anti-PD-L1–PEG–IMIQ–LM) significantly increased after 5 min of NIR irradiation, reaching a maximum value at approximately 55 °C (**Figure 3.23**). Although DSPE–PEG$_{2000}$–NH$_2$-modified LM (PEG–LM) also showed marked temperature increases, laser-induced Anti-PD-L1–IMIQ–LM demonstrated higher tumor surface temperature than laser-induced PEG–LM, indicating that Anti-PD-L1–PEG–IMIQ–LM accumulated in solid tumors and effectively heated the deeper internal tumor tissue due to the EPR effect, binding of Anti-PD-L1–PEG–IMIQ–LM onto PD-L1 of the Colon26 tumor cells, and phagocytosis by myeloid cells, such as macrophage and DC, owing to the immunological activation by IMIQ molecules. Contrarily, the control groups including NS, DSPE–PEG$_{2000}$–NH$_2$-modified IMIQ (PEG–IMIQ), and Anti-PD-L1-injected mice, displayed slight surface temperature increases after laser irradiation, probably because the skin, blood, and tissue converted light energy to heat.

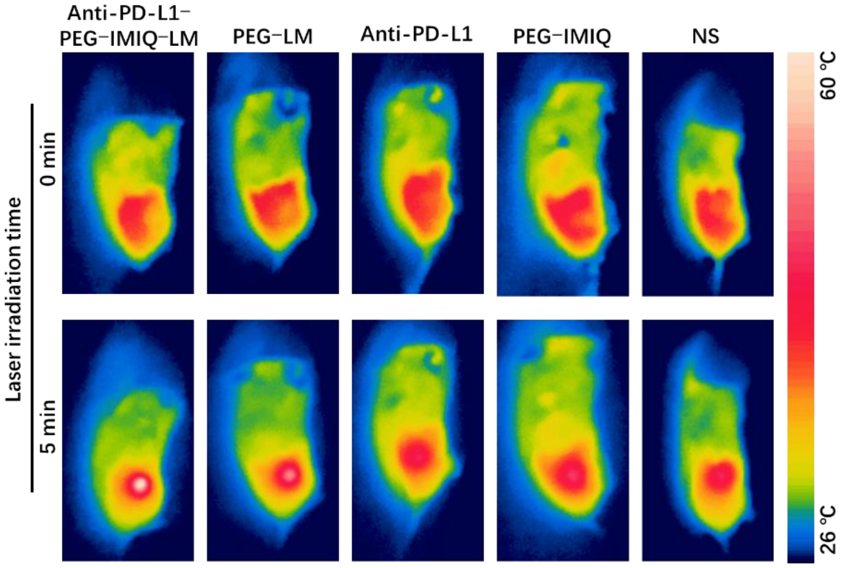

Figure 3.22 Thermographic measurement of the tumor on the mouse body surface for treatment with laser irradiation.

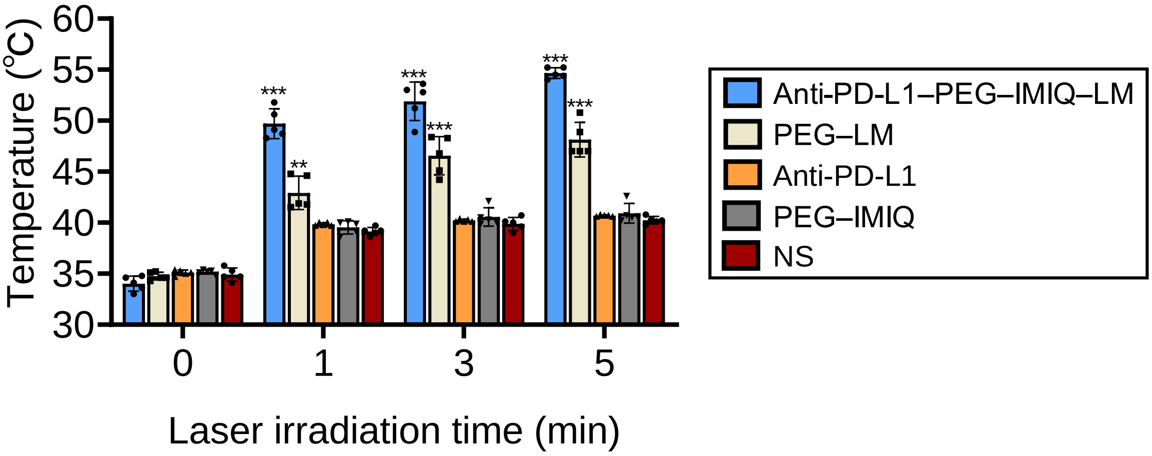

Figure 3.23 Solid tumor surface temperature of Colon26-bearing mice after injection followed by 808 nm laser irradiation for 5 min. Data are expressed as means ± standard error of the mean (SEM); n = 5 independent experiments. Statistical significance was calculated in comparison with the NS group. **, $p < 0.01$, and ***, $p < 0.001$, by Student's *t-test*.

Laser-induced Anti-PD-L1–PEG–IMIQ–LM exhibited the highest anticancer efficacy compared with the other control groups (**Figure 3.24**). In fact, the irradiated solid tumors totally disappeared after laser irradiation for just six times with Anti-PD-L1–PEG–IMIQ–LM owing to the powerful photothermal property of LM, excellent tumor targeting effect, effective controlled drug-releasing of IMIQ, and multidimensional immunological stimulations; 100% complete response (CR) was confirmed in the case at the 22-day follow-up. Due to the excellent photothermal conversion ability of LM nanoparticles, the heat generated by laser irradiation would burn part of the surface skin, however, the scab was observed to fall off on the 29-day and the skin healed. Notably, the group receiving treatment with Anti-PD-L1–PEG–IMIQ–LM and laser irradiation considerably achieved faster healing of tumors and injured parts than other control groups (**Figure 3.25**). Although the LM + laser group indicated CR of the tumor because of the potent photothermal conversion, tumor reoccurrence was unfortunately observed. The Anti-PD-L1 + laser group showed somewhat stronger antitumor effectiveness than the NS + laser group probably because of PD-L1 blocking. The PEG–IMIQ + laser group also displayed better efficacy than the NS + laser group owing to DC activation. These results potentially indicate that laser induction might help in immunological activation by heat energy from the natural photothermal conversion of biological tissue.

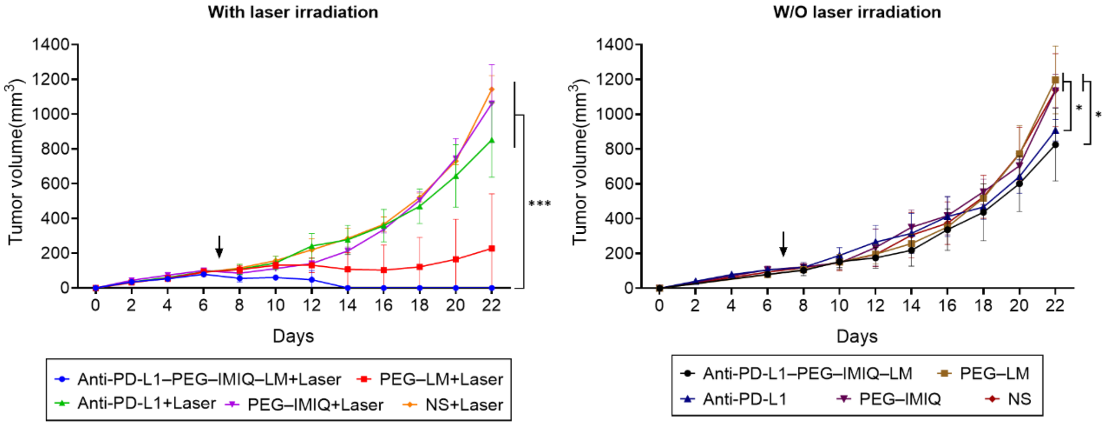

Figure 3 24 *In vivo* anticancer effect of various samples with and without laser irradiation. Irradiation time = 5 min every day (total six times irradiation). Data are expressed as means ± standard error of the mean (SEM) (n = 5 biologically independent tests). *, $p < 0.05$, and ***, $p < 0.001$, by Student's *t-test*. The black arrows display the time point of sample administration.

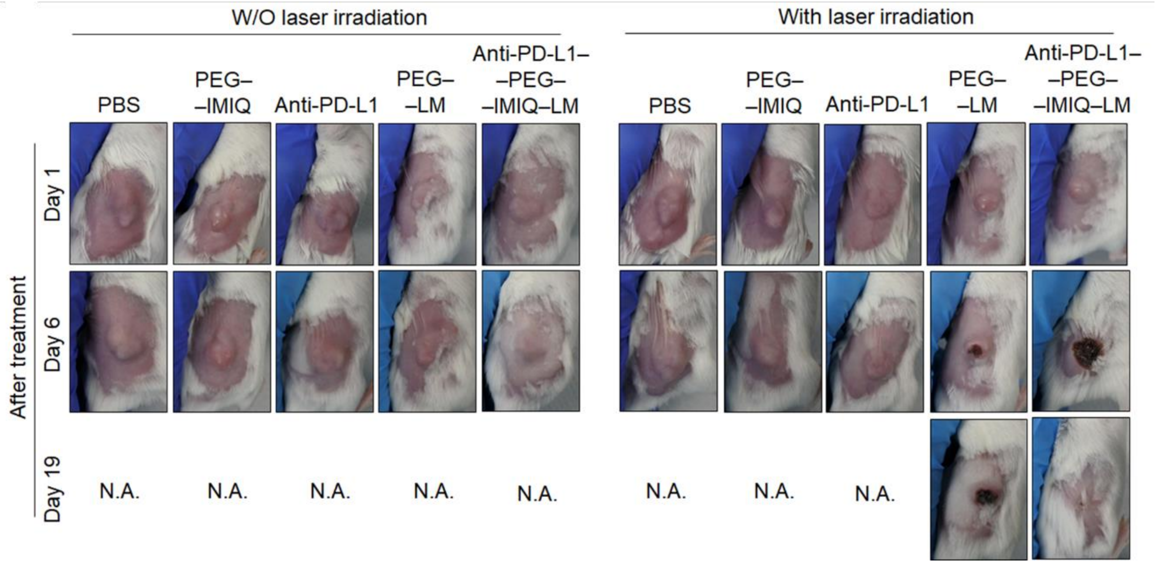

Figure 3.25 Images of mice after each treatment.

Furthermore, the laser-induced Anti-PD-L1–PEG–IMIQ–LM nanostimulator-treated mice exhibit not only excellent anticancer responses but also significant prolonged survival rates (**Figure 3.26**). Contrarily, the control groups without laser irradiation, especially Anti-PD-L1–PEG–IMIQ–LM and Anti-PD-L1, have somewhat anticancer effectiveness even by single administration due to the excellent anticancer efficacy of Anti-PD-L1 itself and the targeted delivery of IMIQ into the tumor by EPR effect. NS, PEG–LM, and PEG–IMIQ alone did not show therapeutic performances at all The body weight of all treatment groups was relatively constant during the experimental period, indicating no side effects (**Figure 3.27**).

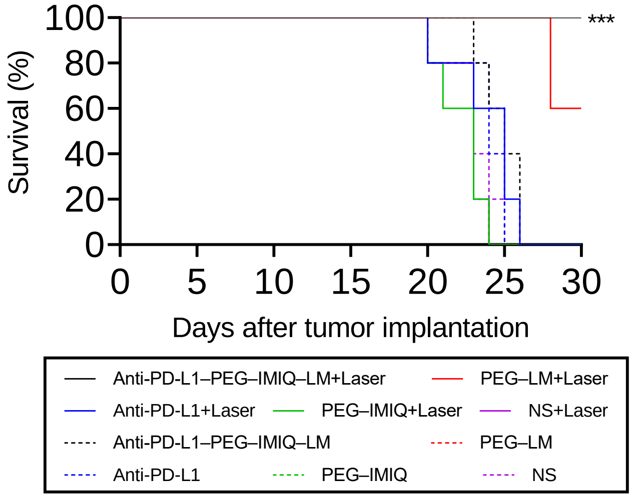

Figure 3.26 Kaplan–Meier survival curves of Colon26-tumor-bearing mice (n = 5 biologically independent mice) after tumor implantation for 30 days. Statistical significance was calculated in comparison with the NS group. ***, $p < 0.001$ by Log-rank (Mantel–Cox) test.

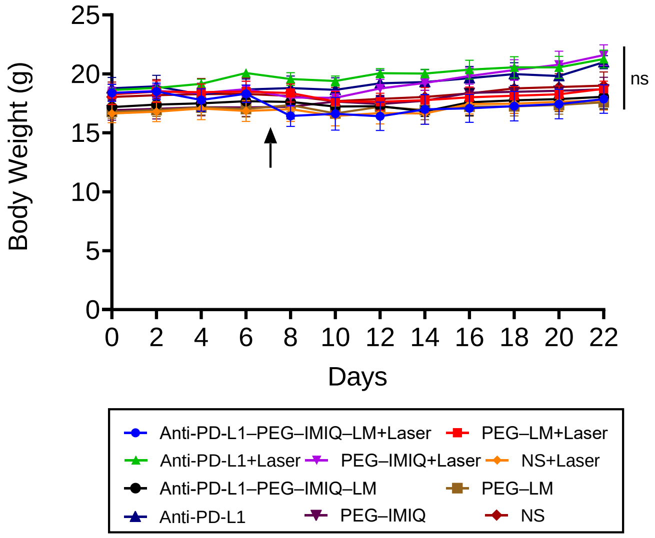

Figure 3.27 Average mouse body weight after treatments during the treatment period. The black arrow displays the time point of the sample administration. Data are expressed as means ± standard error of the mean (SEM) (n = 5 biologically independent tests). ns, not significant, by Student's *t-test*.

Furthermore, blood tests said that Anti-PD-L1–PEG–IMIQ–LM did not show any *in vivo* toxicity (**Table 3-4**). There was no statistically significant difference in the complete blood count or biochemical parameters of mice after intravenously injection with NS or Anti-PD-L1–PEG–IMIQ–LM suspension after 30 days. These results clearly indicate that laser-induced Anti-PD-L1–PEG–IMIQ–LM was effective and safe as a multidimensional anticancer agent, and both photothermal conversion and immunological stimulation could exert synergetic antitumor therapeutic effects for cancer treatment.

Table 3-4 CBCs and biochemical parameters of the mice injected with NS or Anti-PD-L1–PEG–IMIQ–LM nanoparticle dispersion after 30 days.

Measured value	Entry	Unit	NS (n = 7)	Anti-PD-L1–PEG–IMIQ–LM (n = 7)	P value
CBC	WBC	×10^2/μL	64.0 ± 7.03	61.9 ± 7.57	> 0.05
	RBC	×10^4/μL	936.1 ± 8.79	923.1 ± 21.20	> 0.05
	HGB	g/dL	14.3 ± 0.31	14.2 ± 0.32	> 0.05
	HCT	%	42.8 ± 0.78	42.6 ± 1.09	> 0.05
	MCV	fL	45.7 ± 0.51	45.9 ± 0.39	> 0.05
	MCH	pg	15.3 ± 0.27	15.3 ± 0.14	> 0.05
	MCHC	g/dL	33.5 ± 0.32	33.4 ± 0.38	> 0.05
	PLT	×10^4/μL	77.2 ± 6.21	75.1 ± 3.64	> 0.05
Biochemical parameters	TP	g/dL	4.0 ± 0.14	4.2 ± 0.12	> 0.05
	ALB	g/dL	2.7 ± 0.14	2.8 ± 0.08	> 0.05
	BUN	mg/dL	18.5 ± 1.42	19.3 ± 0.71	> 0.05
	CRE	mg/dL	0.1 ± 0.02	0.1 ± 0.01	> 0.05
	Na	mEq/L	145.6 ± 1.72	147.3 ± 1.11	> 0.05
	K	mEq/L	3.5 ± 0.25	3.4 ± 0.20	> 0.05
	Cl	mEq/L	114.0 ± 3.92	118.4 ± 1.90	> 0.05
	AST	IU/L	71.9 ± 28.07	65.1 ± 13.22	> 0.05
	ALT	IU/L	34.6 ± 11.98	30.9 ± 5.58	> 0.05
	LDH	IU/L	227.9 ± 20.68	241.1 ± 31.54	> 0.05
	AMY	IU/L	1701.6 ±191.77	1656.6 ± 99.17	> 0.05
	CK	IU/L	140.3 ± 38.06	134.6 ± 48.66	> 0.05

Data are represented as means ± standard errors of the mean (SEM.); n = 7 biologically independent mice. Statistical analyses comprise the Student's two-sided *t test*.

Abbreviations: ALB, albumin; ALT, alanine transaminase; AMY, amylase; AST, aspartate aminotransferase; BUN, blood urea nitrogen; Cl, chlorine; CK, creatine kinase; CRE, creatinine; HCT, hematocrit; HGB, hemoglobin; K, potassium; LDH, lactate dehydrogenase; MCH, mean corpuscular hemoglobin; MCHC, mean corpuscular hemoglobin concentration; MCV, mean corpuscular volume; Na, sodium; PLT, platelet; RBC, red blood cell; TP, total protein; WBC, white blood cell.

3.3.4 The mechanism of tumor suppression by LM nanostimulant

To explore the immunological mechanism related to solid tumor regression by light-triggered LM immune-nanostimulant, hematoxylin and eosin (H&E) and immunohistochemical (IHC) staining analyses were performed (**Figure 3.28A**). Image-guided statistical IHC analysis using computer-aided software was also applied in this study because it is a highly useful and reliable technique for detection and quantification of target epitopes (e.g., proteins, structures, cellular components, etc.) in a wide variety tissue types (**Figure 3.28B**).[39, 40] Among them, the anti-PD-L1–PEG–IMIQ–LM + laser group demonstrated obvious structural destruction of solid tumor with intercellular fragmentation by H&E staining assay, indicating a strong antitumor efficacy. Meanwhile, the PEG–LM + laser showed slight tumor degradation, and the anticancer therapeutic efficacy was lower than that observed in the Anti-PD-L1–PEG–IMIQ–LM + laser group. Contrarily, H&E staining of tumor tissues showed no discernible lesions throughout the treatment process in the Anti-PD–L1 + laser, PEG–IMIQ + laser, and NS + laser groups. Terminal deoxynucleotidyl transferase (TdT)-mediated 2′-deoxyuridine, 5′-triphosphate (dUTP) nick end labeling (TUNEL) assay also confirmed the results of H&E staining, revealing many apoptotic cells, especially in the anti-PD-L1–PEG–IMIQ–LM + laser group. Simultaneously, the Cleaved Caspase-3 staining assay used also further confirmed the strong *in vivo* anticancer mechanism of the laser-induced Anti-PD-L1–PEG–IMIQ–LM.

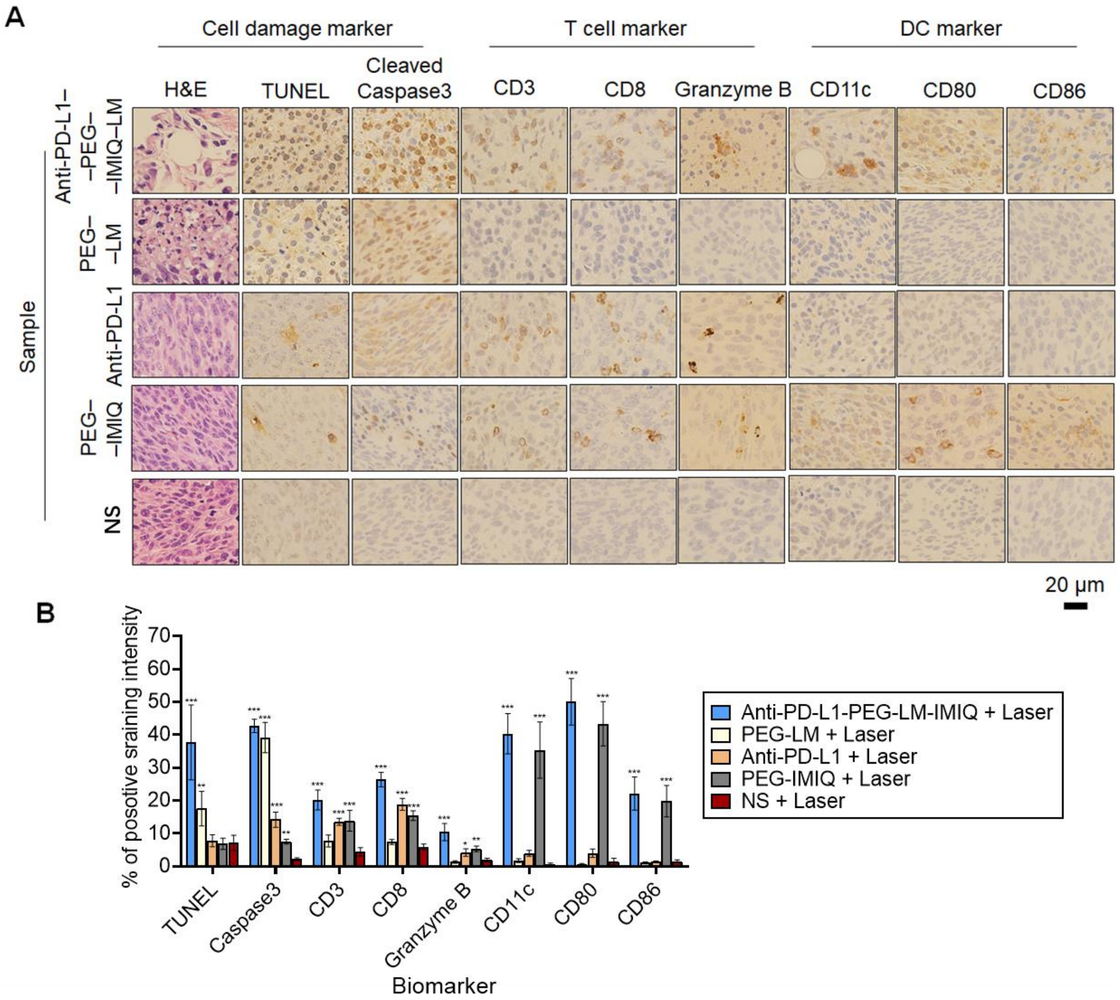

Figure 3.28 Mechanism of tumor suppression by laser-driven Anti-PD-L1–PEG–IMIQ–LM. **A)** H&E, TUNEL, and IHC stained tumor tissues collected from different groups of mice at day 1 after their respective treatments. **B)** Statistical analyses of IHC and TUNEL-positive stained tumor tissues in Figure 3.28A. Data are represented as mean ± standard error of the mean (SEM); n = 10 independent areas (region of interest) in each tumor tissue collected from the groups of mice on day 1 after treatments. Statistical significance was calculated in comparison with the NS group. *, $p < 0.05$, **, $p < 0.01$, and ***, $p < 0.001$ by Student's *t-test*.

IHC staining of CD3 (T-cell marker), CD8 (T-cell marker), Granzyme B (T-cell marker), CD11c (DC marker), CD80 (DC marker), and CD86 (DC marker) could also recognize the immunological reactions for the modulation of tumor regression by laser-induced Anti-PD-L1–PEG–IMIQ–LM. Laser-induced Anti-PD-L1–PEG–IMIQ–LM exhibited the expression of all immunological biomarkers probably because Anti-PD-L1 and IMIQ molecules could work as stimulants for T-cell and DC, respectively. In fact, the anti-PD-L1 + laser group significantly stimulated the T-cell markers. Contrarily, the PEG–IMIQ + laser group certainly modulates the DC markers. The other control approaches of PEG–LM + laser and NS + laser were ineffective for immunological stimulation, as compared with Anti-PD-L1–PEG–IMIQ–LM + laser, Anti-PD-L1 + laser, and PEG–IMIQ + laser. Particularly, the NS + laser treatment did not affect the expression of immunological biomarkers at all. Moreover, significant color developments of DC-derived immunostimulatory factors, including TNF-α and IL-6, in the Anti-PD-L1–PEG–IMIQ–LM + laser and IMIQ + laser groups were also observed (**Figure 3.29A and B**). We further performed flow cytometry analysis to confirm the immune effect stimulated by Anti-PD-L1–PEG–IMIQ–LM. Flow cytometry also said that Anti-PD-L1–PEG–IMIQ–LM especially showed effective activation of T cell and DC in spleen, which is a central repository for immune cells and makes diverse contributions to systemic immune responses against cancerous tumors (**Figure 3.30**).

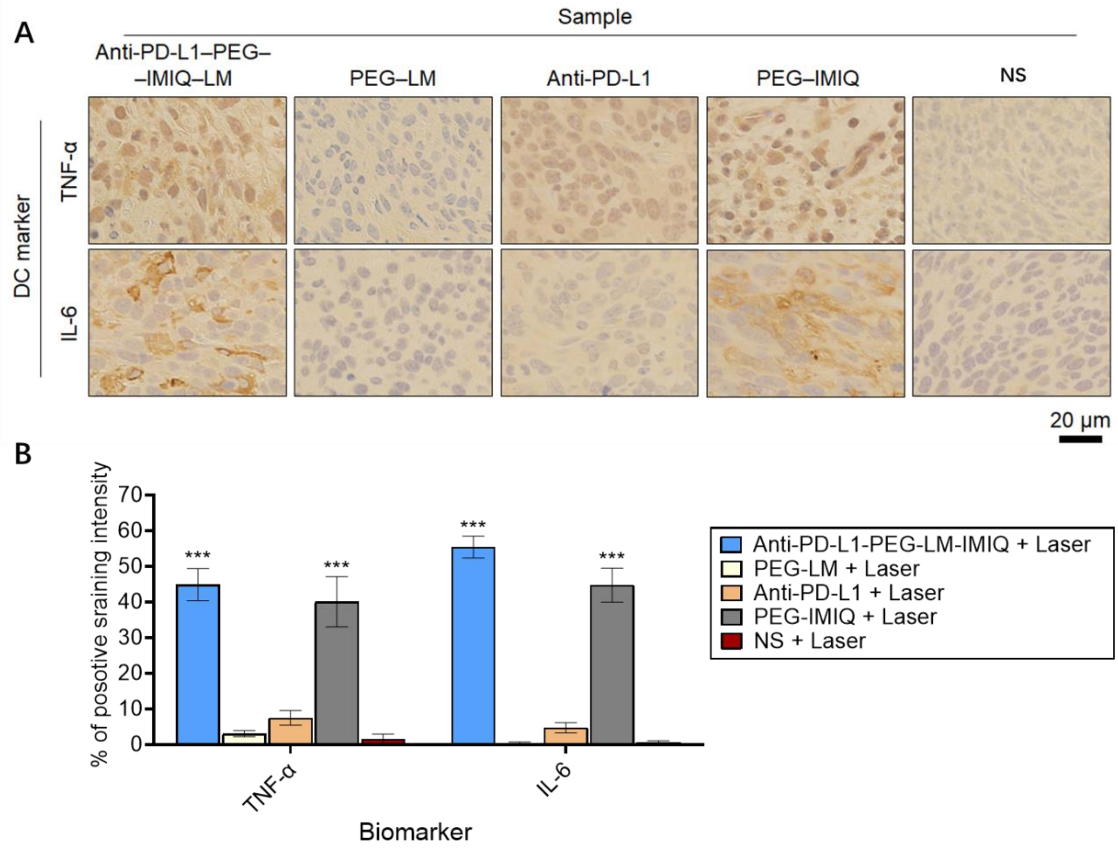

Figure 3.29 A) TNF-α and IL-6-stained tumor tissues were collected from different groups of mice on day 1 after the respective treatments. **B)** Statistical analyses of TNF-α and IL-6-positive stained tumor tissues in Figure 3.29A. Data are represented as mean ± standard error of the mean (SEM); n = 10 independent areas (region of interest) in each tumor tissue collected from the groups of mice on day 1 after treatments. Statistical significance was calculated in comparison with the NS group. ***, $p < 0.001$ by Student's *t-test*.

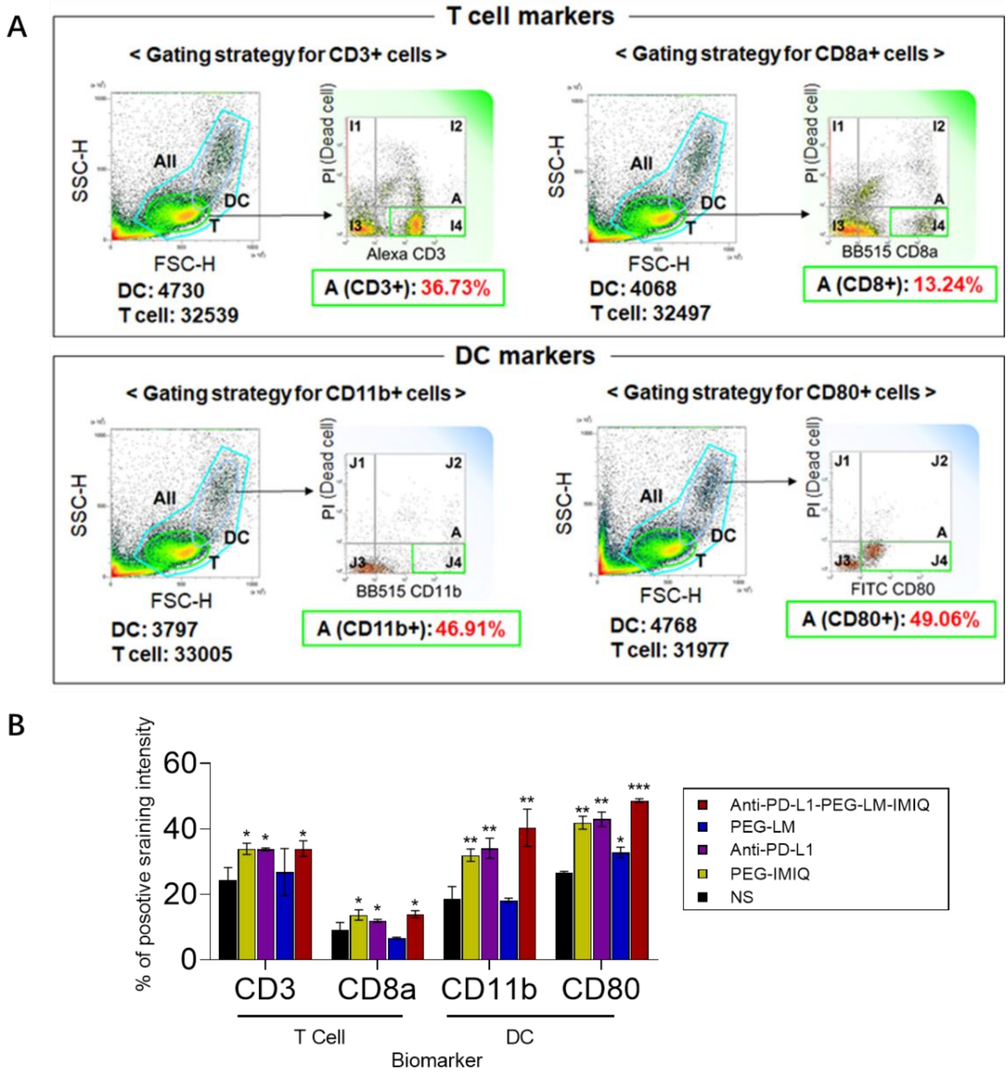

Figure 3.30 Flow cytometry analyses of expression of CD3, CD8a, CD11b, and CD80 in spleens after i.v. injection of each sample for 3 h. **A)** Representative gating strategy for flow cytometry experiments assessing T cell (CD3 and CD8a) and DC (CD11b and CD80) populations after treatment with Anti-PD-L1–PEG–IMIQ–LM. The lymphocytes or the population of monocytes and granulocytes were gated by SSC-H vs. FSC-H, and then plotted in a new graph to calculate the percentages of the CD3, CD8a, CD11b, and CD80 positive cells in the selected total cells. Dead cells were excluded by selecting all live

cells from the plots with PI staining. **B)** Statistical analyses of immunological biomarkers relevant to T cell and DC activations. Data are represented as mean ± SEM; n = 3 independent spleen tissues. Statistical significance was calculated in comparison with the NS group. *, $p < 0.05$, **, $p < 0.01$, and ***, $p < 0.001$, by one-side Student's *t-test*.

In sum, we consider that laser-induced Anti-PD-L1–PEG–IMIQ–LM represents obvious tumor regression and fast healing of injury due to synergistic T-cell and DC stimulations and photothermal destruction of cancerous tumors by effective inhibition of PD-L1 on cancer cells, DC activation by IMIQ, and powerful photothermal conversion and light-driven drug-releasing properties of Anti-PD-L1–PEG–IMIQ–LM **(Figure 3.31)**. We believe that these synergistic immunological effects and optical nano functions of LMs have wide therapeutic application prospects.

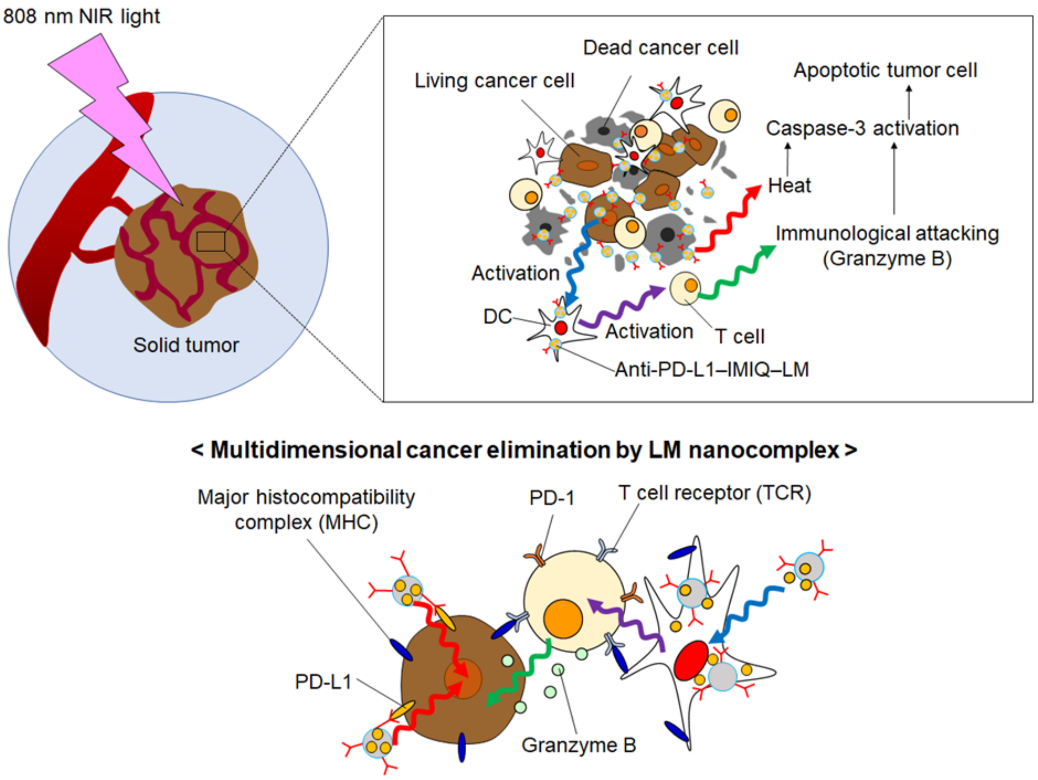

Figure 3.31 The scheme of the proposed mechanism.

3.4 Conclusion

In this study, we synthesized the multifunctional LM nanocomplexes, which are highly water-dispersible with high biocompatibility, by simple pulse-type sonication. Moreover, the NIR laser-triggered LM nanocomplex can be used to effectively eliminate cancer cells and spheroids due to its powerful photothermal properties. For immunological modulations, further functionalization of the LM nanocomplex with an immune checkpoint inhibitor (Anti-PD-L1) and DC activator (IMIQ) was also developed by sonication and one-step chemical reaction. The light-induced functional immunogenic LM nanocomplex can effectively eradicate colorectal tumors in living mice due to the synergistic anticancer performances of immunomodulators, powerful photo-exothermicity of LM, unique remote drug-releasing effect, and excellent tumor targeting effect. Furthermore, nanocomplexes remotely produced the fluorescent emission in cells, spheroids, and living mice when irradiated with NIR light. This study is the first to exploit the various physicochemical properties of LM nanocomplexes for cancer immunotheranostics. We believe that the design strategy and concept of the current LM nanocomplexes are useful and expandable for improving the biomedical theranostic effects of LM not only for cancer treatment but also for various disease treatment and care.

3.5 Reference

1. Liu, J.; Yi, L., *Liquid Metal Biomaterials: Principles and Applications*. Springer Nature Singapore: 2019.
2. Daeneke, T.; Khoshmanesh, K.; Mahmood, N.; de Castro, I. A.; Esrafilzadeh, D.; Barrow, S. J.; Dickey, M. D.; Kalantar-zadeh, K., Liquid metals: fundamentals and applications in chemistry. *Chemical Society Reviews* **2018,** *47* (11), 4073-4111.
3. Zhang, M.; Yao, S.; Rao, W.; Liu, J., Transformable soft liquid metal micro/nanomaterials. *Materials Science and Engineering: R: Reports* **2019,** *138*, 1-35.
4. Yu, Y.; Miyako, E., Recent Advances in Liquid Metal Manipulation toward Soft Robotics and Biotechnologies. *Chemistry* **2018,** *24* (38), 9456-9462.
5. Miyako, E., Convergence of Liquid Metal Biotechnologies for Our Health. *Accounts of Materials Research* **2021,** *2* (10), 858-862.
6. Xie, W.; Allioux, F. M.; Ou, J. Z.; Miyako, E.; Tang, S. Y.; Kalantar-Zadeh, K., Gallium-Based Liquid Metal Particles for Therapeutics. *Trends Biotechnol* **2021,** *39* (6), 624-640.
7. Chechetka, S. A.; Yu, Y.; Zhen, X.; Pramanik, M.; Pu, K.; Miyako, E., Light-driven liquid metal nanotransformers for biomedical theranostics. *Nat Commun* **2017,** *8*, 15432.
8. Yun, Q.; Kimura, A.; Taguchi, M.; Miyako, E., Sonication - and γ-ray-mediated biomolecule-liquid metal nanoparticlization in cancer optotheranostics. *Applied Materials Today* **2022,** *26*, 101302.
9. Yu, Y.; Miyako, E., Alternating-Magnetic-Field-Mediated Wireless Manipulations of a Liquid Metal for Therapeutic Bioengineering. *iScience* **2018,** *3*, 134-148.
10. Lu, Y.; Lin, Y.; Chen, Z.; Hu, Q.; Liu, Y.; Yu, S.; Gao, W.; Dickey, M. D.; Gu, Z., Enhanced Endosomal Escape by Light-Fueled Liquid-Metal Transformer. *Nano Lett* **2017,** *17* (4), 2138-2145.
11. Yan, J.; Zhang, X.; Liu, Y.; Ye, Y.; Yu, J.; Chen, Q.; Wang, J.; Zhang, Y.; Hu, Q.; Kang, Y.; Yang, M.; Gu, Z., Shape-controlled synthesis of liquid metal nanodroplets for photothermal therapy. *Nano Research* **2019,** *12* (6), 1313-1320.
12. Sun, X.; Sun, M.; Liu, M.; Yuan, B.; Gao, W.; Rao, W.; Liu, J., Shape tunable gallium nanorods mediated tumor enhanced ablation through near-infrared photothermal therapy. *Nanoscale* **2019,** *11* (6), 2655-2667.
13. Zhu, P.; Gao, S.; Lin, H.; Lu, X.; Yang, B.; Zhang, L.; Chen, Y.; Shi, J., Inorganic Nanoshell-Stabilized Liquid Metal for Targeted Photonanomedicine in NIR-II Biowindow. *Nano Lett* **2019,** *19* (3), 2128-2137.
14. Hu, J. J.; Liu, M. D.; Chen, Y.; Gao, F.; Peng, S. Y.; Xie, B. R.; Li, C. X.; Zeng, X.; Zhang, X. Z., Immobilized liquid metal nanoparticles with improved stability and photothermal performance for combinational therapy of tumor.

Biomaterials **2019,** *207*, 76-88.
15. Wang, D.; Gao, C.; Wang, W.; Sun, M.; Guo, B.; Xie, H.; He, Q., Shape-Transformable, Fusible Rodlike Swimming Liquid Metal Nanomachine. *ACS nano* **2018,** *12* (10), 10212-10220.
16. Fan, L.; Duan, M.; Sun, X.; Wang, H.; Liu, J., Injectable Liquid Metal- and Methotrexate-Loaded Microsphere for Cancer Chemophotothermal Synergistic Therapy. *ACS applied bio materials* **2020,** *3* (6), 3553-3559.
17. Zhang, Y.; Liu, M.-D.; Li, C.-X.; Li, B.; Zhang, X.-Z., Tumor Cell Membrane-Coated Liquid Metal Nanovaccine for Tumor Prevention‡. *Chinese Journal of Chemistry* **2020,** *38* (6), 595-600.
18. Hou, Y.; Zhang, P.; Wang, D.; Liu, J.; Rao, W., Liquid Metal Hybrid Platform-Mediated Ice-Fire Dual Noninvasive Conformable Melanoma Therapy. *ACS Appl Mater Interfaces* **2020,** *12* (25), 27984-27993.
19. Kumar, N.; Fazal, S.; Miyako, E.; Matsumura, K.; Rajan, R., Avengers against cancer: A new era of nano-biomaterial-based therapeutics. *Materials Today* **2021,** *51*, 317-349.
20. Zhang, C.; Xu, M.; Zeng, Z.; Wei, X.; He, S.; Huang, J.; Pu, K., A Polymeric Extracellular Matrix Nanoremodeler for Activatable Cancer Photo-Immunotherapy. *Angew Chem Int Ed Engl* **2023,** *62* (12), e202217339.
21. Wang, X.; He, S.; Cheng, P.; Pu, K., A Dual-Locked Tandem Fluorescent Probe for Imaging of Pyroptosis in Cancer Chemo-Immunotherapy. *Advanced Materials* **2023,** *35* (10), 2206510.
22. Zhang, C.; Xu, M.; He, S.; Huang, J.; Xu, C.; Pu, K., Checkpoint Nano-PROTACs for Activatable Cancer Photo-Immunotherapy. *Advanced Materials* **2023,** *35* (6), 2208553.
23. Matsumura, Y.; Maeda, H. J. C. r., A new concept for macromolecular therapeutics in cancer chemotherapy: mechanism of tumoritropic accumulation of proteins and the antitumor agent smancs. **1986,** *46* (12_Part_1), 6387-6392.
24. Bark, H.; Lee, P. S., Surface modification of liquid metal as an effective approach for deformable electronics and energy devices. *Chem Sci* **2021,** *12* (8), 2760-2777.
25. Yamaguchi, A.; Mashima, Y.; Iyoda, T., Reversible Size Control of Liquid-Metal Nanoparticles under Ultrasonication. *Angew Chem Int Ed Engl* **2015,** *54* (43), 12809-13.
26. Yu, Y.; Miyako, E., Manipulation of Biomolecule-Modified Liquid-Metal Blobs. *Angewandte Chemie International Edition* **2017,** *56* (44), 13606-13611.
27. Hemmi, H.; Kaisho, T.; Takeuchi, O.; Sato, S.; Sanjo, H.; Hoshino, K.; Horiuchi, T.; Tomizawa, H.; Takeda, K.; Akira, S., Small anti-viral compounds activate immune cells via the TLR7 MyD88-dependent signaling pathway. *Nature immunology* **2002,** *3* (2), 196-200.
28. Ma, F.; Zhang, J.; Zhang, J.; Zhang, C., The TLR7 agonists imiquimod and gardiquimod improve DC-based immunotherapy for melanoma in mice. *Cellular & molecular immunology* **2010,** *7* (5), 381-8.

29. Che, J.; Okeke, C. I.; Hu, Z. B.; Xu, J., DSPE-PEG: a distinctive component in drug delivery system. *Current pharmaceutical design* **2015,** *21* (12), 1598-605.
30. Wang, R.; Xiao, R.; Zeng, Z.; Xu, L.; Wang, J., Application of poly(ethylene glycol)-distearoylphosphatidylethanolamine (PEG-DSPE) block copolymers and their derivatives as nanomaterials in drug delivery. *Int J Nanomedicine* **2012,** *7*, 4185-98.
31. Hessel, C. M.; Pattani, V. P.; Rasch, M.; Panthani, M. G.; Koo, B.; Tunnell, J. W.; Korgel, B. A., Copper selenide nanocrystals for photothermal therapy. *Nano Lett* **2011,** *11* (6), 2560-6.
32. Li, Y.; Bai, G.; Zeng, S.; Hao, J., Theranostic Carbon Dots with Innovative NIR-II Emission for in Vivo Renal-Excreted Optical Imaging and Photothermal Therapy. *ACS Appl Mater Interfaces* **2019,** *11* (5), 4737-4744.
33. Li, J.; Pu, K., Semiconducting Polymer Nanomaterials as Near-Infrared Photoactivatable Protherapeutics for Cancer. *Acc Chem Res* **2020,** *53* (4), 752-762.
34. Cavaliere, R.; Ciocatto, E. C.; Giovanella, B. C.; Heidelberger, C.; Johnson, R. O.; Margottini, M.; Mondovi, B.; Moricca, G.; Rossi-Fanelli, A., Selective heat sensitivity of cancer cells. Biochemical and clinical studies. *Cancer* **1967,** *20* (9), 1351-81.
35. Ito, F.; Ernstoff, M., *Immune checkpoint inhibitors in cancer*. Elsevier Health Sciences: 2018.
36. De Sousa Linhares, A.; Battin, C.; Jutz, S.; Leitner, J.; Hafner, C.; Tobias, J.; Wiedermann, U.; Kundi, M.; Zlabinger, G. J.; Grabmeier-Pfistershammer, K.; Steinberger, P., Therapeutic PD-L1 antibodies are more effective than PD-1 antibodies in blocking PD-1/PD-L1 signaling. *Scientific reports* **2019,** *9* (1), 11472.
37. Ravindran, S.; Suthar, J. K.; Rokade, R.; Deshpande, P.; Singh, P.; Pratinidhi, A.; Khambadkhar, R.; Utekar, S., Pharmacokinetics, Metabolism, Distribution and Permeability of Nanomedicine. *Current drug metabolism* **2018,** *19* (4), 327-334.
38. Zhu, G. H.; Gray, A. B. C.; Patra, H. K., Nanomedicine: controlling nanoparticle clearance for translational success. *Trends in pharmacological sciences* **2022,** *43* (9), 709-711.
39. Shimada, E.; Matsumoto, Y.; Nakagawa, M.; Susuki, Y.; Endo, M.; Setsu, N.; Fujiwara, T.; Iida, K.; Nabeshima, A.; Yahiro, K.; Kimura, A.; Hirose, T.; Kanahori, M.; Oyama, R.; Oda, Y.; Nakashima, Y., Methylation-mediated silencing of protein kinase C zeta induces apoptosis avoidance through ATM/CHK2 inactivation in dedifferentiated chondrosarcoma. *British journal of cancer* **2022,** *126* (9), 1289-1300.
40. Tollemar, V.; Tudzarovski, N.; Boberg, E.; Törnqvist Andrén, A.; Al-Adili, A.; Le Blanc, K.; Garming Legert, K.; Bottai, M.; Warfvinge, G.; Sugars, R. V., Quantitative chromogenic immunohistochemical image analysis in cellprofiler software. *Cytometry. Part A : the journal of the International Society for Analytical Cytology* **2018,** *93* (10), 1051-1059.

Chapter 4

Ionic liquid-modified carbon nanohorns as magnetically driven photothermal nanoconjugates

4.1 Introduction

4.1.1 Introduction of ionic liquid

Room temperature ionic liquids (RTILs) are a new class of organic soft materials, with the characteristics of low flammability, negligible vapor pressure, ionic conductivity, and chemical and thermal stability. Due to these attributes, RTILs have found wide applications in fields such as electrochemistry, soft materials gel, organic synthesis, bioengineering, and pharmaceuticals.[1-5] Notably, some studies have reported that RTILs exhibit promising anticancer properties in some cancer cell lines, prompting recent interest in exploring RTILs as novel anticancer agents.[6-10] 1-butyl-3-methylimidazolium tetrachloroferrate ([Bmim][$FeCl_4$]) is a special room temperature ionic liquid that is paramagnetic due to the presence of high-spin $FeCl_4$ anions and can respond to external magnetic fields. This magnetic ionic liquid combines the favorable properties of ionic liquids with magnetism, making it attractive for expanded applications. This special property suggests that we can control the movement of particles through an external magnetic field, providing a new solution for the synthesis of a new type of magnetically controllable nanophotosensitizer.

4.1.2 Introduction of carbon nanohorns

Carbon nanohorns (CNHs) are a promising material with high surface area and microporosity. Due to their unique structure and ideal size, CNHs become a promising material in the application of sensor, gas storage, adsorption, and catalyst support.[11-13] Furthermore, due to their biocompatibility and low cytotoxicity, CNHs are widely utilized in the biomedical field as carriers for the delivery of drug molecules or antibodies[14, 15], as well as for *in vivo* bioimaging applications[16, 17]. In particular, CNHs have been employed in PTT for tumor eliminating due to their strong photothermal conversion capabilities in the NIR region.[18, 19] However, efficiently delivering CNHs nanoparticles in substantial quantities to tumors presents a significant challenge. As previously introduced, while the enhanced permeability and retention (EPR) effect can lead to increased accumulation of nanoparticles in tumor tissues compared to normal tissues, only a small fraction of the total administered dose typically reaches solid tumors.[20] This limitation significantly hampers the broader application of CNHs nanoparticles as novel functionalized nanoparticles in cancer treatment. It is crucial to synthesize a highly targeted CNHs-based nanocomplex as a novel type of photothermal agent.

4.1.3 Objective of this study

In this chapter, we propose a novel type of magnetically driven functional nanoconjugates based on IL and CNHs. We intend to encapsulate IL in CNHs as a potential drug delivery system. Due to the loading of IL, the IL-CNHs nanoconjugates will be magnetically responsive. By fixing the rubidium magnet at the tumor site, more IL-CNHs nanoconjugates will accumulate at the tumor site under the action of the magnetic field. Notably, CNHs have high photothermal conversion capability, thus enabling more precise photothermal therapy. In addition, loading drugs on IL-CNHs is also expected to enable controllable drug delivery and release using magnetic fields. This study pioneers the first use of magnetic ionic liquids in cancer treatment, offering a promising platform for advanced nanotheranostics.

4.2 Materials and Methods

4.1.1 Nanoconjugates synthesis

The [Bmim][$FeCl_4$]–PEG–CNH nanoconjugates were prepared as follows. Basically, 1 mg of CNHs (average diameter, ≈ 80–100 nm; purity, 95%; metal-free, NEC Corporation, Tokyo, Japan), 1 mg of DSPE–PEG_{2000}–NH_2 (NOF Corporation, Tokyo, Japan), and 200 µl (275.52 mg) of [Bmim][$FeCl_4$] (Tokyo Chemical Industry, Tokyo, Japan) was mixed with 10 ml PBS buffer (Wako Pure Chemical, Osaka, Japan) by pulse-type sonication (VCX-600; Sonics, Danbury, CT, USA) for 10 min with crushed ice. The control CNHs nanoconjugates without magnetism were prepared in a similar way except for adding [Bmim][$FeCl_4$]. In addition, [Bmim][$FeCl_4$]–PEG–CNH or PEG–CNH suspension in high concentration was prepared by increasing the amount of CNHs and DSPE–PEG_{2000}–NH_2 in the same ratio.

The ICG functionalized [Bmim][$FeCl_4$]–PEG–CNH nanoconjugates ([Bmim][$FeCl_4$]–PEG–ICG–CNH) were prepared as follows. 0.1 mg of ICG (Tokyo Chemical Industry) was mixed with 1 ml of prepared [Bmim][$FeCl_4$]–PEG–CNH suspension (CNHs concentration = 0.1 mg ml^{-1}) and stirred up for 1h with dark conditions.

Additionally, highly concentrated [Bmim][$FeCl_4$]–PEG–ICG–CNH suspension was prepared by using increasing the amounts of [Bmim][$FeCl_4$]–PEG–CNH and ICG in the same ratio.

4.1.2 Nanoconjugates structural and optical characterization

The morphology and structure of [Bmim][$FeCl_4$]–PEG–CNH nanoconjugates were observed under a high-resolution transmission electron microscope (TEM) (JEM-2100F, Japan Electron Optics Laboratory, Tokyo, Japan). The hydrodynamic diameter of the [Bmim][$FeCl_4$]–PEG–CNH nanoconjugate was measured using dynamic light scattering (DLS) (Zetasier Nano ZS; Malvern Panalytical, UK). The optical absorbance and fluorescence (FL) of the [Bmim][$FeCl_4$]–PEG–CNH and [Bmim][$FeCl_4$]–PEG–ICG–CNH suspension was measured by using UV-vis-NIR (V-730 BIO; Jasco, Tokyo, Japan) and FL spectrometers (FP-8600 NIR Spectrofluorometer; Jasco), respectively. The amounts of PEG and [Bmim][$FeCl_4$] conjugated with CNH were estimated by TG analysis (TG-DTA8122; Rigaku, Tokyo, Japan). TGA traces were recorded for the series using a ramp rate of 5 °C/min in air. The [Bmim][$FeCl_4$]–PEG–CNH and PEG–CNH were synthesized by the same way as the above protocol of nanocomplex synthesis except for using distilled water instead of PBS. The freeze dried [Bmim][$FeCl_4$]–PEG–CNH and PEG–CNH was prepared by a freeze dryer (FDU-1200; EYELA, Tokyo, Japan) before TG measurements.

4.1.3 Photothermal conversion

[Bmim][$FeCl_4$]–PEG–CNH suspension and PBS buffer were irradiated with an 808 nm NIR laser (Civil Laser, Hangzhou, Zhejiang, China) at [0.7W (~35.6 mW mm^{-2}; spot diameter ~3 mm), and 0.3 W (~15.3 mW mm^{-2})] powers under the indicated conditions. The temperature of the solutions was measured in real-time using a temperature sensor (AD-5601A; A&D, Tokyo, Japan). Thermographic images were recorded using infrared thermography (i7, E6; FLIR, Nashua, NH, USA).

The photothermal stability of [Bmim][$FeCl_4$]–PEG–CNH nanoconjugates were determined as follows. 100 μl of [Bmim][$FeCl_4$]–PEG–CNH suspension was diluted with 1.9 ml of PBS buffer. And irradiated with an 808 nm NIR laser for 5 min at 0.7 W (~35.6 mW mm^{-2}, spot diameter ~3 mm). Analyzed the optical absorbance spectra of before- and after-laser by using the UV-vis-NIR spectrometer.

4.1.4 Controllable Movement of [Bmim][$FeCl_4$]–PEG–CNH droplet

The [Bmim][$FeCl_4$]–PEG–CNH droplet (~20 μl) was pipetted to the liquid surface of dish (diameter 90 mm; ND90-15, AS ONE, Osaka, Japan) containing 10 ml of 3M™ Novec™ 7300 Engineered Fluid (3M, MN, USA). The magnetic-driven movement was observed by placing a neodymium magnet obliquely above the droplet (distance ~1.5 cm) and the direction of movement was adjusted by moving the neodymium magnet. Similarly, the light-driven movement was observed by using the 808 nm NIR laser (0.7 W, ~35.6

mW mm^{-2}; spot diameter ~3 mm) to irradiate the edge of the droplet, the direction of movement was adjusted by changing the direction of laser irradiation.

4.1.5 Cell culture and viability

Murine colon carcinoma (Colon26) cells and normal diploid lineage bud (TIG-103) cells were obtained from the Japanese Collection of Research Bioresources Cell Bank (Tokyo, Japan). The Colon26 cell line was cultured in Roswell Park Memorial Institute (RPMI) 1640 medium (Nacalai Tesque, Kyoto, Japan) containing 10% fetal bovine serum (FBS), 2 mM of L-glutamine, 1 mM of sodium pyruvate, gentamycin, and 100 IU ml^{-1} of penicillin-streptomycin. The TIG-103 cells were cultured in Eagle's minimal essential medium (Nacalai Tesque) containing 10% FBS, 2 mM of L-glutamine, 1 mM of sodium pyruvate, gentamycin, 100 IU ml^{-1} penicillin-streptomycin. Both of cells were maintained at 37 °C in a humidified chamber containing 5% CO_2. They were subsequently cryopreserved in liquid nitrogen in multiple vials. The cell stocks were regularly revived to avoid genetic instability associated with high passage numbers.

Cell viability was assessed using a Cell Counting Kit-8 (CCK-8) (Dojindo Laboratories, Kumamoto, Japan) according to the manufacturer’s instructions. Briefly, 5,000 cells per well were seeded in 96-well plates, allowed to adhere overnight, then exposed to nanoconjugates, and laser-irradiated as indicated. After washing with fresh medium, the cells were incubated with 10 μl of CCK-8 for 3 h at 37 °C in a humidified chamber containing 5% CO_2. The absorbance at 450 nm was determined using a microplate reader (Infinite M200 PRO; Tecan, Männedorf, Switzerland).

4.1.4 Intracellular penetration of [Bmim][FeCl$_4$]–PEG–CNH

Colon26 cells (2.5 × 10^5 cells per dish) were seeded in poly-L-lysine coated 35 mm glass bottom dishes (Matsunami glass, Osaka, Japan) and allowed to adhere overnight. Cells were then exposed to [Bmim][FeCl$_4$]–PEG–CNH (CNHs concentration = 0.1 mg ml^{-1}) suspension for 24 h at 37 °C in a humidified incubator containing 5% CO$_2$. After washing thoroughly with fresh PBS buffer, Colon26 cells were observed using a microscopy system equipped with a mirror unit (IRDYE800-33LP-A-U01; Semrock, Lake Forest, IL, USA) and an objective lens (×40 magnification, aperture 0.95; UPLSAPO20X, Olympus, Tokyo, Japan) at room temperature. For FL bioimaging, the Colon26 cells were incubated with 0.1 mg ml^{-1} of [Bmim][FeCl$_4$]–PEG–ICG–CNH suspension (CNHs concentration = 0.1 mg ml^{-1}, ICG concentration = 0.1 mg ml^{-1}) in a similar manner. After washes with PBS buffer, the cells were examined, and images were acquired using a FL microscope (BZ-X800, Keyence, Tokyo, Japan).

4.1.5 Direct observation of laser-driven cancer cell destruction

In a similar way, Colon26 cells (2.5 × 10^5 cells per dish) were seeded in 35 mm glass bottom dishes and cultured to adhere overnight. [Bmim][FeCl$_4$]–PEG–CNH suspension (CNHs concentration = 100 μg ml^{-1}) or fresh PBS buffer was added to the dishes for 24 h. After washing three times with PBS buffer, the cells were maintained in RPMI medium.

The destruction of cancer cells triggered by laser-induced nanoconjugates using the laser irradiation setup was performed as follows. An 808 nm, 254 mW (~129 mW mm^{-2}) NIR laser beam from a continuous-wave diode laser (Sigma Koki, Tokyo, Japan) was incorporated into a microscopy system (IX73, Olympus). The laser beam (spot diameter ~50 μm) was focused on the target position (× 40 magnification; aperture 0.95; UPLSAPO40X, Olympus) at room temperature for 3 s. The videos were recorded using an electron-multiplying, charge-coupled device camera system (DP80, Olympus) before and during irradiation.

4.1.6 *In vivo* anticancer therapy

The animal experiments were conducted following the protocols approved by the Institutional Animal Care and Use Committee of the Japan Advanced Institute of Science and Technology (JAIST) (No. 04-007). All the mice were obtained from Japan SLC (Hamamatsu, Japan) (female; 5 weeks old; n = 40; average weight = 16 g; BALB/cCrSlc). Colon26 cell-derived mouse tumors were generated by injecting 100 μl Matrigel® Matrix (mixed with RPMI medium, v/v = 1:1; Dow Corning, Corning, NY, USA) containing 1×10^6 cells into the dorsal right side of the mice. After approximately 1 week, when the tumor volume reached ~100 mm^3, the mice were intravenously injected with 200 μl of [Bmim][$FeCl_4$]–PEG–CNH suspension (CNHs concentration = 1 mg ml^{-1}, [Bmim][$FeCl_4$] concentration = 10 μl ml^{-1}), PEG–CNH suspension (CNHs concentration = 1 mg ml^{-1}), or fresh PBS buffer respectively. Especially, for magnetic groups, the neodymium magnet (diameter ~6 mm; magnetic flux density ~230 mT, Okazaki, Wakayama, Japan) was fixed on the tumor top by medical bandage (NICHIBAN, Tokyo, Japan). The dorsal right-side tumors were irradiated for 5 min every day 24 h after sample injection (a total of four laser irradiation sessions) using an 808 nm laser (0.7 W, ~35.6 mW mm^{-2}, spot diameter ~3 mm). Thermographic measurements were conducted during irradiation using infrared thermography. Tumor formation and overall health (vitality and body weight) were monitored every other day. The tumor volumes were calculated using the formula $V = L \times W^2/2$, where L and W denote the length and width of the tumor, respectively. When the tumor volumes reached 1,500 mm^3, the mice were euthanized according to the JAIST Institutional Animal Care and Use Committee guidelines.

4.1.7 *In vivo* fluorescent bio-imaging

To monitor the chronological changes in FL intensity due to the [Bmim][$FeCl_4$]–PEG–CNH nanoconjugates tumor-targeting effect, Colon26 tumor-bearing mice (female; 6 weeks old; n = 4; average weight = 18 g; average tumor size = 100 mm^3; BALB/cCrSlc) were injected intravenously with 200 µl of PBS or [Bmim][$FeCl_4$]–PEG–CNH nanoconjugates suspension (ICG concentration = 1 mg ml^{-1}, CNHs concentration = 1 mg ml^{-1}) The mice were euthanized, and the major organs, including the heart, liver, spleen, lungs and kidneys, in addition to the tumor, were imaged using an *in vivo* FL imaging system (VISQUE™ InVivo Smart-LF, Vieworks, Anyang, Republic of Korea) with a 3 s exposure time and an ICG filter (Ex, 740–790 nm; Em, 810–860 nm) at 4, 8, 12 and 24 h postinjection. The FL images were acquired and analyzed using CleVue™ software.

4.1.8 Immunohistochemistry staining of tumor tissues

Colon26 tumor-bearing mice (n = 4) were euthanized on the day after sample intravenous injection and laser irradiation. Subsequently, tumor tissue from the treatment groups was harvested for immunohistochemistry (IHC) staining. IHC analysis was performed by the Biopathology Institute Co., Ltd. (Oita, Japan) with standard protocols. Briefly, primary tumors were surgically removed, fixed in 10% formalin, processed for paraffin embedding, and cut into 3–4 μm sections. After incubation with the primary antibody (**Table 4-1**), the sections were stained with hematoxylin and eosin and examined using light microscopy (IX73, Olympus). The areas showing positive staining in tumor tissues were analyzed using a light microscopy system (BZ-X800, Keyence) and hybrid cell count and microcell count software (Keyence).

Table 4-1 Antibodies used in this study.

Antibody	Type	Source	Catalog No.	Application
Anti-digoxigenin-peroxidase	Sheep Polyclonal	Merck Millipore	S7100	Tunel
Caspase-3	Rabbit Polyclonal	Cell Signaling Technology	9661S	IHC (1:100)

4.1.9 Safety tests

The complete blood count (CBC) was measured using a Celltac α blood cell counting machine (Microsemi LC-712; HORIBA, Japan), and biochemical parameters were investigated by Oriental Yeast Co. (Tokyo, Japan). BALB/cCrSlc mice (female; 6 weeks; n = 5; average weight = 18 g; Japan SLC, Inc.) were injected in the tail vein with PBS buffer (200 μl) or [Bmim][$FeCl_4$]–PEG–ICG–CNH nanocomplex (200 μl, CNH concentration = 1 mg ml^{-1}. Blood samples were collected from the inferior vena cava of each mouse after 7 days.

Vital organ tissues from the different treatment groups were harvested after nanocomplex administration for 7 days for histological staining. All surgeries were performed under anaesthesia and all efforts were made to relieve suffering. The histology of liver, spleen, heart, lungs, and kidney was analysed using a light microscopy system (BZ-X800). H&E staining was performed by the Biopathology Institute Co., Ltd.. Briefly, excised organ tissues were fixed in 10% neutral buffered formalin for at least 48 h, then dehydrated with increasing concentrations of ethanol and embedded in paraffin. Tissue sections of 3–4 μm thick were attached to positively charged glass slides and stained with H&E.

4.1.10 Statistical analysis

All experiments were performed in triplicates and repeated three or more times. Quantitative values are expressed as the mean ± standard error of the mean (SEM) of at least three independent experiments. Statistical differences were identified by the Student's *t-test* or Log-rank (Mantel-Cox) test using GraphPad Prism, version 9.4.0 (GraphPad Software, Boston, MA, USA). A P value of less than 0.05 was considered statistically significant.

4.3 Result and Discussion

4.3.1 Characterizations of nanoparticles

CNH nanoparticles are inherently insoluble in water, but their water dispersibility can be enhanced through surfactant modification. [Bmim][$FeCl_4$] also exhibits hydrophobic properties. As introduced **Chapter 3**, 1,2-distearoyl-sn-glycero-3-phosphoethanolamine-N-[amino(polyethylene glycol)−2000] (DSPE–PEG_{2000}–NH_2) is one of the useful surfactant for biomedical applications because of its high biocompatibility and excellent high versatility for improvement of water-dispersibility of various materials.[21, 22] In this study, we developed a simple and effective preparation method for synthesizing water-dispersible [Bmim][$FeCl_4$]-modified CNH nanoconjugates by utilizing DSPE–PEG_{2000}–NH_2, chosen for its high biocompatibility and versatility. Using a conventional pulsed ultrasound method, we synthesized PEG-modified CNH nanoconjugates with excellent water dispersibility. (**Figure 4.1**) The prepared [Bmim][$FeCl_4$]–PEG–CNH suspension was black, and no precipitation was observed after standing overnight at room temperature, indicating that the surface-modified nanoparticle suspension had high dispersibility and stability (**Figure 4.2**).

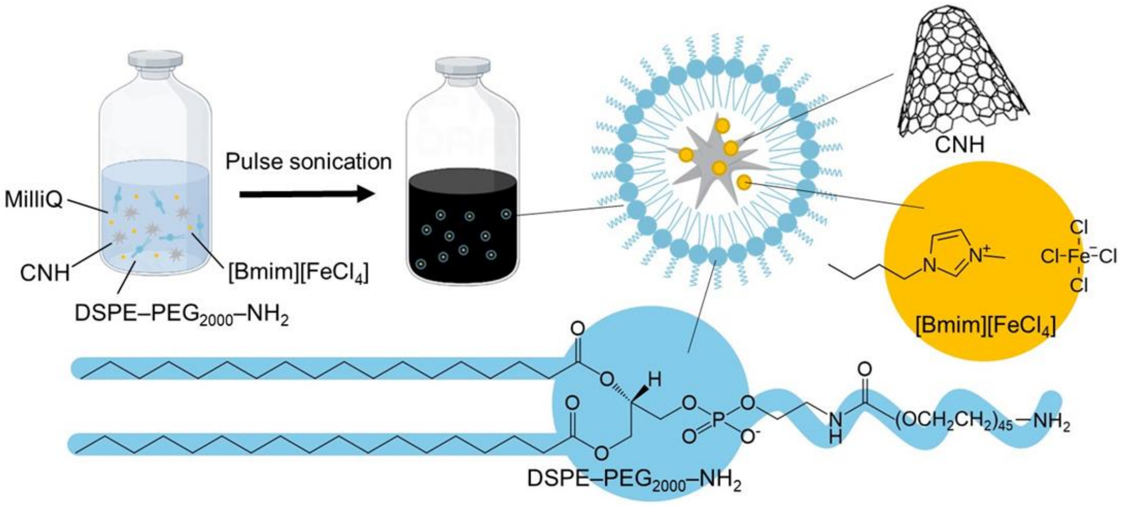

Figure 4.1 Synthesis scheme of the preparation of [Bmim][$FeCl_4$]–PEG–CNH nanoconjugates.

Figure 4.2 Image of the prepared [Bmim][$FeCl_4$]–PEG–CNH aqueous suspension.

Dynamic light scattering (DLS) measurements also further confirmed the stability of [Bmim][$FeCl_4$]–PEG–CNH. The diameter of [Bmim][$FeCl_4$]–PEG–CNH nanoconjugates in aqueous dispersion remained at ~160 nm and maintained almost unchanged particle size for at least 7 days (**Figure 4.3**). Transmission electron microscopy

(TEM) images further showed the morphology and particle size (diameter ~160 nm) of well-dispersed [Bmim][FeCl4]–PEG–CNH nanoconjugate suspension, which was consistent with the DLS results (**Figure 4.4**). The above data indicates that the prepared [Bmim][FeCl4]–PEG–CNH has a small particle size and a stable structure, which provides the possibility for further investigation of its characteristics.

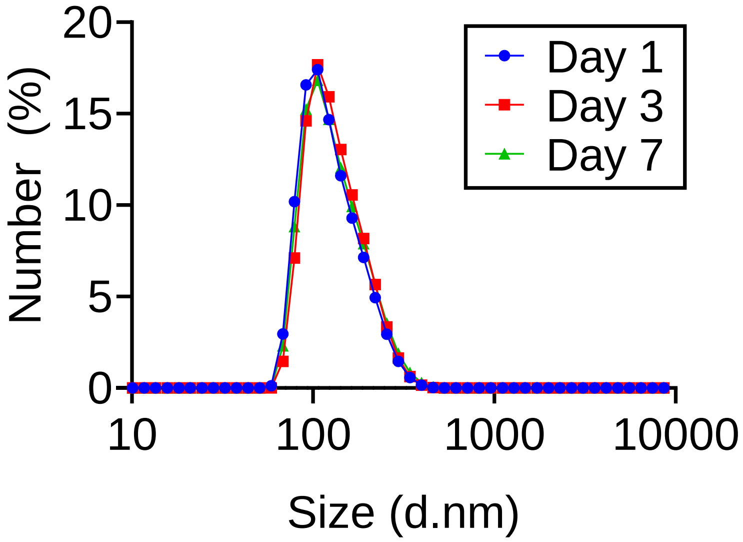

Figure 4.3 DLS results of [Bmim][FeCl4]–PEG–CNH on 1-, 3- and 7-days after incubation at 25 °C.

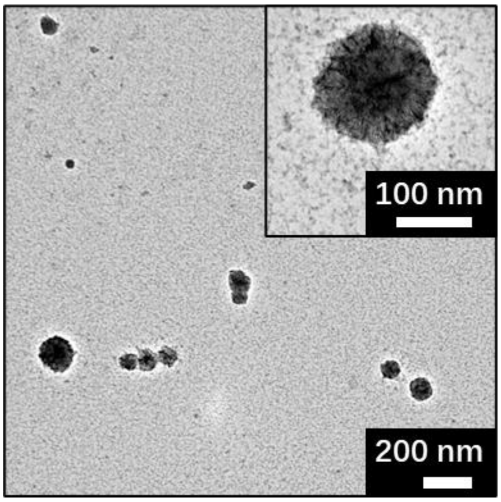

Figure 4.4 The TEM images of [Bmim][$FeCl_4$]–PEG–CNH nanoconjugates. Inlet is magnified view of the conjugate.

Additionally, the ultraviolet–visible–near-infrared (UV–vis–NIR) absorption spectra of [Bmim][$FeCl_4$]–PEG–CNH and PEG–CNH in aqueous solution were further analyzed. The results showed that absorption was observed in the near-infrared (NIR) region and the absorbance increased linearly with the increase in CNHs concentration. Notably, a characteristic peak of [Bmim][$FeCl_4$] appeared in the spectra of [Bmim][$FeCl_4$]–PEG–CNH around 560 nm, due to the conjugation of [Bmim][$FeCl_4$] with CNHs (**Figure 4.5**).[23] We thus estimated that almost [Bmim][$FeCl_4$] molecules could be sufficiently loaded onto the surface of CNH via hydrophobic and π-π interactions, since no ionic liquid layer was observed in the prepared vials and no aggregation from the DLS results. Overall, these data suggest that PEG-modified CNH nanoparticles can effectively encapsulate [Bmim][$FeCl_4$] molecules while maintaining dispersing stability, highlighting their potential as light-responsive nanodrug in cancer therapy. We also believe that anionic

[$FeCl_4$] molecules are loaded onto CNH by ionic interaction with cationic [Bmim] molecules. In fact, thermogravimetric analysis (TGA) showed that approximately 0.98 mg of PEG and 273 mg of [Bmim][$FeCl_4$] were coated on surface of 1 mg of CNH (**Figure 4.6**). The loading efficiency of PEG and [Bmim][$FeCl_4$] onto CNH are 98% and 99%, respectively. By using a UV–vis–NIR spectrometer, we could also make sure that 98% [Bmim][$FeCl_4$] was remained within nanocomplexes even after filtration (**Figure 4.7**). These results clearly indicate that [Bmim][$FeCl_4$] and PEG molecules are surely attached on the surface of CNH.

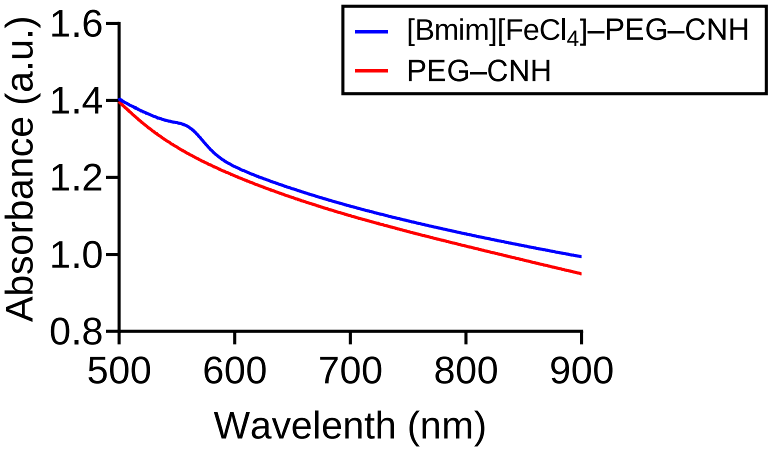

Figure 4.5 UV–vis–NIR absorption spectra of [Bmim][$FeCl_4$]–PEG–CNH and PEG–CNH suspension.

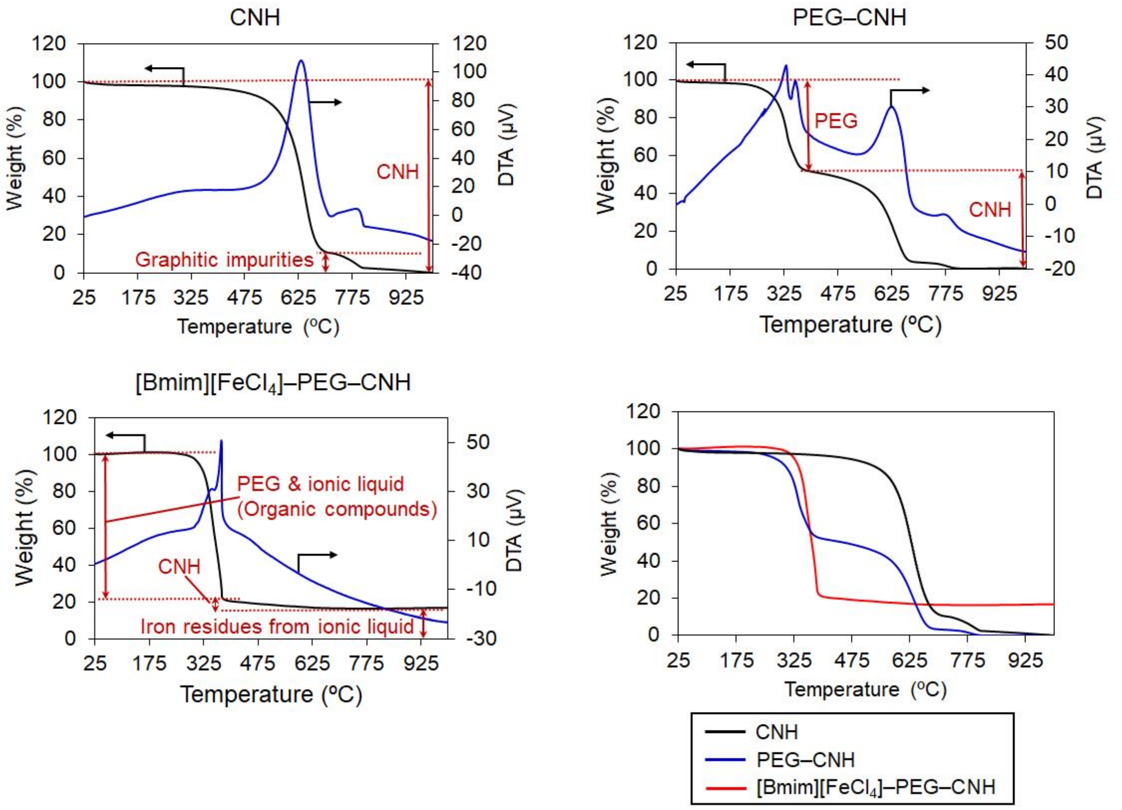

Figure 4.6 Thermogravimetric analysis (TGA) of CNH, PEG–CNH, and [Bmim][FeCl$_4$]–PEG–CNH.

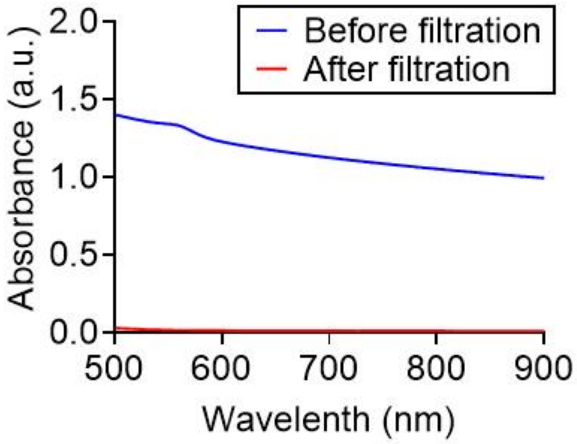

Figure 4.7 UV–vis–NIR absorption spectra of the filtrate of [Bmim][FeCl$_4$]–PEG–CNH. The aqueous suspension was filterd (0.22 µm-polytetrafluoroethylene syringe filter, Osaka Chemical, Osaka, Japan) before the measurement.

Subsequently, the photothermal conversion capability of [Bmim][$FeCl_4$]–PEG–CNH was evaluated based on their absorbance at the NIR region. Under 808 nm NIR laser irradiation, the temperature increase (ΔT) at a power of 0.7 W (~35.6 mW mm^{-2}) and 0.3 W (~15.3 mW mm^{-2}) was measured for various concentrations of [Bmim][$FeCl_4$]–PEG–CNH suspensions using a thermocouple. The results showed that the ΔT of each [Bmim][$FeCl_4$]–PEG–CNH suspension increased with prolonged laser irradiation, while the MilliQ water control exhibited almost no temperature rise. As shown in **Figure 4.8**, the temperature of 100 μg ml^{-1} [Bmim][$FeCl_4$]–PEG–CNH suspension increased 40.7 °C under the power of 0.7 W laser irradiation during 5 min. By adjusting the CNHs concentration or laser power and irradiation duration, we can easily control the temperature, thereby enhancing the operability and precision of [Bmim][$FeCl_4$]–PEG–CNH for potential photothermal therapy applications.

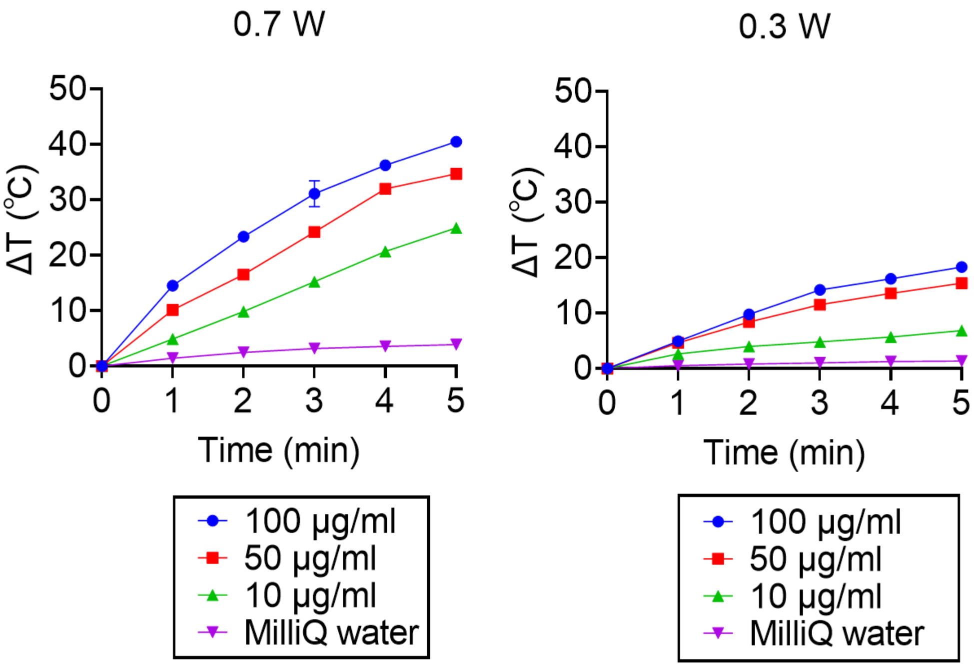

Figure 4.8 Laser-induced temperature increase in MilliQ water (control) and [Bmim][$FeCl_4$]–PEG–CNH suspension at different concentrations and different powers of NIR laser.

Figure 4.9 presents thermographic images illustrating the temperature changes in [Bmim][$FeCl_4$]–PEG–CNH suspensions before and after laser irradiation. These images support similar conclusions, showing that at a laser power of 0.7 W, the surface temperature of a 100 µg ml^{-1} [Bmim][$FeCl_4$]–PEG–CNH suspension significantly increased, reaching approximately 69 °C after 5 minutes of irradiation. Furthermore, suspensions with different concentrations of [Bmim][$FeCl_4$]–PEG–CNH (10 µg ml^{-1}, 50 µg ml^{-1}, or 100 µg ml^{-1}) exposed to a lower laser power of 0.3 W (~15.3 mW mm^{-2}) also exhibited varying degrees of temperature increase after 5 minutes of irradiation, demonstrating concentration-dependent photothermal effects.

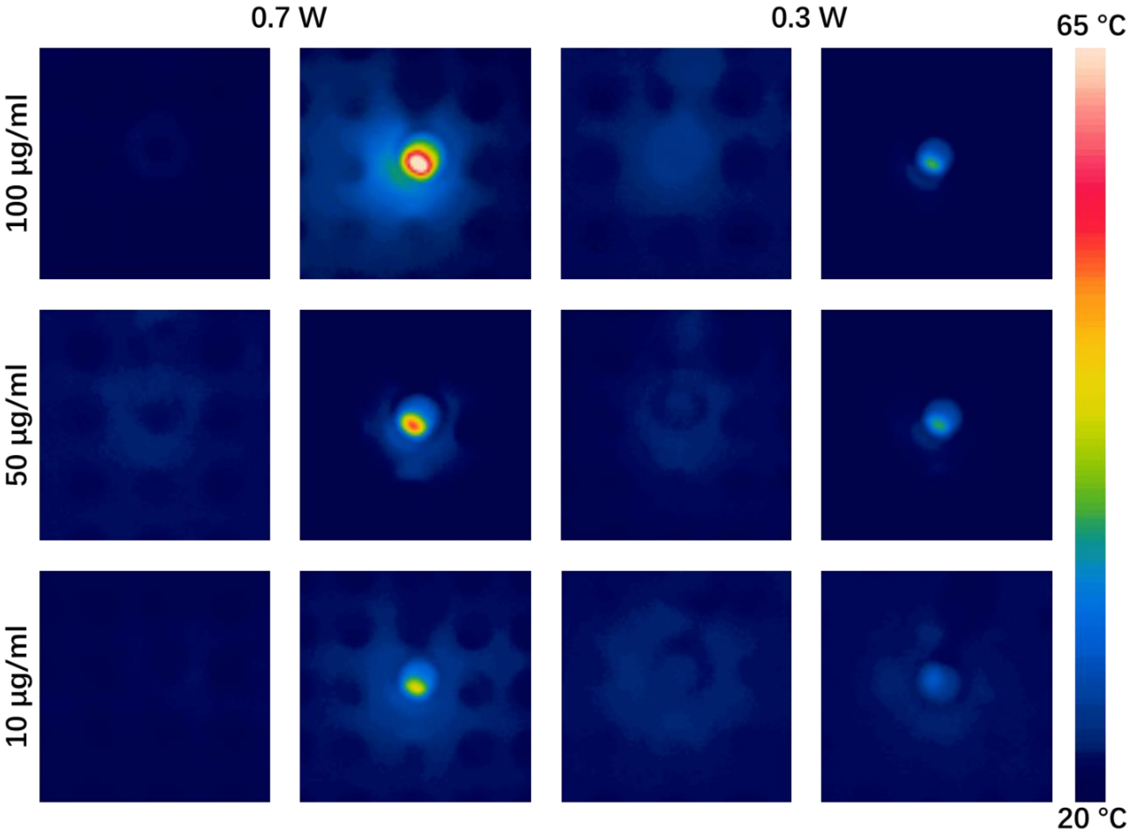

Figure 4.9 Thermographic images of various concentrations of [Bmim][$FeCl_4$]–PEG–CNH suspension after 5-min laser irradiation at NIR laser powers of 0.7 and 0.3 W.

The photothermal stability of [Bmim][$FeCl_4$]–PEG–CNH was evaluated using a laser on/off cycling test. Under 0.7 W NIR laser irradiation, [Bmim][$FeCl_4$]–PEG–CNH underwent four cycles of heating and natural cooling. The maximum temperatures reached after each cycle of laser irradiation remained consistent, demonstrating the excellent photothermal stability of the nanoconjugates (**Figure 4.10**). Notably, from the second cycle onwards, the maximum temperatures were slightly higher than in the first cycle. This can be attributed to incomplete cooling after the first cycle, where the temperature at the end of the cooling phase (10 min) did not return to the initial baseline (0 min), and this discrepancy disappeared in subsequent cycles. Additionally, the UV−vis−NIR optical absorption spectra of the [Bmim][$FeCl_4$]–PEG–CNH suspension before and after laser irradiation showed no change in absorbance, confirming that the nanoconjugates did not undergo degradation during NIR laser exposure (**Figure 4.11**).

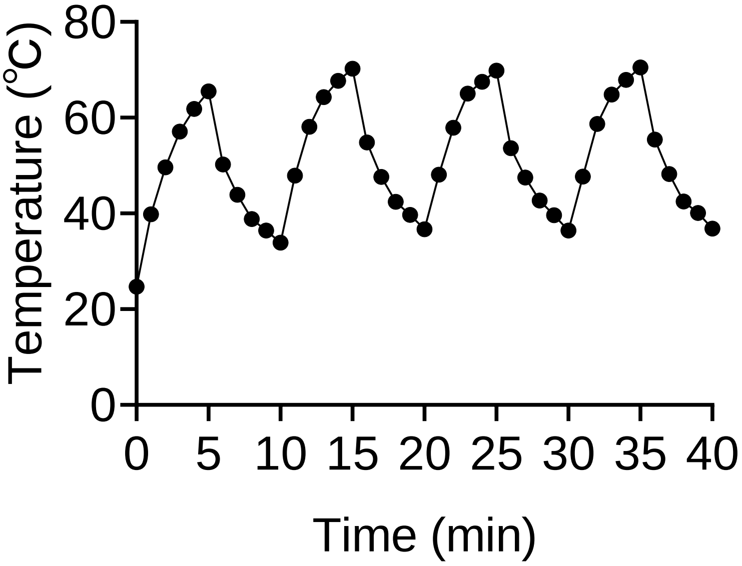

Figure 4.10 Stability testing of the [Bmim][$FeCl_4$]–PEG–CNH suspension under photothermal heating and natural cooling cycles by 808 nm laser irradiation.

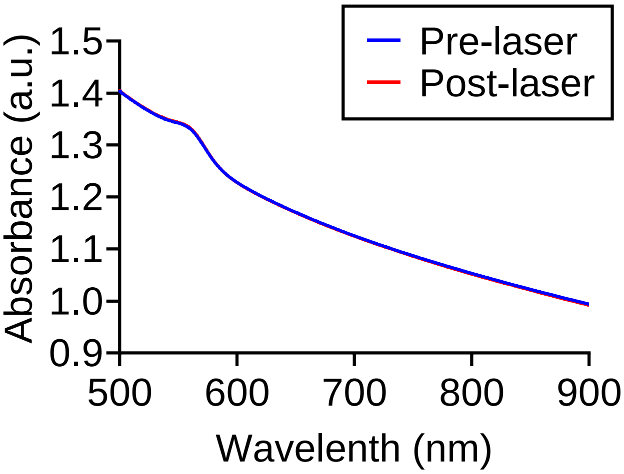

Figure 4.11 UV–vis–NIR absorption spectra of [Bmim][$FeCl_4$]–PEG–CNH pre- and post-laser irradiation at 0.7 W power for 5 min.

The photothermal conversion efficiency of [Bmim][$FeCl_4$]–PEG–CNH at 808 nm was calculated to be 63%. In comparison, other photothermal nanomaterials, such as metal-based materials, carbon dots, and semiconductor polymer nanoparticles, exhibit lower conversion efficiencies than [Bmim][$FeCl_4$]–PEG–CNH.[24-26] (**Table 4-2**) This superior efficiency highlights the potential of [Bmim][$FeCl_4$]–PEG–CNH as a highly effective photothermal agent for cancer photothermal therapy.

Table 4-2 The photothermal conversion efficiency of materials in previous reports

Material	Photothermal conversion efficiency (%)	Reference
[Bmim][$FeCl_4$]–PEG–CNH	63	This study
Gold nanorods	21	24
Gold nanoshells	13	24
Copper selenide	22	24
Carbon dots	31	25
Semiconducting polymer nanoparticles	37	26

As magnetic ionic liquid, [Bmim][$FeCl_4$] exhibits a strong response to external magnetic fields. By using this property, we tested the ability of [Bmim][$FeCl_4$]–PEG–CNH droplets to move under a magnetic field. When a neodymium magnet was brought near the [Bmim][$FeCl_4$]–PEG–CNH droplet from above, the droplet was attracted and moved toward the magnet. By adjusting the magnet's position, the trajectory of the droplet could be precisely controlled (**Figure 4.12A**). Interestingly, when irradiated with the 0.7W of NIR laser, the powerful photothermal conversion ability of CNHs generated thermal convection at air-liquid interface, caused the dynamic motion of the [Bmim][$FeCl_4$]–PEG–CNH droplet in a fluorous solvent (**Figure 4.12B**). The temperature of the [Bmim][$FeCl_4$]–PEG–CNH droplet reached at 36.5 °C from about 21.0 °C just after laser irradiation (**Figure 4.13**). In contrast, only the [Bmim][$FeCl_4$] droplet could not be moved by laser irradiation because of the absence of photothermal conversion and absorbance in NIR region. Briefly, the surface-tension gradient (thermal convection) can be generated by a temperature gradient. The natural flow of liquid due to different surface tensions, resulting in the spontaneous movement of liquids.[27, 28] This combination of magnetic and photothermal control offers the potential for precise manipulation of [Bmim][$FeCl_4$]–PEG–CNH, opening new possibilities for their application in targeted therapies and controlled delivery systems.

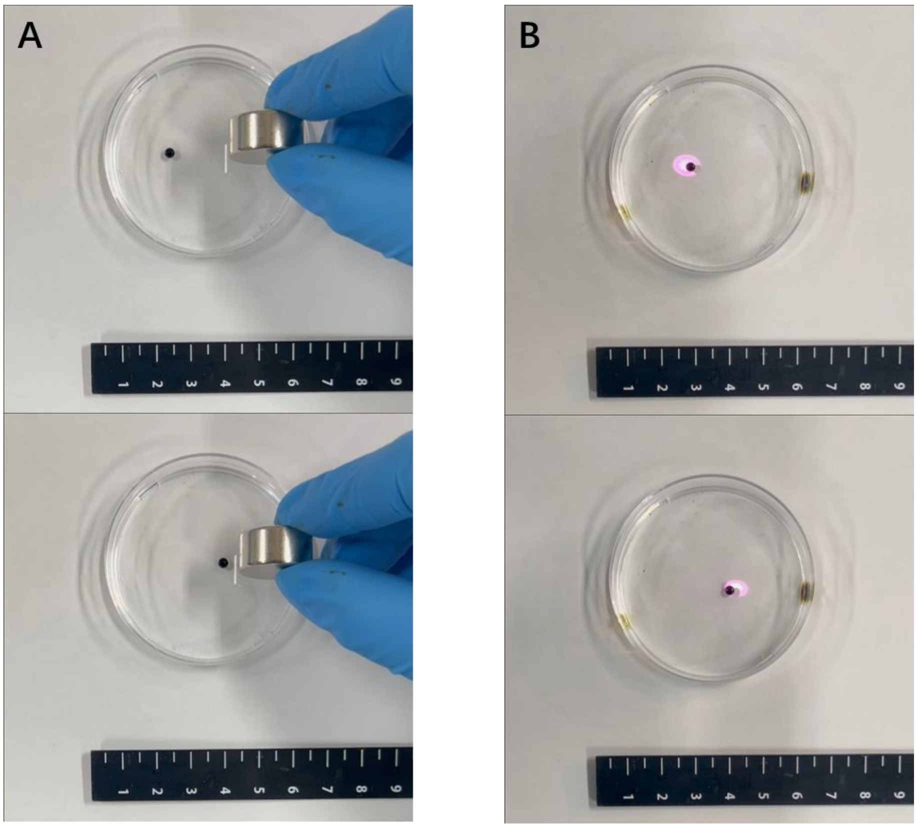

Figure 4.12 The movement of [Bmim][$FeCl_4$]–PEG–CNH droplet by **A)** magnet and **B)** laser irradiation.

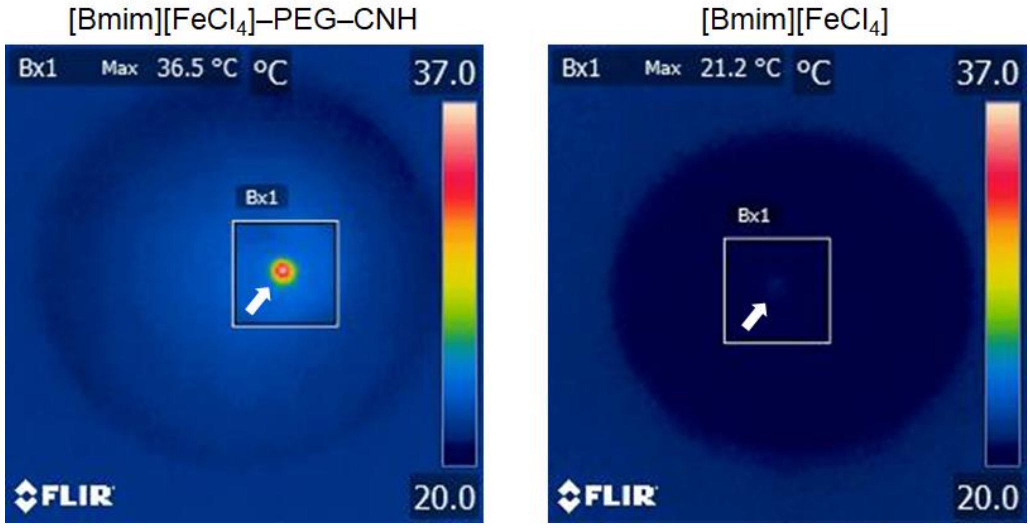

Figure 4.13 Thermographic image of [Bmim][FeCl$_4$]–PEG–CNH and [Bmim][FeCl$_4$] droplet in a fluorous solvent after laser irradiation at NIR laser powers of 0.7 W (~35.6 mW mm^{-2}). The white arrows represent the location of [Bmim][FeCl$_4$]–PEG–CNH and [Bmim][FeCl$_4$] droplets.

4.3.2 *In vitro* anticancer efficacy of [Bmim][FeCl$_4$]–PEG – CNH nanoparticles

The high biocompatibility and low toxicity of CNHs have been confirmed by many research groups.[14-17] After characterizing various properties of synthesized CNHs nanoconjugates, the cytotoxicity was evaluated using normal diploid fibroblast cells (TIG-103) cells and murine colon carcinoma (Colon26) cells. The cells were incubated for 24 hours with varying concentrations of PEG–CNH and [Bmim][FeCl$_4$]–PEG–CNH nanoconjugates respectively. PEG–CNH suspension at different concentrations exhibited no cytotoxicity toward either TIG-103 or Colon26 cells (**Figure 4.14**). In contrast, after encapsulating the ionic liquid, the [Bmim][$FeCl_4$]–PEG–CNH nanoconjugates demonstrated cytotoxicity in both cell lines. Notably, the [Bmim][$FeCl_4$]–PEG–CNH nanoconjugates showed stronger cytotoxic effects on Colon26 cancer cells compared to TIG-103 cells, due to the specificity of conventional nonmagnetic ionic liquids toward cancer cells (**Figure 4.15**).[29-31] In general, normal cells have healthy cell and nuclear membranes and rigid protein and mitochondrial structure rather than cancer cells those are endlessly and destructively proliferated. Therefore, ionic liquids might directly interact and destruct such fragile and deregulated cancer cell and cancer nuclear membranes themselves through several different mechanisms, such as altering cell membrane viscoelasticity and lipid distribution, mitochondrial dysfunction and permeabilization, disruption of cell and nuclear membranes, producing reactive oxygen species, changing the functions of transmembrane and cytoplasmatic proteins and enzymes, and fragmenting DNA.[30-32] For both nanoconjugates, the radioimmunoprecipitation assay (RIPA) lysis buffer was used as a positive control, consistently inducing strong cytotoxicity in both cell lines.

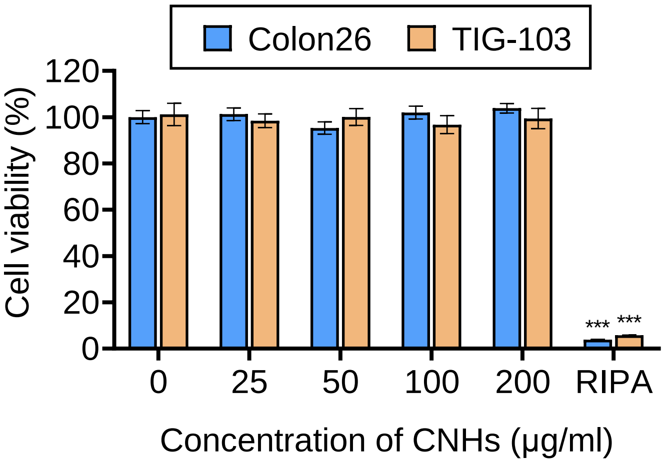

Figure 4.14 Viability of TIG-103 and Colon26 cells treated with the RIPA buffer (control) and PEG–CNH at various CNHs concentrations. Data presented as means ± standard error of the mean (SEM) (n = 5; biologically independent tests), ***, $p < 0.001$ versus control without nanoparticles (Student's *t-test*).

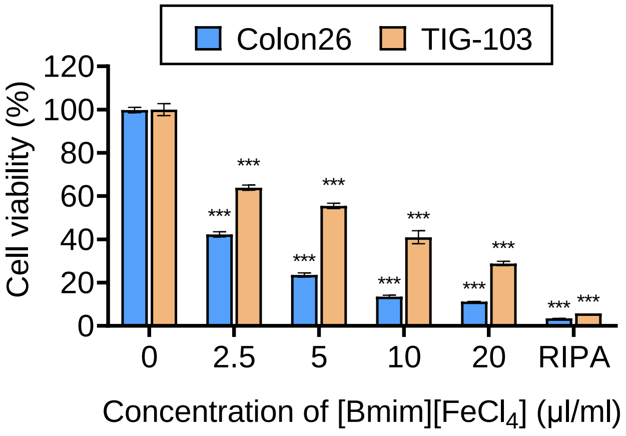

Figure 4.15 Viability of TIG-103 and Colon26 cells treated with the RIPA buffer (control) and [Bmim][$FeCl_4$]–PEG–CNH at various [Bmim][$FeCl_4$] concentrations. Data presented as means ± standard error of the mean (SEM) (n = 5; biologically independent tests), ***, $p < 0.001$ versus control without nanoparticles (Student's *t-test*).

The cytotoxicity of laser-induced [Bmim][$FeCl_4$]–PEG–CNH nanoconjugates was further investigated. TIG-103 and Colon26 cells co-incubated with either PEG–CNH or [Bmim][$FeCl_4$]–PEG–CNH were partially eliminated upon exposure to an 808 nm NIR laser at 0.7 W (~35.6 mW mm^{-2}) for 5 min, owing to the strong photothermal conversion properties of CNHs (**Figure 4.16**). Interestingly, by placing neodymium magnets at the bottom of well-plate, under the influence of magnetic field, [Bmim][$FeCl_4$]–PEG–CNH nanoconjugates were more effectively accumulated in the cells, leading to enhanced cells elimination (**Figure 4.17**). Notably, the laser-induced cytotoxicity of [Bmim][$FeCl_4$]–PEG–CNH was significantly lower in normal TIG-103 cells compared to Colon26 cancer cells. This can be attributed to the inherent heat sensitivity of cancer cells, which arises from selective biochemical responses such as the activation of heat-shock proteins and unique molecular signaling pathways under thermal stress.[33] These results further emphasize the selective anticancer efficacy of laser-induced [Bmim][$FeCl_4$]–PEG–CNH and the fact that the external magnetic field increased the accumulation of the nanoconjugates.

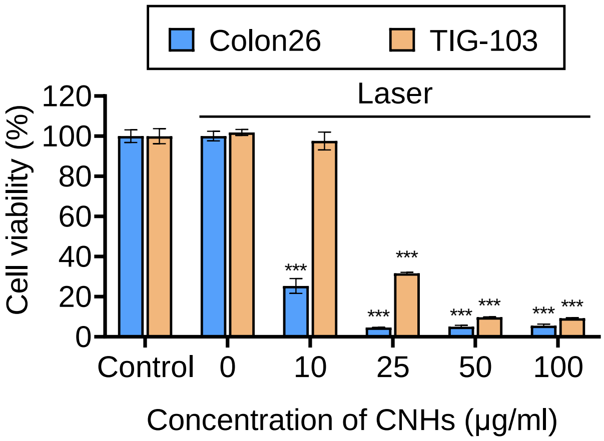

Figure 4.16 Laser-induced [Bmim][FeCl4]–PEG–CNH cytotoxicity evaluation in TIG-103 and Colon26 cells with 5 min laser irradiation at various CNHs concentrations. Data presented as means ± SEM (n = 5; biologically independent tests), ***, p < 0.001, by Student's *t-test*.

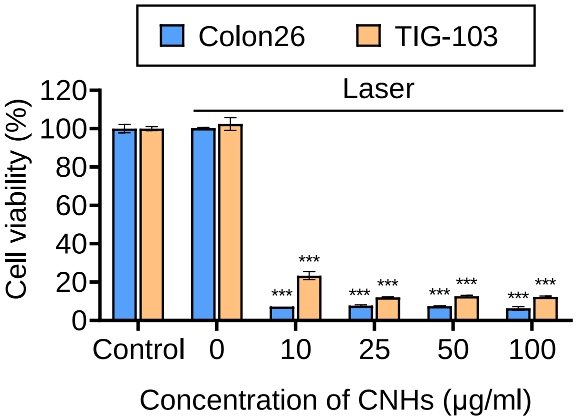

Figure 4.17 Laser-induced [Bmim][FeCl4]–PEG–CNH cytotoxicity evaluation in TIG-103 and Colon26 cells with 5 min laser irradiation under the magnet field at the bottom of the well plate at various CNHs concentrations. Data presented as means ± SEM (n = 5; biologically independent tests), ***, p < 0.001, by Student's *t-test*.

To further validate the laser-induced cytotoxicity of [Bmim][$FeCl_4$]–PEG–CNH nanoconjugates, we assessed their real-time anticancer activity using a single laser beam integrated into a fluorescence microscopy setup. Remarkably, after 808 nm laser irradiation at 254 mW (~129 mW mm^{-2}), the structure of Colon26 cancer cells incubated with [Bmim][$FeCl_4$]–PEG–CNH or PEG–CNH was immediately disrupted, forming bubbles, which are likely due to water vaporization caused by the strong photothermal conversion of CNHs (**Figure 4.18**). In contrast, control groups without nanoconjugates showed no cancer cell destruction, confirming that the photothermal effect was specific to the nanoconjugates. These results align with previous findings, further demonstrating that laser-activated [Bmim][$FeCl_4$]–PEG–CNH nanoconjugates can precisely target and eliminate cancer cells, underscoring their potential as highly effective agents in cancer photothermal therapy.

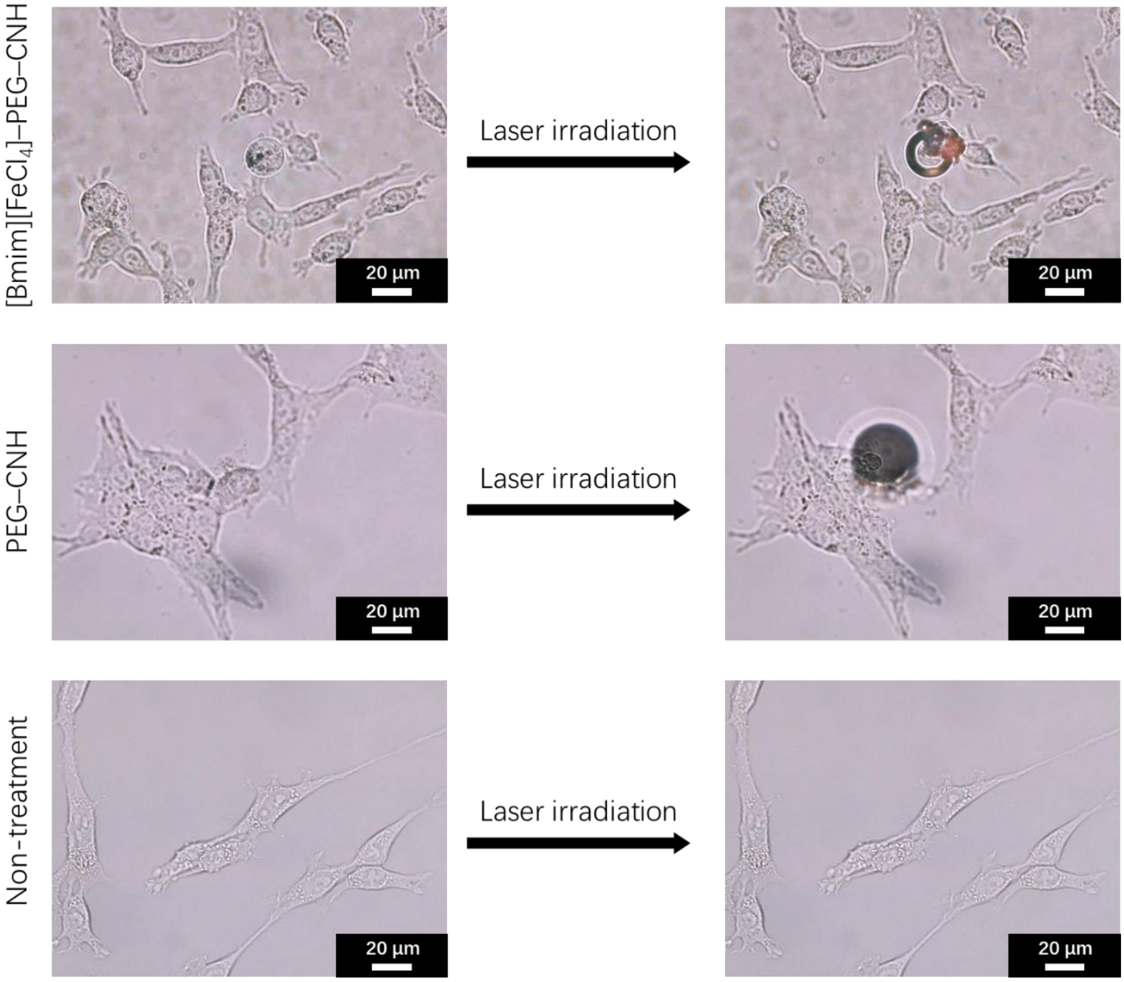

Figure 4.18 Colon26 cells destruction by laser-induced [Bmim][FeCl$_4$]–PEG–CNH before and after laser irradiation.

4.3.3 *In vivo* cancer theranostics

To assess the tumor-targeting capability of [Bmim][FeCl$_4$]–PEG–CNH nanoconjugates, indocyanine green (ICG) was encapsulated to synthesize [Bmim][FeCl$_4$]–PEG–ICG–CNH nanoconjugates, briefly, 1 mg ICG was mixed with 1 ml prepared [Bmim][FeCl$_4$]–PEG–CNH suspension and stirred up for 1 h with dark conditions (**Figure 4.19**). Hydrophobic ICG molecules can be entrapped with IMIQ in the hydrophobic region formed by long alkyl chains of DSPE–PEG$_{2000}$–NH$_2$ molecules. The fluorescence (FL) emission of [Bmim][FeCl$_4$]–PEG–ICG–CNH nanoconjugates were measured by FL spectra under the excitation of NIR region, which [Bmim][FeCl$_4$]–PEG–CNH didn't show any FL intensity (**Figure 4.20A**). Meanwhile, **Figure 4.20B** shows that the synthesized [Bmim][FeCl$_4$]–PEG–ICG–CNH had strong FL emission by various NIR light excitation.

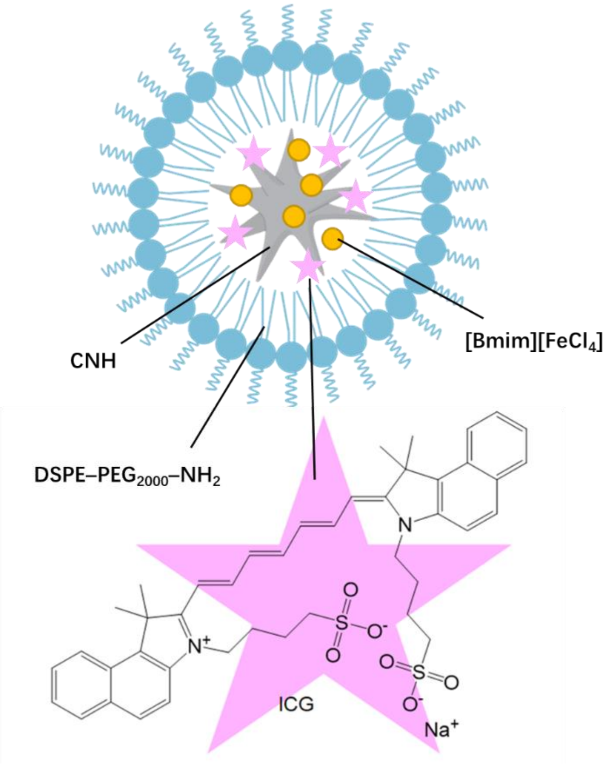

Figure 4.19 Schematic illustration of [Bmim][FeCl$_4$]–PEG–ICG–CNH nanoconjugates.

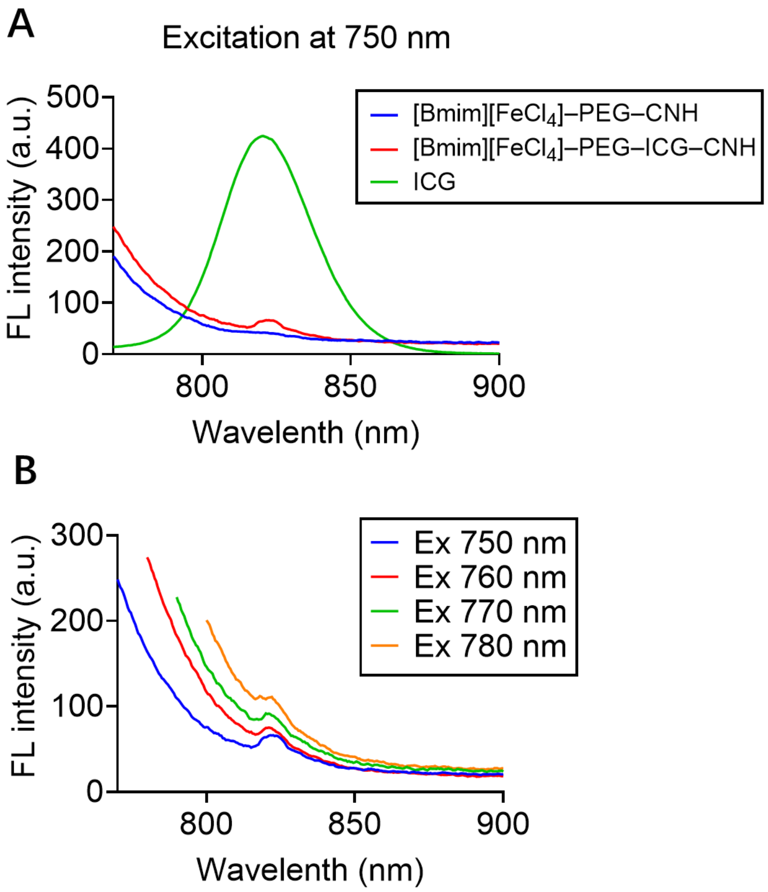

Figure 4.20 **A)** FL spectra of [Bmim][$FeCl_4$]–PEG–CNH, [Bmim][$FeCl_4$]–PEG–ICG–CNH, and ICG at 750 nm excitation wavelength. **B)** FL spectra of [Bmim][$FeCl_4$]–PEG–ICG–CNH at different excitation wavelength.

To investigate the systemic pharmacokinetics of [Bmim][$FeCl_4$]–PEG–ICG–CNH *in vivo*, fluorescence distribution was monitored in mice using a bioimager. The distributions of CNHs nanoconjugates were observed over time (4, 12, and 24 h) in tumors after intravenous (i.v.) injections through the tail vein of Colon26 tumor-bearing mice (**Figure 4.21**). Owing to the EPR effect, the gradual accumulation of

$[Bmim][FeCl_4]$–PEG–ICG–CNH nanoconjugates was observed in the tumor site over time.[20] Interestingly, in mice with neodymium magnets fixed at the tumor site, higher accumulation of nanoconjugates was observed, accompanied by stronger fluorescence intensity. In contrast, mice injected with PEG–ICG–CNH nanoconjugates and mice injected with $[Bmim][FeCl_4]$–PEG–ICG–CNH nanoconjugates but without neodymium magnets exhibited similar fluorescence distribution. The PBS control group showed no fluorescence throughout the body. In addition, the mice were dissected 24 hours after injection, and the NIR FL intensity of major organs including heart, liver, spleen, lung, kidney and tumor tissues were observed by using a bioimager (**Figure 4.22**). A minor amount of fluorescence was detected in the liver and kidneys after dissection, suggesting that the primary elimination pathway for the nanoconjugates is through renal excretion. The fluorescence observed in the lungs may be attributed to the pulmonary extraction by immune cells such as alveolar macrophages.[34, 35] Nanoparticle-mediated pulmonary drug delivery is recently gaining increasing attention as a means to overcome the biological barriers and accomplish site-specific drug delivery by controlling release of the loaded drug(s) at the target site.[36] In any case, these findings conclusively demonstrate that $[Bmim][FeCl_4]$–PEG–ICG–CNH nanoconjugates retain exceptional *in vivo* targeting abilities and can be effectively accumulated at the tumor site under magnetic control.

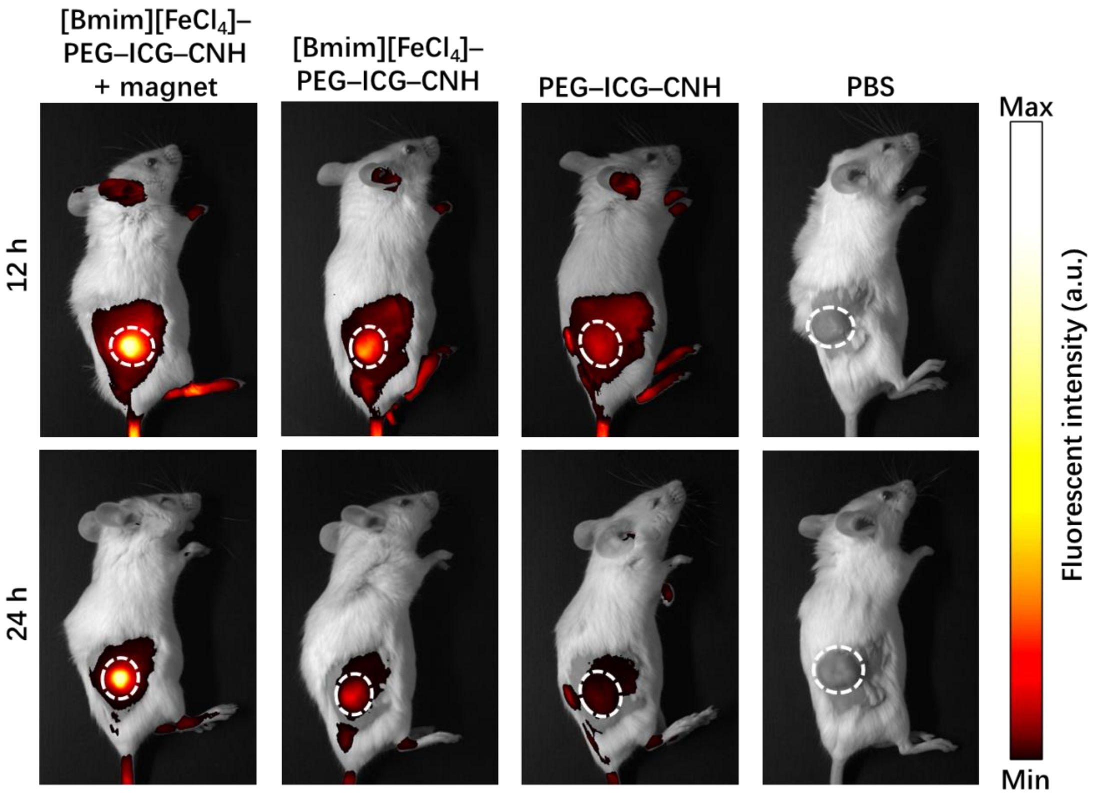

Figure 4.21 FL imaging of Colon26 tumor-bearing mice after an i.v. injection. White dashed circles denote the solid tumor location.

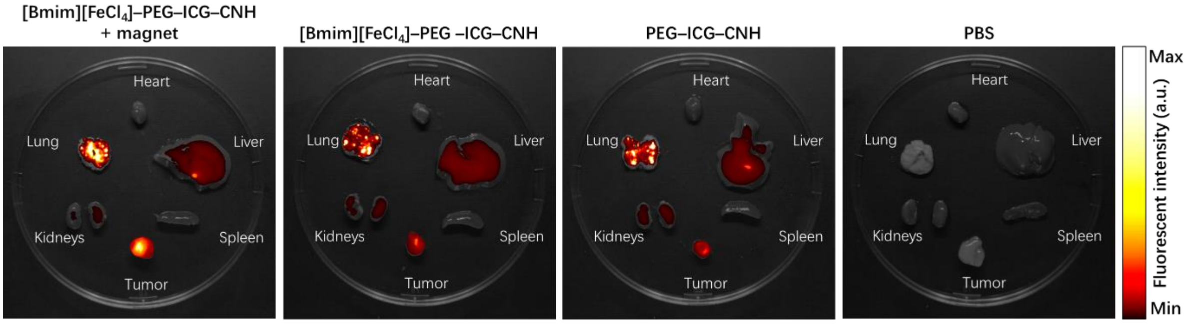

Figure 4.22 FL imaging of extracted vital organs and tumor tissue after an i.v. injection. White dashed circles denote the solid tumor location.

After confirming the targeting selectivity and controllability of [Bmim][$FeCl_4$]–PEG–CNH nanoconjugates *in vivo*, we further evaluated their laser-induced photothermal conversion efficiency using a homologous tumor model. Following intravenous injection of the nanoconjugates, neodymium magnets were affixed to the solid tumors of select mice. After 24 hours, the solid tumors were exposed to an 808 nm NIR laser at 0.7 W (~35.6 mW mm^{-2}) for 5 minutes. During the laser irradiation, the surface temperatures of the solid tumors were continuously monitored using a thermographic camera (**Figure 4.23**). The surface temperatures of the solid tumors in all mice were approximately 35 °C, before the laser irradiation. However, after 5 minutes of NIR laser irradiation, the surface temperature of tumors of mice injected with [Bmim][$FeCl_4$]–PEG–CNH after magnetic attraction increased significantly, reaching around 56 °C (**Figure 4.24**). In contrast, tumors of mice injected with PEG-CNH or [Bmim][$FeCl_4$]–PEG–CNH after magnetic induction displayed a lower temperature increase, reaching around 48 °C. Besides, even PBS-injected mice showed a slight temperature rise under NIR laser irradiation, likely due to light energy conversion to heat in the skin, blood, and tissue.

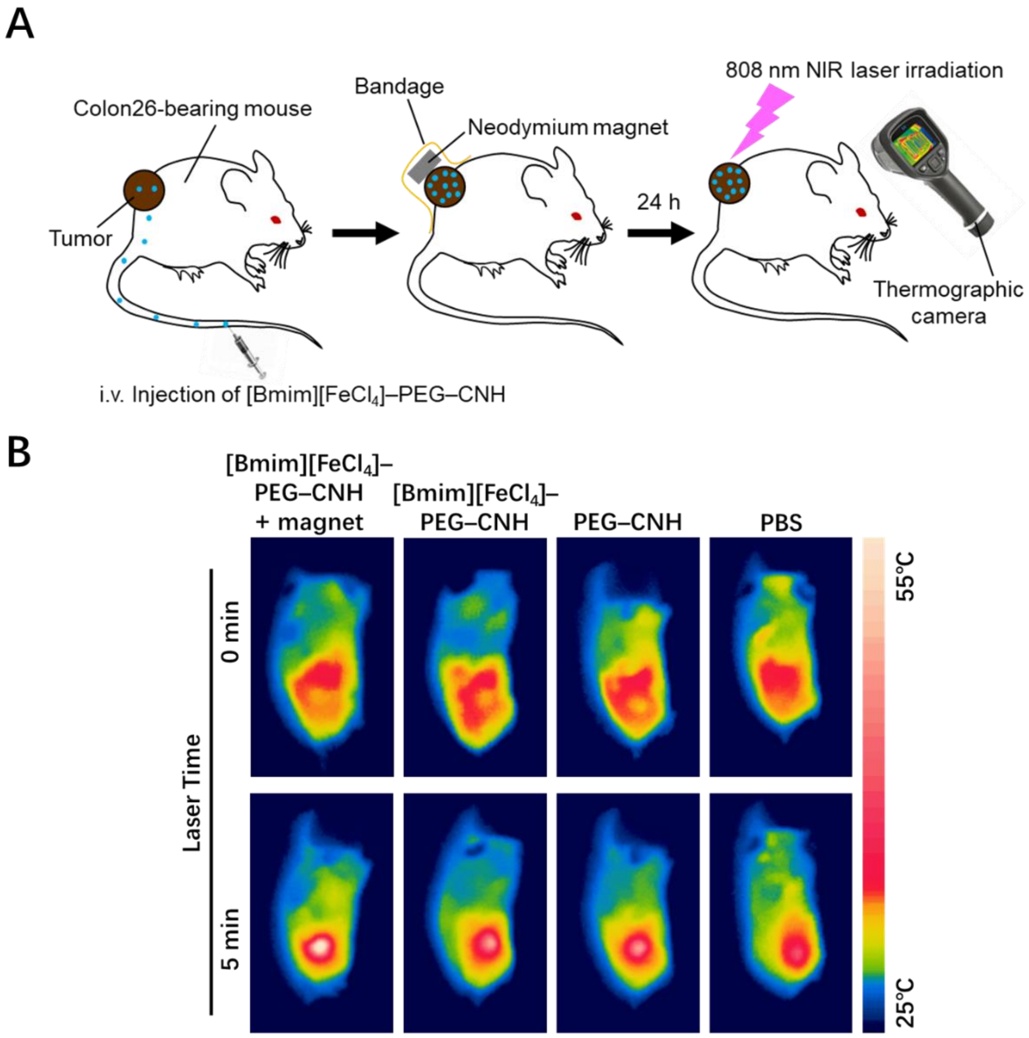

Figure 4.23 *In vivo* photothermal conversion activity of the laser- and magnetic field-induced Bmim $FeCl_4$–PEG–CNH. **A)** Experimental design of the *in vivo* anticancer experiment. PBS or a suspension of [Bmim][$FeCl_4$]–PEG–CNH, PEG–CNH, was intravenously injected into Colon26-bearing mice. A neodymium magnet was placed on the tumor using a bandage. After 24 h, the neodymium magnets were removed and the tumors were exposed to 808 nm laser irradiation [0.7 W (~35.6 mW mm^{-2}) for 5 min each day (total of four times)]. **B)** Thermographic measurement of the tumor on the mouse body surface for treatment with laser irradiation.

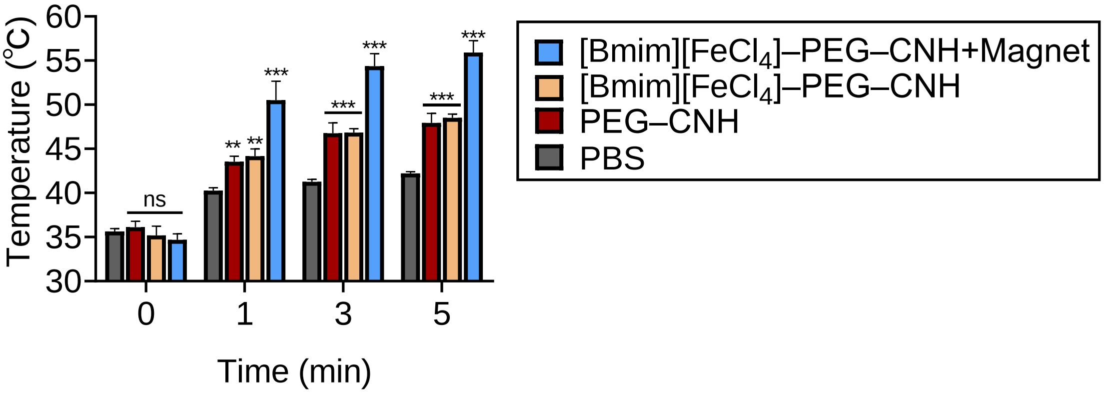

Figure 4.24 Solid tumor surface temperature of Colon26-bearing mice after injection followed by 808 nm laser irradiation for 5 min. Data are expressed as means ± standard error of the mean (SEM); n = 5 independent experiments. Statistical significance was calculated in comparison with the PBS group. **, $p < 0.01$, and ***, $p < 0.001$, by Student's *t-test*.

Meanwhile, the absence of *in vivo* toxicity of [Bmim][FeCl$_4$]–PEG–CNH nanoconjugates were further confirmed by blood tests (**Table 4-3**). After 7 days, there was no statistically significant difference in the CBC or biochemical parameters of mice intravenously injected with PBS or [Bmim][FeCl$_4$]–PEG–CNH suspension. Furthermore, [Bmim][FeCl$_4$]–PEG–CNH did not show any toxicity in tissues 7 days after i.v. injection (**Figure 4.25**). Indeed, hematoxylin and eosin (H&E) staining analyses demonstrated that the tissues of post i.v. injection of [Bmim][FeCl$_4$]–PEG–ICG–CNH resemble that of control group (PBS buffer).

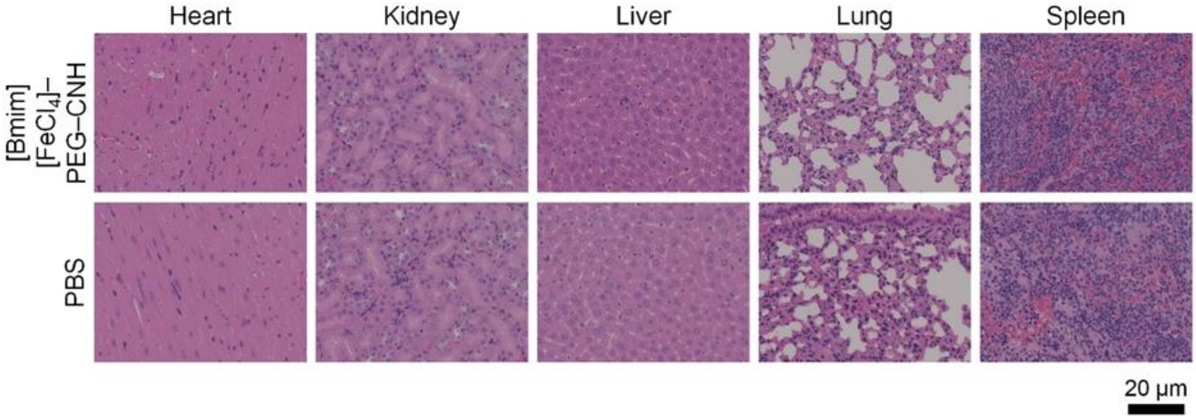

Figure 4.25 H&E staining in conventional organs sectioned after i.v. injection of [Bmim][$FeCl_4$]–PEG–CNH or PBS after 7 days.

Table 4-3 CBCs and biochemical parameters of the mice injected with PBS or [Bmim][FeCl$_4$]–PEG–ICG–CNH nanoparticle dispersion after 7 days.

Measured value	Entry	Unit	PBS (n = 6)	[Bmim][FeCl$_4$]–PEG–ICG–CNH (n = 6)	P value
CBC	WBC	$\times 10^{2}$ /μL	65.8 ± 3.85	61.8 ± 7.73	> 0.05
	RBC	$\times 10^{4}$ /μL	869.2 ± 28.25	874.7 ± 22.88	> 0.05
	HGB	g/dL	15.0 ± 0.43	15.3 ± 0.28	> 0.05
	HCT	%	15.5 ± 1.39	15.6 ± 0.75	> 0.05
	MCV	fL	52.3 ± 0.68	52.1 ± 0.62	> 0.05
	MCH	pg	17.3 ± 0.29	17.5 ± 0.30	> 0.05
	MCHC	g/dL	33.0 ± 0.30	33.5 ± 0.21	> 0.05
	PLT	$\times 10^{4}$ /μL	83.3 ± 3.43	86.4 ± 8.69	> 0.05
Biochemical parameters	TP	g/dL	4.6 ± 0.15	4.7 ± 0.15	> 0.05
	ALB	g/dL	3.0 ± 0.12	3.1 ± 0.08	> 0.05
	BUN	mg/dL	26.1 ± 2.43	23.5 ± 1.68	> 0.05
	CRE	mg/dL	0.1 ± 0.01	0.1 ± 0.01	> 0.05
	Na	mEq/L	144.3 ± 1.25	143.8 ± 0.69	> 0.05
	K	mEq/L	22.3 ± 1.32	23.0 ± 0.70	> 0.05
	Cl	mEq/L	104.5 ± 1.80	103.3 ± 1.80	> 0.05
	AST	IU/L	46.7 ± 5.47	44.7 ± 1.11	> 0.05
	ALT	IU/L	21.0 ± 3.46	20.5 ± 0.76	> 0.05
	LDH	IU/L	246.0 ± 59.66	239.2 ± 23.69	> 0.05
	AMY	IU/L	2378.3 ± 192.85	2662.7 ± 107.20	> 0.05
	CK	IU/L	65.5 ± 10.31	53.0 ± 4.51	> 0.05

Data are represented as means ± standard errors of the mean (SEM.); n = 6 biologically independent mice. Statistical analyses comprise the Student's two-sided *t test*.

Abbreviations: ALB, albumin; ALT, alanine transaminase; AMY, amylase; AST, aspartate aminotransferase; BUN, blood urea nitrogen; Cl, chlorine; CK, creatine kinase; CRE, creatinine; HCT, hematocrit; HGB, hemoglobin; K, potassium; LDH, lactate dehydrogenase; MCH, mean corpuscular hemoglobin; MCHC, mean corpuscular hemoglobin concentration; MCV, mean corpuscular volume; Na, sodium; PLT, platelet; RBC, red blood cell; TP, total protein; WBC, white blood cell.

Very interestingly, the synthesized CNHs nanoconjugates demonstrated significant anticancer effects with daily NIR laser irradiation. In mice injected with [Bmim][$FeCl_4$]–PEG–CNH after magnetic induction, complete tumor elimination was observed by the fourth irradiation, achieving a 100% cure rate (CR) and there was no recurrence in the following 20 days (**Figure 4.26**). Although slight burns appeared on the skin at the tumor site, these burn scars eventually fell off in later tests (**Figure 4.27**). In contrast, while the solid tumor volumes of mice injected with PEG–CNH or [Bmim][$FeCl_4$]–PEG–CNH without magnetic attraction were generally controlled under NIR laser irradiation, with a few tumors even being cured, tumor regrowth occurred once the laser treatment was stopped. This suggests the instability of relying solely on the EPR effect for tumor targeting. In the control group, which did not receive NIR laser irradiation, the anticancer properties of the ionic liquids still had some effect. The growth rate of solid tumors of mice injected with [Bmim][$FeCl_4$]–PEG–CNH slowed down, with even slower tumor growth observed in mice where magnets were fixed at the solid tumor site.

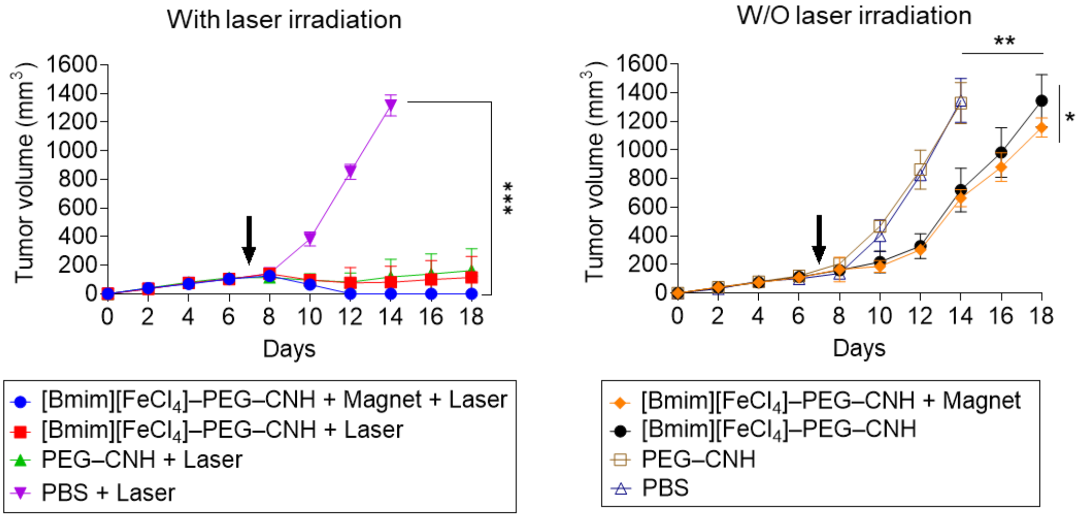

Figure 4.26 *In vivo* anticancer effect of various samples with and without laser irradiation. Irradiation time = 5 min every day (total four times irradiation). Data are expressed as means ± standard error of the mean (SEM) (n = 5 biologically independent tests). *, $p < 0.05$, **, $p < 0.01$, and ***, $p < 0.001$ by Student's *t-test*. The black arrows display the time point of sample administration.

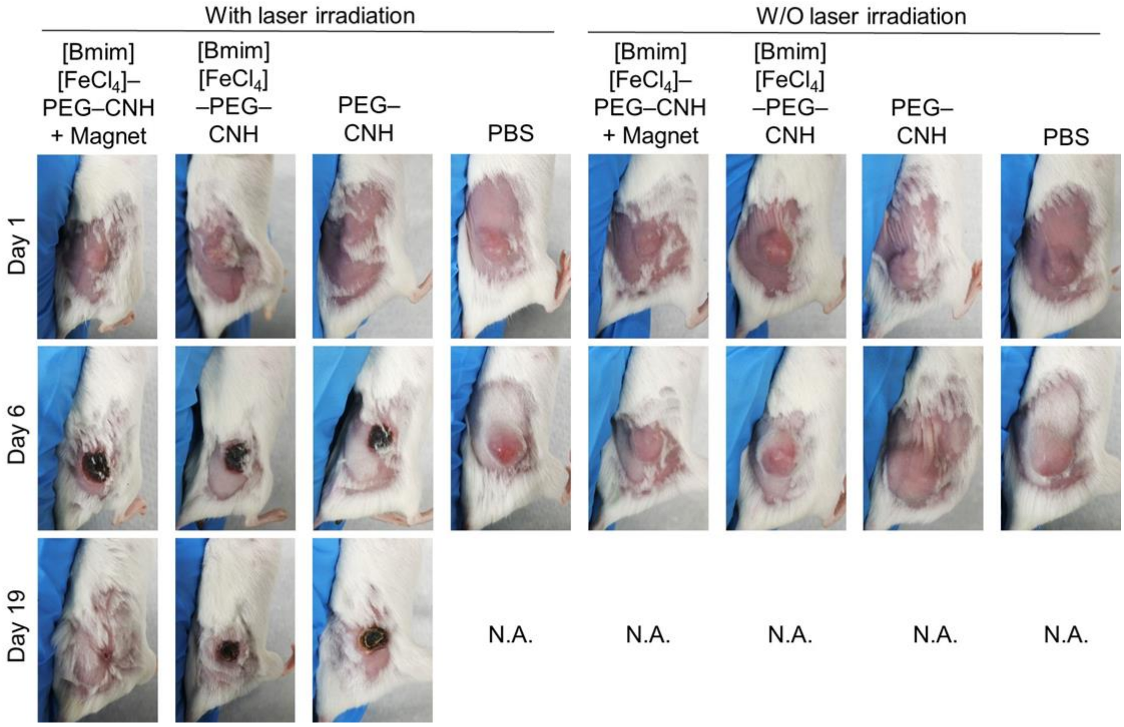

Figure 4.27 Images of mice after each treatment.

Besides, the body weight and survival rate of the mice were monitored every other day. Across all groups, the body weight of the mice increased steadily throughout the experiment, indicating no adverse side effects from the treatments (**Figure 4.28**). Notably, due to the anticancer effects of light-induced [Bmim][$FeCl_4$]–PEG–CNH, the survival rate of mice injected with the nanoconjugates was significantly extended, demonstrating the therapeutic safety of [Bmim][$FeCl_4$]–PEG–CNH in cancer treatment (**Figure 4.29**).

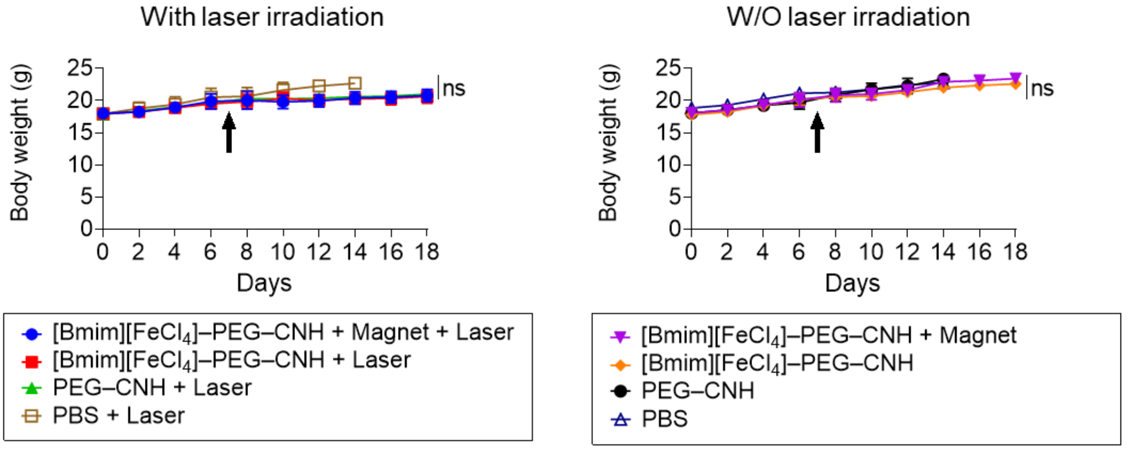

Figure 4.28 Average mouse body weight after treatments during the treatment period. The black arrow displays the time point of the sample administration. Data are expressed as means ± standard error of the mean (SEM) (n = 5 biologically independent tests). ns, not significant, by Student's *t-test*.

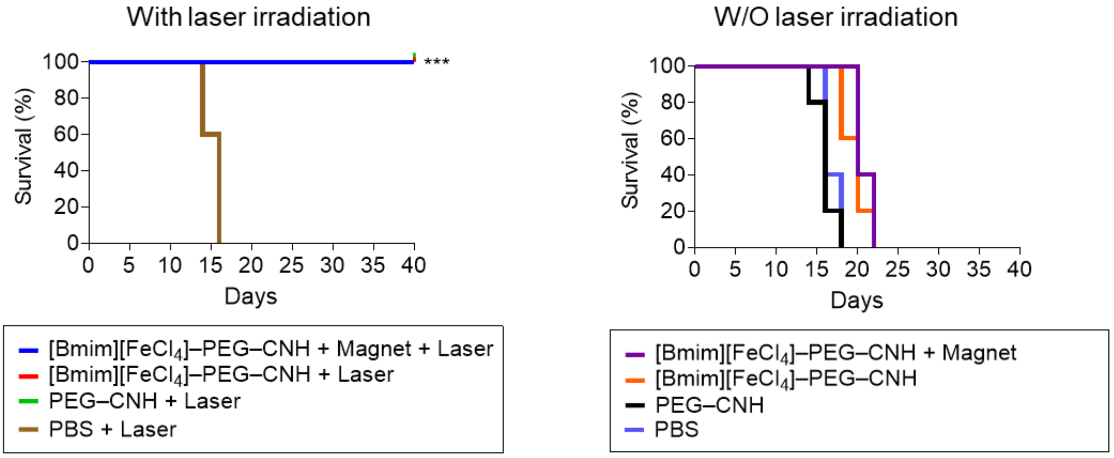

Figure 4.29 Kaplan–Meier survival curves of Colon26-tumor-bearing mice (n = 5 biologically independent mice) after tumor implantation for 30 days. Statistical significance was calculated in comparison with the NS group. ***, $p < 0.001$ by Log-rank (Mantel–Cox) test.

The solid tumor suppression behavior of NIR laser-induced [Bmim][$FeCl_4$]–PEG–CNH was further investigated using hematoxylin and eosin (H&E) staining, terminal deoxynucleotidyl transferase (TdT)-mediated 2′-deoxyuridine, 5′-triphosphate (dUTP) nick end labeling (TUNEL), and cleaved caspase-3 staining analysis (**Figure 4.30A**). Image-guided statistical IHC analysis using computer-aided software was also applied in this study because it is a highly useful and reliable technique for detection and quantification of target epitopes (e.g., proteins, structures, cellular components, etc.) in a wide variety tissue types (**Figure 4.30B**).[37, 38] H&E staining shows that, the solid tumor structure and cells were destroyed in [Bmim][$FeCl_4$]–PEG–CNH + Magnet + Laser, [Bmim][$FeCl_4$]–PEG–CNH + Laser and PEG–CNH + Laser groups under laser irradiation, among which [Bmim][$FeCl_4$]–PEG–CNH + Magnet + Laser was the most obvious, indicating a strong anti-tumor effect. Similarly, in TUNEL staining, [Bmim][$FeCl_4$]–PEG–CNH + Magnet + Laser also showed more apoptotic cells compared with other groups. Contrarily, H&E staining of tumor tissues showed no discernible lesions in the [Bmim][$FeCl_4$]–PEG–CNH + Magnet, [Bmim][$FeCl_4$]–PEG–CNH, PEG–CNH, and PBS groups since no laser irradiation. Cleaved Caspase3 staining further confirmed the potent *in vivo* anti-cancer mechanism of laser-induced [Bmim][$FeCl_4$]–PEG–CNH. Notably, cleaved caspase3 staining also shows brown dots in [Bmim][$FeCl_4$]–PEG–CNH + Magnet and [Bmim][$FeCl_4$]–PEG–CNH groups which are without laser irradiation, indicating the anti-cancer effect of [Bmim][$FeCl_4$]. The PBS group as control didn’t show any positive signal from all the staining.

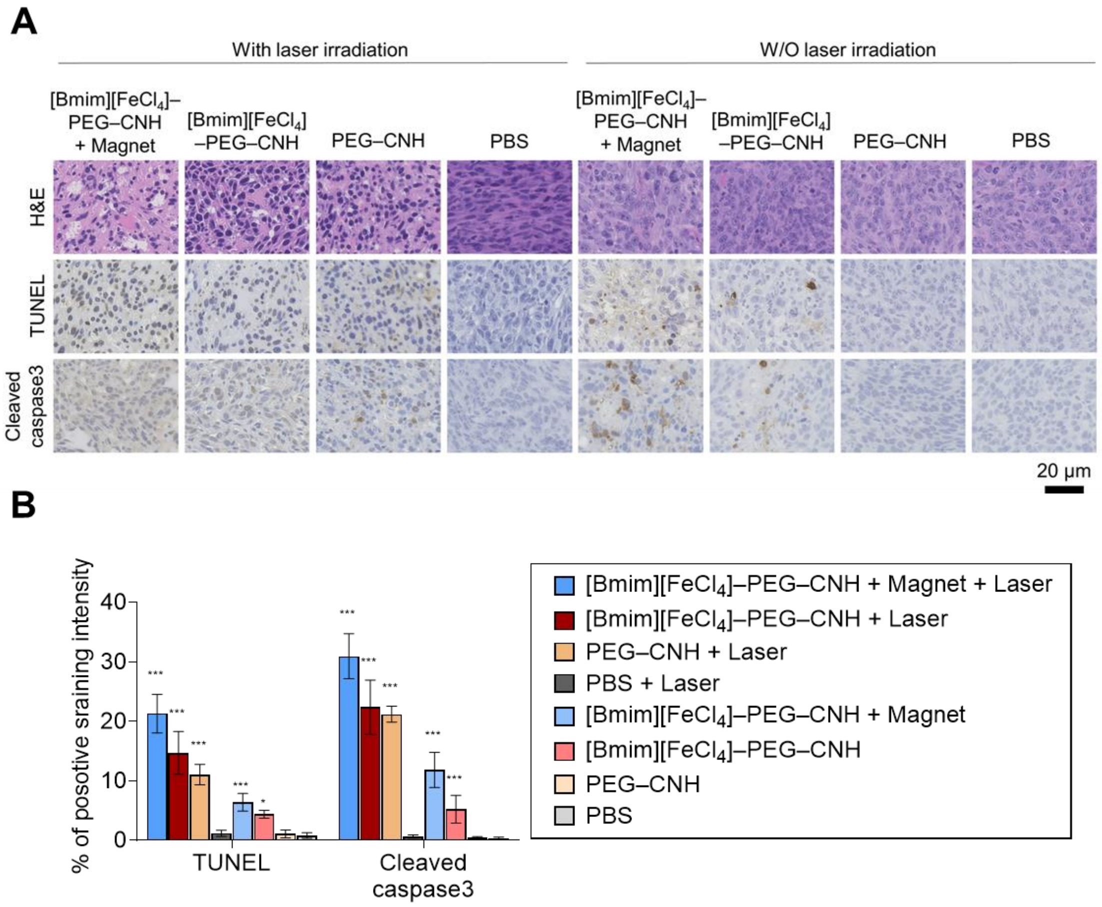

Figure 4.30 A) H&E, TUNEL, and Cleaved Caspase3 stained tumor tissues collected from different groups of mice at day 1 after their respective treatments. **B)** Statistical analyses of IHC and TUNEL-positive stained tumor tissues in Figure 4.26A. Data are represented as mean ± standard error of the mean (SEM); n = 7 independent areas (region of interest) in each tumor tissue collected from the groups of mice on day 1 after treatments. Statistical significance was calculated in comparison with the PBS group. *, $p < 0.05$, and ***, $p < 0.001$ by Student’s *t-test*.

4.4 Conclusion

In this chapter, we developed a chemotherapeutic, optical, and magnetically driven ionic liquid-modified CNH nanocomplex with excellent water dispersibility and photothermal stability. This represents the first application of a magnetic ionic liquid in cancer treatment. These nanocomplexes exhibited efficient tumor targeting under an external magnetic field and potent photothermal and NIR FL effects for cancer cell theranostic *in vitro* and *in vivo*. By improving the precision control of the EPR effect, our approach offers a promising strategy for precise and effective cancer theranostic, paving the way for advanced biomedical applications of multifunctional nanomaterials. *In vivo* anticancer efficacy of CNH nanocomplex was obviously amplified to suppress tumor growth via a simple and efficient nanoformulation strategy. At least, the efficacy of this proposed CNH nanocomplex system against a syngeneic mouse model is better than those of previous functional nanoparticles.[39-41] Moreover, we believe our nanosystem is better than chemotherapeutic, light, and magnetic field monotherapy because the combination therapy has apparently improved rates and durability of response to therapy. We also envision that the advantage of synergistic strategy of the developed nanosystem is effectively applicable to address tumor heterogeneity. Meanwhile, immune modulation induced by nanosystem would offer a novel approach for an innovative cancer immunotherapy.[42, 43] The proposed nanocomplex will be useful for designing an effective platform for sophisticated immunological regulation.

Conventional magnetic nanoparticles offer high magnetic moments and surface-area-to-volume ratios that make them attractive for cancer hyperthermia and active-targeted drug delivery system.[44] Additionally, they can function as contrast agents for magnetic resonance imaging and can improve the sensitivity of biosensors and diagnostic tools.[44] However, magnetic nanoparticles themselves do not have anticancer trait at all unless modification with anticancer drugs. In this study, we first found that magnetic ionic liquid itself has anticancer property in addition to various unique physicochemical traits for cancer treatments and manipulation of droplets. We believe that magnetic ionic liquid potentially offers versatile control due to their nature: 1) excellent fluidity, 2) adjustable surface tension, 3) chemical controllability and designability, 4) ionic and thermal conductivities, and 5) the ability to conjugate with other materials. These all-in-one properties empower magnetic ionic liquid to exhibit controllable molecular functions, and make magnetic ionic liquid susceptible to various fields, including electric, magnetic, electromagnetic, wave, light, and biomedical fields. Moreover, the manipulation of magnetic ionic liquid enable intriguing morphological changes and controllable motion (e.g., directional locomotion) of magnetic ionic liquid with new fluidic phenomena and practical applications such as soft electronics and robotics in addition to the current proposed nanomedicine. Exploring of potentiality of magnetic ionic liquid functions has just begun. We envision that the current study would help to stimulate imaginations for developing future innovative applications of magnetic ionic liquids.

4.5 References

1. Marullo, S.; Rizzo, C.; Dintcheva, N. T.; Giannici, F.; D'Anna, F., Ionic liquids gels: Soft materials for environmental remediation. *J Colloid Interface Sci* **2018,** *517*, 182-193.
2. Kore, R.; Srivastava, R., A simple, eco-friendly, and recyclable bi-functional acidic ionic liquid catalysts for Beckmann rearrangement. *Journal of Molecular Catalysis A: Chemical* **2013,** *376*, 90-97.
3. Florindo, C.; Araujo, J. M.; Alves, F.; Matos, C.; Ferraz, R.; Prudencio, C.; Noronha, J. P.; Petrovski, Z.; Branco, L.; Rebelo, L. P.; Marrucho, I. M., Evaluation of solubility and partition properties of ampicillin-based ionic liquids. *Int J Pharm* **2013,** *456* (2), 553-9.
4. Ferraz, R.; Branco, L. C.; Prudêncio, C.; Noronha, J. P.; Petrovski, Ž., Ionic Liquids as Active Pharmaceutical Ingredients. **2011,** *6* (6), 975-985.
5. Lewandowski, A.; Świderska-Mocek, A., Ionic liquids as electrolytes for Li-ion batteries—An overview of electrochemical studies. *Journal of Power Sources* **2009,** *194* (2), 601-609.
6. Shamshina, J. L.; Kelley, S. P.; Gurau, G.; Rogers, R. D., Chemistry: Develop ionic liquid drugs. *Nature* **2015,** *528* (7581), 188-189.
7. Babamale, H. F.; Khor, B.-K.; Chear, N. J.-Y.; Yam, W. S., Safe and selective anticancer agents from tetrafluorinated azobenzene-imidazolium ionic liquids: Synthesis, characterization, and cytotoxic effects. *Archiv der Pharmazie* **2022,** *355* (8), 2200085.
8. Kumer, A.; Sarker, M. N.; Paul, S., The simulating study of HOMO, LUMO, thermo physical and quantitative structure of activity relationship (QSAR) of some anticancer active ionic liquids. *Eurasian Journal of Environmental Research* **2019,** *3* (1), 1-10.
9. Moshikur, R. M.; Ali, M. K.; Wakabayashi, R.; Moniruzzaman, M.; Goto, M., Methotrexate-based ionic liquid as a potent anticancer drug for oral delivery: In vivo pharmacokinetics, biodistribution, and antitumor efficacy. *International Journal of Pharmaceutics* **2021,** *608*, 121129.
10. Shi, Y.; Zhao, Z.; Peng, K.; Gao, Y.; Wu, D.; Kim, J.; Mitragotri, S., Enhancement of Anticancer Efficacy and Tumor Penetration of Sorafenib by Ionic Liquids. *Advanced Healthcare Materials* **2021,** *10* (2), 2001455.
11. Zhao, F.; Yao, Y.; Li, X.; Lan, L.; Jiang, C.; Ping, J., Metallic Transition Metal Dichalcogenide Nanosheets as an Effective and Biocompatible Transducer for Electrochemical Detection of Pesticide. *Analytical Chemistry* **2018,** *90* (19), 11658-11664.
12. Comisso, N.; Berlouis, L. E. A.; Morrow, J.; Pagura, C., Changes in hydrogen storage properties of carbon nano-horns submitted to thermal oxidation. *International Journal of Hydrogen Energy* **2010,** *35* (17), 9070-9081.

13. Lodermeyer, F.; Costa, R. D.; Casillas, R.; Kohler, F. T. U.; Wasserscheid, P.; Prato, M.; Guldi, D. M., Carbon nanohorn-based electrolyte for dye-sensitized solar cells. *Energy & Environmental Science* **2015,** *8* (1), 241-246.
14. Sang, N.; Qi, Y.; Nishimura, S.; Miyako, E., Biomimetic Functional Nanocomplexes for Photothermal Cancer Chemoimmunotheranostics. *Small Science* **2024**.
15. Li, N.; Zhao, Q.; Shu, C.; Ma, X.; Li, R.; Shen, H.; Zhong, W., Targeted killing of cancer cells in vivo and in vitro with IGF-IR antibody-directed carbon nanohorns based drug delivery. *International Journal of Pharmaceutics* **2015,** *478* (2), 644-654.
16. Li, D.; Zhang, Y.; Xu, J.; Yoshino, F.; Xu, H.; Chen, X.; Zhao, L., Surface-engineered carbon nanohorns as a theranostic nanodevice for photoacoustic imaging and effective radiochemotherapy of cancer. *Carbon* **2021,** *180*, 185-196.
17. Zhang, J.; Ge, J.; Shultz, M. D.; Chung, E.; Singh, G.; Shu, C.; Fatouros, P. P.; Henderson, S. C.; Corwin, F. D.; Geohegan, D. B.; Puretzky, A. A.; Rouleau, C. M.; More, K.; Rylander, C.; Rylander, M. N.; Gibson, H. W.; Dorn, H. C., In vitro and in vivo studies of single-walled carbon nanohorns with encapsulated metallofullerenes and exohedrally functionalized quantum dots. *Nano Lett* **2010,** *10* (8), 2843-8.
18. Yu, Y.; Yang, X.; Reghu, S.; Kaul, S. C.; Wadhwa, R.; Miyako, E., Photothermogenetic inhibition of cancer stemness by near-infrared-light-activatable nanocomplexes. *Nature Communications* **2020,** *11* (1).
19. He, B.; Shi, Y.; Liang, Y.; Yang, A.; Fan, Z.; Yuan, L.; Zou, X.; Chang, X.; Zhang, H.; Wang, X.; Dai, W.; Wang, Y.; Zhang, Q., Single-walled carbon-nanohorns improve biocompatibility over nanotubes by triggering less protein-initiated pyroptosis and apoptosis in macrophages. *Nat Commun* **2018,** *9* (1), 2393.
20. Matsumura, Y.; Maeda, H. J. C. r., A new concept for macromolecular therapeutics in cancer chemotherapy: mechanism of tumoritropic accumulation of proteins and the antitumor agent smancs. **1986,** *46* (12_Part_1), 6387-6392.
21. Wang, R.; Xiao, R.; Zeng, Z.; Xu, L.; Wang, J., Application of poly(ethylene glycol)-distearoylphosphatidylethanolamine (PEG-DSPE) block copolymers and their derivatives as nanomaterials in drug delivery. *Int J Nanomedicine* **2012,** *7*, 4185-98.
22. Che, J.; Okeke, C. I.; Hu, Z. B.; Xu, J., DSPE-PEG: a distinctive component in drug delivery system. *Current pharmaceutical design* **2015,** *21* (12), 1598-605.
23. Friedman, H. L., The Visible and Ultraviolet Absorption Spectrum of the Tetrachloroferrate(III) Ion in Various Media1. *Journal of the American Chemical Society* **1952,** *74* (1), 5-10.
24. Hessel, C. M.; Pattani, V. P.; Rasch, M.; Panthani, M. G.; Koo, B.; Tunnell, J. W.; Korgel, B. A., Copper selenide nanocrystals for photothermal therapy. *Nano Lett* **2011,** *11* (6), 2560-6.

25. Li, Y.; Bai, G.; Zeng, S.; Hao, J., Theranostic Carbon Dots with Innovative NIR-II Emission for in Vivo Renal-Excreted Optical Imaging and Photothermal Therapy. *ACS Appl Mater Interfaces* **2019,** *11* (5), 4737-4744.
26. Li, J.; Pu, K., Semiconducting Polymer Nanomaterials as Near-Infrared Photoactivatable Protherapeutics for Cancer. *Acc Chem Res* **2020,** *53* (4), 752-762.
27. Magome, N.; Yoshikawa, K., Nonlinear Oscillation and Ameba-like Motion in an Oil/Water System. *The Journal of Physical Chemistry* **1996,** *100* (49), 19102-19105.
28. Okawa, D.; Pastine, S. J.; Zettl, A.; Fréchet, J. M. J., Surface Tension Mediated Conversion of Light to Work. *Journal of the American Chemical Society* **2009,** *131* (15), 5396-5398.
29. Babamale, H. F.; Khor, B. K.; Chear, N. J. Y.; Yam, W. S., Safe and selective anticancer agents from tetrafluorinated azobenzene-imidazolium ionic liquids: Synthesis, characterization, and cytotoxic effects. *Archiv der Pharmazie* **2022,** *355* (8).
30. Alfaifi, M. Y.; Elbehairi, S. E. I.; Elshaarawy, R. F. M.; Zein, M. A. E., Novel thiazolium ionic liquids-tagged bicyclo-palladium(II) Schiff base complexes; Synthesis, characterization and in vitro cytotoxicity toward ovarian cancer. *Journal of Molecular Structure* **2022,** *1249*, 131594.
31. Dias, A. R.; Costa-Rodrigues, J.; Fernandes, M. H.; Ferraz, R.; Prudêncio, C., The Anticancer Potential of Ionic Liquids. *ChemMedChem* **2017,** *12* (1), 11-18.
32. Ali, I.; Hozaifa, M.; Ali, S.; Malik, A.; Locatelli, M., Advances in ionic liquids as future anti-cancer drugs. *Journal of Molecular Liquids* **2023,** *388*.
33. Cavaliere, R.; Ciocatto, E. C.; Giovanella, B. C.; Heidelberger, C.; Johnson, R. O.; Margottini, M.; Mondovi, B.; Moricca, G.; Rossi-Fanelli, A., Selective heat sensitivity of cancer cells. Biochemical and clinical studies. *Cancer* **1967,** *20* (9), 1351-81.
34. Lee, D.-K.; Kim, G.; Maruthupandy, M.; Lee, K.; Cho, W.-S., Multimodal pulmonary clearance kinetics of carbon black nanoparticles deposited in the lungs of rats: the role of alveolar macrophages. *Particle and Fibre Toxicology* **2024,** *21* (1), 32.
35. Ge, D.; Ma, S.; Sun, T.; Li, Y.; Wei, J.; Wang, C.; Chen, X.; Liao, Y., Pulmonary delivery of dual-targeted nanoparticles improves tumor accumulation and cancer cell targeting by restricting macrophage interception in orthotopic lung tumors. *Biomaterials* **2025,** *315*, 122955.
36. Huang, Z.; Kłodzińska, S. N.; Wan, F.; Nielsen, H. M., Nanoparticle-mediated pulmonary drug delivery: state of the art towards efficient treatment of recalcitrant respiratory tract bacterial infections. *Drug delivery and translational research* **2021,** *11* (4), 1634-1654.
37. Shimada, E.; Matsumoto, Y.; Nakagawa, M.; Susuki, Y.; Endo, M.; Setsu, N.; Fujiwara, T.; Iida, K.; Nabeshima, A.; Yahiro, K.; Kimura, A.; Hirose, T.; Kanahori, M.; Oyama, R.; Oda, Y.; Nakashima, Y., Methylation-mediated silencing of protein kinase C zeta induces apoptosis avoidance through ATM/CHK2

inactivation in dedifferentiated chondrosarcoma. *British journal of cancer* **2022,** *126* (9), 1289-1300.

38. Tollemar, V.; Tudzarovski, N.; Boberg, E.; Törnqvist Andrén, A.; Al-Adili, A.; Le Blanc, K.; Garming Legert, K.; Bottai, M.; Warfvinge, G.; Sugars, R. V., Quantitative chromogenic immunohistochemical image analysis in cellprofiler software. *Cytometry. Part A : the journal of the International Society for Analytical Cytology* **2018,** *93* (10), 1051-1059.
39. Zhou, Z.; Liu, Y.; Jiang, X.; Zheng, C.; Luo, W.; Xiang, X.; Qi, X.; Shen, J., Metformin modified chitosan as a multi-functional adjuvant to enhance cisplatin-based tumor chemotherapy efficacy. *International Journal of Biological Macromolecules* **2023,** *224*, 797-809.
40. Zhou, Z.; Wang, H.; Li, J.; Jiang, X.; Li, Z.; Shen, J., Recent progress, perspectives, and issues of engineered PD-L1 regulation nano-system to better cure tumor: A review. *International Journal of Biological Macromolecules* **2024,** *254*, 127911.
41. Zheng, C.; Luo, W.; Liu, Y.; Chen, J.; Deng, H.; Zhou, Z.; Shen, J., Killing three birds with one stone: Multi-stage metabolic regulation mediated by clinically usable berberine liposome to overcome photodynamic immunotherapy resistance. *Chemical Engineering Journal* **2023,** *454*, 140164.
42. Riley, R. S.; June, C. H.; Langer, R.; Mitchell, M. J., Delivery technologies for cancer immunotherapy. *Nature reviews. Drug discovery* **2019,** *18* (3), 175-196.
43. Moy, A. J.; Tunnell, J. W., Combinatorial immunotherapy and nanoparticle mediated hyperthermia. *Adv Drug Deliv Rev* **2017,** *114*, 175-183.
44. Roper, D. K.; Ahn, W.; Hoepfner, M., Microscale Heat Transfer Transduced by Surface Plasmon Resonant Gold Nanoparticles. *The Journal of Physical Chemistry C* **2007,** *111* (9), 3636-3641.

Chapter 5

General Conclusion

Cancer remains one of the leading causes of death globally due to its invasive and metastatic nature. Conventional treatments like surgery, chemotherapy, and radiotherapy face limitations, including poor specificity, significant side effects, and limited efficacy in metastatic stages. Photothermal therapy (PTT) has emerged as a promising alternative for cancer treatment due to its advantages of high specificity, minimal invasiveness, and reduced toxicity. PTT leverages photosensitizers that convert near-infrared (NIR) light into heat, enabling the thermal ablation of cancer cells. Nanoparticles, due to their enhanced permeability and retention effect, have shown promise as photosensitizers, but challenges in stability, targeting, and functionalization have limited their broader application.

This research focused on the development of multifunctional soft nanomaterials and proposed a series of advanced intravenously injectable soft nanoconjugates for cancer photothermal therapy. In **Chapter 2**, we discussed the synthesis of functional liquid metal (LM) nanoparticles. Gallium-based eutectic alloys were used with surface modifications using biomolecules to improve stability, dispersibility, and biocompatibility. The nanoparticles demonstrated exceptional stability in aqueous solutions for extended periods and high photothermal conversion efficiency (up to 49%), outperforming many existing materials. The laser-induced LM nanoconjugates showed potent tumor ablation capabilities in both *in vitro* and *in vivo* models, selectively targeting cancer cells with minimal harm to normal tissues. In **Chapter 3**, we further modified the LM nanoconjugates with anticancer drugs and immuno-checkpoint inhibitors, the incorporation of immunostimulants into LM nanoparticles enabled the combination of PTT with immune system activation, opening the way for synergistic cancer treatments. It is the first to exploit the various physicochemical properties of LM nanoparticles for cancer immunotheranostics. Under synergistic treatment, tumors are eliminated more efficiently and accurately. In **Chapter 4**, an optically and magnetically driven drug delivery system using functional soft material ionic liquids and promising photo exothermic material carbon nanohorns (CNHs) was proposed, which will expand the concept of traditional nanoparticle accumulation mechanisms (EPR effect) by active targeting effect. In fact, the synthesized CNHs nanoconjugates have more efficient photothermal conversion efficiency (up to 63%) and can accumulate more effectively at the tumor site due to the loading of magnetic particles, achieving precise tumor elimination. Future studies should explore scaling production, detailed pharmacokinetics, and long-term safety assessments in human trials. Additionally, integrating more advanced targeting mechanisms and combining these nanoconjugates with other therapeutic modalities could further enhance their efficacy.

In conclusion, our research on multifunctional soft nanomaterials has achieved encouraging results. From biomolecule-modified nanoconjugates that highly rely on the EPR effect, to antibody-bound immunogenic nanoconjugates with drug delivery capabilities, and finally to smart nanoconjugates that can be controlled by external magnetic fields. We believe that these multifunctional nanoconjugates will provide new solutions for photothermal cancer therapy.

List of publications

Publications related to this dissertation

- **Y. Qi**, A. Kimura, M Taguchi, E. Miyako, Sonication- and γ-ray-mediated biomolecule-liquid metal nanoparticlization in cancer optotheranostics. *Appl. Mater. Today* 26, 101302 (**2022**). (Chapter 2)
- **Y. Qi**, M. Miyahara, S. Iwata, E. Miyako, Light-activatable liquid metal immunostimulants for cancer nanotheranostics. *Adv. Funct. Mater.* 34, 2305886 (**2024**). (Chapter 3)
- **Y. Qi**, E. Miyako, Multifunctional magnetic ionic liquid-carbon nanohorn complexes for targeted cancer theranostics. *Small Sci.* xxxxxxx **(2025)**. (Chapter 4) (In Press)

Other publications

- K. Sakamoto, **Y. Qi**, E. Miyako, Nanoformulation of the K-Ras(G12D)-inhibitory peptide KS-58 suppresses colorectal and pancreatic cancer-derived tumors. *Sci. Rep.* 13, 518 (**2023**).
- T. Wang, **Y. Qi**, E. Miyako, A. Bianco, C. Ménard-Moyon, Photocrosslinked co-assembled amino acid nanoparticles for controlled chemo/photothermal combined anticancer therapy. *Small* 20, 2307337 (**2024**).
- N. Sang, **Y. Qi**, S. Nishimura, E. Miyako, Biomimetic functional nanocomplexes for photothermal cancer chemoimmunotheranostics. *Small Sci.* 2400324 (**2024**).

Presentation

- Light-activatable liquid metal immunostimulants for cancer nanotheranostics, Kazunari Akiyoshi Award, International Symposium on Exponential Biomedical DX 2024(eMEDX-24) | Ishikawa, Japan, December 19th – 20th 2024

Awards and grants

- The State Scholarship Fund by China Scholarship Council (CSC). (October 2023 to March 2025)

Acknowledgements

As I complete my doctoral dissertation, my time at JAIST will come to an end. I would like to express my sincere gratitude to everyone who has helped me over the past five years.

First and foremost, I would like to thank my supervisor, Prof. Eijiro Miyako, or Miyako sensei as I prefer to call him. I have benefited greatly from his dedication and passion for science. From my master's project to my doctoral project, he has always been a valuable guide to my studies and research. He has always provided me with support and encouragement when I face difficulties.

I am also very grateful to Prof. Kazuaki Matsumura as my second supervisor, Prof. Yuki Nagao and Prof. Yoshifumi Oshima as my minor research supervisor, for their invaluable comments and constructive suggestions on my research. I am also deeply thankful to Prof. Kazuaki Matsumura, Prof. Motoichi Kurisawa, Prof. Shun Nishimura and Dr. Mitsumasa Taguchi for taking their precious time to serve as referees for my doctoral defense and providing me with indispensable help and support in improving this study.

I would like to thank all the members of the Miyako Lab for providing multiple perspectives and positive feedback on my research during my study life. And I also appreciate Dr. Tongmin Chen and Dr. Yuanzhe Xu from Oshima Lab for their long-term support for the TEM results of this study. I also thank Prof. Shun Nishimura for his assistance with the TGA measurement in **Chapter 4**.

I would like to thank my family, girlfriend, and other friends. Their encouragement and support are the most precious wealth I have gained. Without their trust and understanding, I would not be able to achieve my current achievements and success. Special thanks to my late father, who is my lifelong role model.

Last but not least, I would also like to thank the China Scholarship Council for providing scholarship support during my doctoral studies. Thanks to JAIST for providing me with a good research and learning environment. Finally, I would like to express my appreciation again to everyone who has given me help and support.